University of Southampton

Faculty of Engineering and Physical Sciences

Optoelectronics Research Centre

Bismuth-Doped Optical Fibre Fabrication and Laser Development

by

Siyi Wang

Supervisors: Prof. Jayanta Sahu and Prof. David Richardson

Thesis for the degree of Doctor of Philosophy

August 2023

https://orcid.org/0000-0002-1374-1196

University of Southampton

Abstract

Faculty of Engineering and Physical Sciences

Optoelectronics Research Centre

Doctor of Philosophy

By Siyi Wang

The incorporation of bismuth (Bi) as a dopant in silica fibre has demonstrated great potential for the development of fibre lasers and amplifiers. Silica fibres doped with Bi, in combination with aluminium (Al), phosphorus (P), and germanium (Ge), can provide amplification covering different spectral bands in the wavelength range of 1.1-1.5 µm and 1.62-1.75 µm, which are typically inaccessible to rare-earth (RE) doped silica fibres.

This thesis presents a detailed study of Bi-doped fibres (BDFs) in phosphosilicate and aluminosilicate host, fabricated using the modified chemical vapour deposition (MCVD)-solution doping technique. The study investigates the impact of various fabrication conditions on the performance of Bi-doped phosphosilicate fibres (BPSFs) and Bi-doped aluminosilicate fibres (BASFs). The conditions include soot deposition temperature, solution composition, collapsing of preforms in O2/He atmospheres, and fibre drawing speed. The optical properties of the BDFs were characterised through measurements of absorption and unsaturable loss. The results of this characterisation and the subsequent laser experiments were used as feedback for the optimisation of the fabrication process. Spectroscopic studies of BASFs were also conducted, including measurements of fluorescence spectrum, lifetime, absorption and emission cross-section, and unique anti-stoke emission in the visible wavelength region.

Additionally, Bi-doped fibre lasers (BDFLs) were developed to assess the performance of the fibres. A BDFL based on a 200m BPSF was demonstrated to operate at 1340nm with 172mW output power and 38% slope efficiency. Afterwards, the laser was continuously tuned in the spectra range of 1305-1375nm by employing different tuning elements, such as an optical filter and a tunable fibre Bragg grating. However, the development of BDFLs in the 1.1µm band based on BASFs faces challenges due to high unsaturable loss in the fibre, resulting in poor laser output performance. Thus, further optimisation of the fabrication process is crucial to increase the efficiency of BASFs.

Overall, this work provides important insights into the fabrication and optimisation of Bi-doped silica fibres for use in fibre lasers and amplifiers.

Contents

Table of Figures

Table of Tables

Declaration of Authorship

Print name: Siyi Wang

Title of thesis: Bismuth-Doped Optical Fibre Fabrication and Laser Development

I declare that this thesis and the work presented in it are my own and has been generated by me as the result of my own original research.

I confirm that:

1. This work was done wholly or mainly while in candidature for a research degree at this University;
2. Where any part of this thesis has previously been submitted for a degree or any other qualification at this University or any other institution, this has been clearly stated;
3. Where I have consulted the published work of others, this is always clearly attributed;
4. Where I have quoted from the work of others, the source is always given. With the exception of such quotations, this thesis is entirely my own work;
5. I have acknowledged all main sources of help;
6. Where the thesis is based on work done by myself jointly with others, I have made clear exactly what was done by others and what I have contributed myself;
7. Parts of this work have been published as: Appendix A

Signature: ..... Date: .....

Acknowledgements

First and foremost, I want to express deep gratitude to my supervisor, Pro. Jayanta Sahu, for his unwavering support throughout my Ph.D. journey. He ignited my initial spark of interest during my graduate studies and provided the opportunity to tread this path. He has been the beginning of everything. I also deeply appreciate Pro. David Richardson's time and feedback, as well as the II-VI Foundation, USA, for their generous sponsorship.

I sincerely extend my thanks to Dr. Pranabesh Barua, Dr. Andrey A. Umnikov, and Dr. Martin Nunez Velazquez for their thorough training, providing me with essential skills and knowledge to conquer numerous research challenges. The time we shared in the cleanroom holds a special place in my heart. My appreciation also extends to Wang Yu, Ziwei Zhai, Angeles Camacho Rosales, and Norberto Ramirez Martinez for their ongoing support.

I'm grateful for the support of Dr. James Gates and Pro. Periklis Petropoulos during my research's midway point. I extend my thanks to Pro. Senthil Murugan Ganapathy and Pro. Bernard Dussardier for examining my thesis during the final viva, validating my dedication, and providing essential suggestions. Dr. Morten Ibsen's aid in fabricating fibre Bragg gratings holds significant value. A special acknowledgment goes to Pro. Radan Slavik for his trust and support, which helped me regain my confidence during moments of self-doubt.

I deeply appreciate to my family for their love and support, despite the physical distance. I am also grateful to my feline companions, whose comforting presence has been a solace during nights of despair and exhaustion.

At most, my heartfelt thanks go to my friends. Their presence is like the sparkling stars shining through the cloud-covered night sky. During countless moments of vulnerability and sensitivity, their contagious smiles, and comforting hugs have always been a source of strength and made me a better person. Mr. Liu, your distinct significance cannot be denied by anyone. This unforgettable period of time will forever be etched in my heart.

And, finally, I thank myself for persevering through the challenges of the past few years. Though science can be an impersonal and arduous endeavour, it is the people who make it worthwhile and gentle.

To the past

Abbreviations

AOM ..... **A**cousto-**O**ptic **M**odulator

ASE..... **A**mplified **S**pontaneous **E**mission

ATT..... **Att**enuator

BAC ..... **B**i **A**ctive **C**entre

BASF..... **B**i-doped **A**luminosilicate **F**ibre

BDF ..... **B**i-**D**oped **F**ibre

BDFA ..... **B**i-**D**oped **F**ibre **A**mplifier

BDFL..... **B**i-**D**oped **F**ibre **L**aser

BGSF ..... **B**i-doped **G**ermano**S**ilicate **F**ibre

Bi..... **B**ismuth

BPGSF ..... **B**i-doped **P**hospho**G**ermano**S**ilicate **F**ibre

BPSF..... **B**i-doped **P**hospho**S**ilicate **F**ibre

CNT ..... **C**arbon **N**ano**t**ubes

CW ..... **C**ontinuous-**W**ave

EDFA ..... **E**rbium-**D**oped **F**ibre **A**mplifier

EPMA..... **E**lectron **P**robe **M**icro **A**nalysis

ESA..... **E**xcited **S**tate **A**bsorption

ETU ..... **E**nergy **T**ransfer **U**pconversion

FUT ..... **F**ibre **U**nder **T**est

FWHM ..... **F**ull **W**idth at **H**alf **M**aximum

ISO ..... **Iso**lator

LD..... **L**aser **D**iode

MCVD ..... **M**odified **C**hemical **V**apour **D**eposition

MOPA ..... **M**aster **O**scillator **P**ower **A**mplifier

NALM..... **N**on-linear **A**mplifying **L**oop **M**irror

NIR..... **N**ear-**I**nfrared

NOLM ..... **N**on-linear **O**ptical **L**oop **M**irror

NPR..... **N**onlinear **P**olarisation **R**otation

OC..... **O**utput **C**oupler/**C**oupling ratio

OSA..... **O**ptical **S**pectrum **A**nalyser

OSNR ..... **O**ptical **S**ignal-to-**N**oise **R**atio

OVD ..... **O**utside **V**apour **D**eposition

PC ..... **P**olarisation **C**ontroller

PBC ..... **P**olarisation **B**eam **C**ombiner

PCVD ..... **P**lasma-activated **C**hemical **V**apour **D**eposition

RE ..... **R**are-**E**arth

SESAM ..... **Se**miconductor **S**aturable **A**bsorber **M**irror

SIMS ..... **S**econdary **I**on **M**ass **S**pectrometry

SWCNT ..... **S**ingle-**W**alled **C**arbon **N**ano**t**ubes

UL ..... **U**nsaturable **L**oss

VAD ..... **V**apour **A**xial **D**eposition

WDM ..... **W**avelength-**D**ivision-**M**ultiplexing

WLS ..... **W**hite **L**ight **S**ource

Chapter 1 Introduction

1.1 Motivation and Challenge

Silica fibre has been developed rapidly over the past decades and has been applied widely in various fields, such as fibre amplifiers, fibre lasers, fibre sensors and gyroscopes. It has revolutionised optical communications with low propagation loss in a large bandwidth, allowing data transmission over long distances [1, 2]. The invention of the fibre amplifier, particularly the erbium-doped fibre amplifier (EDFA) [3], was a breakthrough in optical communications and boosted the field dramatically. At the same time, the fibre laser keeps playing an essential role in the industry, from laser weapons and material processing [4, 5], to spectroscopy and medicine [6], benefiting from its high gain, efficient cooling, high-quality optical beam, and compactness.

In recent years, exploring fibre lasers and amplifiers capable of operating in the new wavelength bands has drawn significant interest. Optical fibres doped with rare-earth (RE) ions are widely used in the near-infrared (NIR) wavelength region, covering bands around 1 μm, 1.5 μm, 1.8 μm, and 2 μm, respectively, with different RE ions such as neodymium (Nd), ytterbium (Yb), erbium (Er), thulium (Tm) and holmium (Ho), as shown in Figure 1.1. However, there exists a significant gap in the working laser wavelengths of RE-doped fibres in the spectral region of 1.1-1.5 μm and 1.62-1.75 μm. In particular, the wavelength gap around 1.3 μm is crucial for the availability of lasers and amplifiers, as it can fill the low-loss transmission window of SMF-28 [7], increasing the capacity of today's fibre optic communication. Furthermore, with the help of low-loss hollow-core fibre that provides ~ 0.5 dB/km loss at 1064 nm and 1100 nm [8], the telecommunication bandwidth can even be extended to 1 μm, indicating the need for new amplifiers and lasers. In addition, a suitable fibre laser operating at 1100-1200 nm would enable an efficient visible light source in the wavelength range of 575-590 nm by frequency doubling, which can be beneficial for astronomy [9], ophthalmology [10] and dermatology [11].

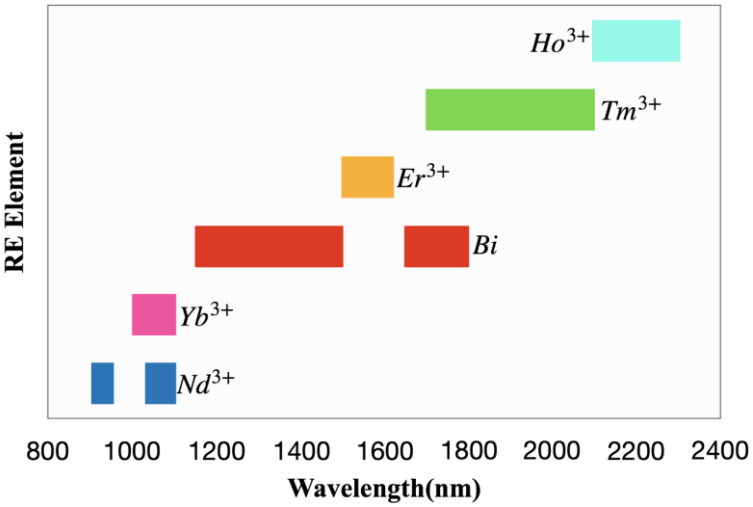

Figure 1.1 Wavelength bands covered by silica fibres doped with different REs and Bi ions.

Different dopants have been extensively studied in silica fibres to broaden the wavelength range of operation. Among them, bismuth (Bi) has emerged as a leading candidate as it can extend the emission wavelength beyond what is normally covered by REs when doped in silica fibres. Thanks to the host-dependent spectroscopic properties, BDFs with different co-dopants such as aluminium (Al), phosphorus (P) and germanium (Ge) with a low or high (>50mol%) concentration can cover wavelength bands around 1.1, 1.3, 1.45 and 1.8 μm respectively [12]. This unique feature enables amplifiers and fibre lasers in wavelength bands that are difficult to achieve with RE-doped silica fibres, with a view to many potential applications such as fibre optic communications, optical fibre sensing, biomedical imaging and so on.

It cannot be denied that there are alternative technologies to achieve laser sources or amplifiers for the wavelength band of 1.1-1.8 μm discussed above. Although some wavelength bands can be achieved by bulk lasers and semiconductor lasers, the fibre laser has certain unique advantages. Initially demonstrated in a Neodymium (Nd)-doped glass fibre in the 1960s [13, 14], the fibre laser gradually replaced many bulk laser sources and became widely used because of its compactness and robustness as the fabrication technique of active-doped fibres developed. Compared to semiconductors which have limited output power, fibre lasers have greater potential for power scaling, with additional attractive features such as the ability for single mode and narrow linewidth operations. Among different types of fibre lasers, although the Raman laser can generate light at many wavelengths, it often necessitates a relatively high pump power to surpass the Raman

threshold. The Raman laser also has drawbacks of limited spectral control in comparison to lasers based on active fibres. In the case of amplifiers, no efficient amplifier with RE-doped fibres has been demonstrated to operate covering the wavelengths region 1.1 to ~1.5 μm and ~1.65 μm. Therefore, there is a high demand for developing BDFs in various glass hosts to cover the wavelength gaps not accessible using RE-doped fibre, for both lasers with high power and good beam quality, and amplifiers with efficient gain and low noise figure. Furthermore, the potential for future power scaling of these laser sources is of vital importance. Concerning the amplifiers, the implementation of a broader operating bandwidth is desirable in conjunction with the existing EDFA-based optical telecommunications system.

Despite the broadband emission of BDFs supports lasers and amplifiers operating over a wide wavelength range, their efficiency is currently limited by the performance of the BDFs used to demonstrate such devices. Additionally, due to the experimentally observed fact that low Bi concentration in BDFs perform better compared to high-concentration, thus long device lengths, sometimes of the order of hundreds of meters, are required to provide sufficient gain for Bi doped fibre lasers and amplifiers (BDFLs and BDFAs). Improving the fibre performance and associated laser/amplifier efficiency requires a proper understanding of the bismuth active centres (BACs) that contribute to the near-IR emission and a reduction of the unsaturable loss (UL) in such fibres.

The primary objective of this project is to develop BDFs with different dopants in a silica host and to build the corresponding fibre lasers operating in different wavelength ranges. This study follows a closed loop sequential approach, starting with (1) the fabrication of BDFs using MCVD-solution doping technique, followed by (2) the characterisation of a number of BDFs produced under different fabrication conditions, (3) the spectroscopic study of the fibres, and (4) the demonstration of BDFLs. Based on the fibre characterisation and laser results, the fabrication conditions were further modified, in terms of deposition temperature, solution content and concentration, collapse atmosphere, and fibre drawing conditions. This study developed both Bi-doped phosphosilicate and aluminosilicate fibres (BPSFs and BASFs) that were used to demonstrate both fibre lasers and amplifiers, with a focus on laser performance in this thesis. Information on BDFAs and related results can be found in [15-18].

1.2 Layout of the thesis

Chapter 1 explains the motivation behind this study of Bi-doped fibres and briefly discusses the challenges and difficulties of the topic.

Chapter 2 reviews the history of development of BDFs and briefly explains the origin of their NIR luminescence. It summarises the improvement of both BDFL and BDFA at different spectral regions.

Chapter 3 introduces the background knowledge about the optical fibre fabrication, including the specific technique so called 'modified-chemical-vapour-deposition (MCVD) combined with solution doping', which is used in this study to manufacture both BPSFs and BASFs. It presents a detailed overview of the general production process, including preform fabrication, analysis, and fibre drawing.

Apart from the review and introduction of fundamental knowledge related to this topic, this study can be generally separated into two modules based on the glass host of BDFs: (1) the study of BPSFs, covering chapter 4 -5 and (2) the study of BASFs, covering chapter 6-8. In each module, the study involves the fibre development and the device demonstration.

Chapter 4 shows the development of the fibre fabrication process, particularly for BPSFs. The modifications made during the preform fabrication are introduced in detail, followed by characterisation of the resulting fibres in terms of both chemical analysis and optical properties.

Chapter 5 details the construction of a laser setup used to evaluate the performance of the BPSFs manufactured in this study. The cavity was modified to achieve the highest possible output power. After optimisation of the BDFL operating at 1340nm, its wavelength-tuning ability was demonstrated using an optical filter and mechanical-tunable fibre Bragg gratings (FBGs). Comprehensive results of the laser output, including power, slope efficiency, and spectrum, are presented in both experimental scenarios.

Similar to Chapter 4, **Chapter 6** introduces the development of BASFs fabrication and the related characterisation of the fibres. The modification of the BASF fabrication involves different parameters in both MCVD process and fibre drawing.

Chapter 7 introduces our spectroscopic study related to BASFs. The study includes measurement of fluorescence spectrum, the lifetime, and cross-section. A methodology for cross-section analysis that can be generally applied to BDFs is presented. Additionally, this chapter discusses a critical phenomenon of visible luminescence in BASFs at new wavelengths, which is believed to be one of the reasons contributing to the low efficiency of BASFs.

The laser performance of in-house fabricated BASFs is presented in **Chapter 8**.

Chapter 9 concludes the contributions of this thesis to knowledge in this field and discusses some potential work for the convenience of researchers studying on BDFs in the future.

With the exception of a few samples created collaboratively with colleagues as part of early project training, the author played a central role in fabricating the majority of preforms and fibres utilised in this study. While the characterisation of the BPSFs was partially carried out by another colleagues, the entire work related to BASFs was conducted by the author.

1.3 Reference

[1] S. B. Poole, D. N. Payne and M. E. Fermann, “Fabrication of low-loss optical fibres containing rare-earth ions,” Electronics Letters, 21(17), 737-738 (1985).

[2] S. Sudo, Optical fibre amplifiers: materials, devices and applications, Artech House, 1997.

[3] R. J. Mears, L. Reekie, I. M. Jauncey and D. N. Payne, “Low-noise erbium-doped fibre amplifier operating at 1.54μm,” *Electronics Letters*, 23(19), 1026-1028 (1987).

[4] M. N. Zervas, C. A. Codemard, “High Power Fiber Lasers: A Review”. IEEE *Journal of Selected Topics in Quantum Electronics*, 20(5), 219-241 (2014).

[5] K. C. Phillips, H. H. Gandhi, E. Mazur,S. K. Sundaram, “Ultrafast laser processing of materials: a review,” *Advances in Optics and Photonics*, 7(4), 684-712 (2015).

[6] S. Popov “7: Fiber laser overview and medical applications,” in Tunable Laser Applications 2nd ed. New York, USA: F. J. Duarte (ed.). CRC (2009).

[7] A. Ghatak, and K. Thyagarajan, “Basic characteristics of the optical fiber,” in An introduction to fiber optics, Cambridge university press. 40(1998).

[8] H. Sakr, Y. Chen, G.T. Jasion, T.D. Bradley, J.R. Hayes, H.C.H. Mulvad, I.A., Davidson, E.Numkam Fokoua, and F. Poletti, “*Hollow core optical fibres with comparable attenuation to silica fibres between 600 and 1100 nm*”. Nature communications, 11(1), 1-10. (2020).

[9] C. E. Max, S. S. Olivier, H. W. Friedman, J. An, K. Avicola, B. V. Beeman, H. D. Bissinger, J. M. Brase, G. V. Erbert, D. T. Gavel et al., “Image improvement from a sodium-layer laser guide star adaptive optics system,” Science, 277(5332),1649-1652 (1997).

[10] C. F. Blodi, S. R. Russell, J. S. Pulido, and J. C. Folk, “Direct and feeder vessel photocoagulation of retinal angiomas with dye yellow laser," Ophthalmology, 97(6), 791-797 (1990).

[11] N. S. Sadick and R. Weiss, “The utilization of a new yellow light laser (578nm) for the treatment of class I red telangiectasia of the lower extremities,” Dermatologic surgery, 28(1), 21-25 (2002).

[12] N. K. Thipparapu, Y. Wang, S. Wang, A. A. Umnikov, P. Barua, and J. K. Sahu, “Bi-doped fiber amplifiers and lasers,” Optical Materials Express, 9(6), 2446-2465 (2019).

[13] E. Snitzer, “Proposed fiber cavities for optical masers,” Journal of Applied Physics, 32(1), 36-39 (1961)

[14] E. Snitzer, “Optical maser action of Nd+ 3 in a barium crown glass,” Physical Review Letters, 7(12), 444-446 (1961)

[15] Y. Wang, N. K. Thipparapu, S. Wang, P. Barua, D. J. Richardson, and J. K. Sahu. “O-band bismuth-doped fiber amplifier and its temperature dependent performance.” In Sixth International Workshop on Specialty Optical Fibers and Their Applications (WSOF 2019), vol. 11206, paper 112061X-1.

[16] Y. Wang, N. K. Thipparapu, S. Wang, P. Barua, D. J. Richardson, and J. K. Sahu. “Study on the temperature dependent characteristics of O-band bismuth-doped fiber amplifier.” Optics Letters 44, no. 23, 5650-5653, (2019).

[17] N. K. Thipparapu, Y. Wang, S. Wang, P. Barua, and J. K. Sahu, “Bi-doped silica-based fiber amplifier for O-band transmission,” in Asia Communications and Photonics Conference (ACPC) 2019, OSA Technical Digest (Optical Society of America, 2019), paper S3G.6.

[18] Y. Wang, S. Wang, A. Halder, and J. Sahu, “Bi-doped optical fibers and fiber amplifiers”. Optical Materials: X, 17, 100219 (2023).

Chapter 2 Introduction to Bi-doped optical fibres

2.1 Introduction

This chapter provides a review of the development of Bi-doped fibres (BDFs) over the past 20 years, highlighting the latest achievement in both Bi-doped fibre lasers (BDFLs) and amplifiers (BDFAs). The study of BDFs has been focused on two main areas: the physical theory of its working mechanism and the device development. This chapter is organised accordingly, beginning with a discussion of the origin of the near-infrared (NIR) luminescence in BDFs in Section 2.2. The subsequent section (2.3) provides a review of BDFLs, covering three areas: (1) Continuous-wave (CW) BDFLs operating at a single wavelength within 1100-1800 nm; (2) Tunable BDFLs; and (3) Pulse BDFLs. In Section 2.4, the progress made on BDFAs is summarised based on the working wavelength, including: (1) 1100-1250 nm; (2) 1260-1360 nm; (3) 1300-1500 nm; (4) 1600-1800 nm.

2.2 Origin of the NIR luminescence in Bi-doped fibres

The doping material Bi in silica fibres has attracted increasing attention from researchers, due to its unique feature of exhibiting host-dependent absorption and emission properties, which is attributed to its distinct fundamental structure as compared to REs. The typical electronic configuration of REs is $(Xe)4f^x5d^ys^2$ (x=0-14, y=0 or 1), where the 4f subshell is partially filled and the 6s subshell is full-filled. As a result, the interactions between the unpaired electrons and the glass host are mostly prevented because the 4f subshell is shielded by the 6s subshell. In comparison, the electronic configuration of Bi is (Xe) $4f^{14}5d^{10}6s^26p^3$, in which the inner subshells are full filled, leaving the outer 6s and 6p electrons to have significant interaction with the surroundings. The host-dependence of Bi has enabled a broad gain bandwidth to be observed from 1.1-1.8 μm, particularly in the silica optical fibres when the host glass is co-doped with Al, P, Ge, or a combination of those.

Historically, the NIR luminescence of Bi-doped silica glass was first discovered in 1999 by Murata et al. at 1132 nm with a full width at half maximum (FWHM) of 150 nm [1]. Since then, significant efforts have been made in the past decades to develop Bi-related glass and optical fibres. However, after over 20 years investigation, the nature of Bi-related NIR

emission remains unclear. One of the main reasons for this is that Bi ions at different valence states can coexist in the glass, including Bi^{+}, Bi^{2+}, Bi^{3+} and Bi^{5+}, as well as Bi clusters and negative Bi dimers, such as Bi_2^{-} and Bi_2^{2-} [2-19]. This makes the manufacturing procedures of BDFs heavily depend on fabrication conditions as the oxidation states of Bi ions can be easily affected by factors such as temperature, atmosphere, and concentration of other elements present in the glass. Table 2.1 lists the hypotheses and related evidence of Bi NIR luminescence origin in the past and current, categorised by the valency states of the Bi-ion.

Table 2.1 Origin of NIR luminescence in Bi-doped glass

Origin of NIR luminescence	Glass composition	Reference
Bi clusters	GeO_2-Ta_2O_5-Bi_2O_3 GeO_2-Al_2O_3-Bi_2O_3	[2]
Bi^0	Bi_2O_3·B_2O_3·SiO_2·PbO Bi_2O_3·B_2O_3·SiO_2·PbO·Sb_2O_3	[3]
Bi^{+}	B_2O_3-BaO-Al_2O_3-Bi_2O_3	[4]
	P_2O_5-Al_2O_3-Bi_2O_3	[5]
	GeO_2-Al_2O_3-Bi_2O_3	[6]
	SiO_2-Al_2O_3-GeO_2-P_2O_5-Bi_2O_3 SiO_2-Al_2O_3-GeO_2-Bi_2O_3 SiO_2-Al_2O_3-Bi_2O_3 GeO_2-SiO_2-Ta_2O_5-P_2O_5-Bi_2O_3	[7]
	SiO_2-GeO_2-Al_2O_3-Bi_2O_3 SiO_2-GeO_2-Bi_2O_3	[8]
	SiO_2-Al_2O_3-GeO_2-P_2O_5-Bi_2O_3 SiO_2-GeO_2-P_2O_5-Bi_2O_3	[9]
Bi^{2+}	GeO_2-SrO-Al_2O_3-Bi_2O_3	[10]
Bi^{5+}	SiO_2-Al_2O_3-GeO_2-P_2O_5-Bi_2O_3 SiO_2-Al_2O_3-GeO_2-Bi_2O_3 SiO_2-Al_2O_3-Bi_2O_3 GeO_2-SiO_2-Ta_2O_5-P_2O_5-Bi_2O_3	[7]
	SiO_2-Al_2O_3-Bi_2O_3	[11]
	Al_2O_3–GeO_2-Na_2O(or BaO, Y_2O_3)-Bi_2O_3	[12]
Negative Bi dimmer Bi_2^{-}, Bi_2^{2-}	SiO_2-Al_2O_3-P_2O_5-Li_2O SiO_2-Al_2O_3-P_2O_5-B_2O_3-Na_2O SiO_2-Al_2O_3-ZnO-MgO-TiO-ZrO_2	[13]
	SiO_2-Al_2O_3-MgO-Bi_2O_3	[14]
$Bi^{5+}O_n^{2-}$	Model	[15]

	Model	[16]
	SiO_2-Al_2O_3-Y_2O_3-Bi_2O_3 + Model	[17]
{$[AlO_{4/2}]^-$, Bi^+}	Al_2O_3-GeO_2-P_2O_5-SiO_2-Bi_2O_3 Al_2O_3-SiO_2-Bi_2O_3	[18]
Point defect	GeO_2-Al_2O_3-Bi_2O_3 (or PbO, In_2O_3, SnO_2, Sb_2O_3, TeO_2)	[19]

Reports of luminescence from Bi-doped glass and crystals related to Bi^{2+} and Bi^{3+} had been previously published [20-23]. However, in those reports, the luminescence was limited at visible wavelengths. After the NIR fluorescence was discovered in Bi-doped glass, Fujimoto et al. refuted the hypothesis that Bi^{2+} and Bi^{3+} were the origin of this new NIR luminescence for the following main reasons [11]: (1) The absorption peaks of their samples were different from those of previous Bi^{3+} doped glasses, and the lifetime of this new fluorescence was two order magnitude longer than that of typical Bi^{3+} ions at room temperature (630μs and 3μs respectively); (2) Electron spin resonance (ESR) measurements failed to detect any signal resulting from unpaired electrons, which would exist if there were Bi^{2+} in the sample. The possibility of impurities as the cause of the NIR luminescence ruled out, and Bi^{5+} was suggested to be responsible for this new feature. This opinion was further supported by experiments showing that the NIR emission increased with Bi^{5+} concentration in three Bi^{5+} doped glass samples [12]. However, later studies found that melting temperature could also have great impact on the optical properties of Bi-doped glass [24]. Therefore, the comparability of the experiment in Ref. [12] was reconsidered since the temperature was not controlled to be identical thus the conclusion was not persuasive. Another hypothesis emerged, suggesting Bi in the lower valency states [4,5] could be the source for the NIR emission based on the energy matching conditions. This hypothesis was later supported by [6-9].

After successful fabrication of BDFs in an aluminosilicate host [18], Dvoyrin et al. hypothesised that the luminescence feature of BDFs was due to the $[AlO_{4/2}]^-$ complex as there was no infrared emission without co-doped Al in the fibre. However, this hypothesis was quickly disproved when a series of Bi fibres co-doped with other elements (P, Ge, or the combination of these dopants) were fabricated and showed amplification in the spectral range of 1.2-1.55 μm [7]. Peng et al. proposed that the emission could come from Bi cluster in the Bi-tantalum (Ta) -co-doped germanium oxide glass [2], while Ren et al.

suggested that the infrared emission could be assigned to BiO molecules in Bi-doped silicate glass [25]. Over the years, several other hypotheses were also proposed, including negative Bi dimers (Bi^{2-}/Bi^{2} [13], Bi^{2-}/Bi_2^{2-} [14]), Bi^{0} [3], and point defects [19]. Some researchers suggested that $Bi^{5+}O_n^{2-}$ molecules could be responsible for the NIR emission using an intramolecular charge transfer model [15-17]. Overall, the most acceptable opinion is that the NIR emission does not come from Bi^{2+} and Bi^{3+} [26], but the exact origin of the Bi-related NIR emission is still a topic of intense debate.

In addition to these hypotheses, another essential concept is the bismuth active centre (BAC) related to the NIR luminescence feature. Nowadays, it is believed that different types of BACs can be formed and exist in the glass depending on the glass composition. Energy level diagrams for BACs formed together with other elements (such as Si, Al, P, Ge) associated with NIR luminescence have been predicted as shown in Figure 2.1 [27-29]. These predictions were determined from absorption and luminescence properties of the BDFs, by measuring the intensity of fluorescence light in a wide spectrum range when the fibre was pumped at different wavelengths. Supercontinuum laser sources were used to sweep the excitation wavelength continuously from 450-1700 nm and 250-900 nm.

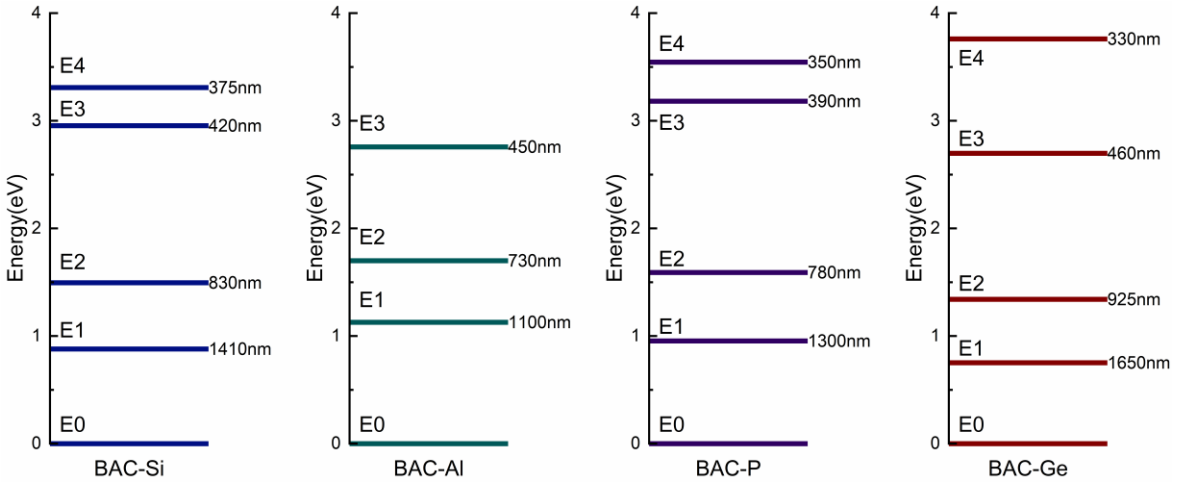

Figure 2.1 Predicted energy level diagrams of BACs associated with Si, Al, P and Ge

Despite numerous experimental and theoretical studies, none of the hypotheses proposed so far has been completely validated. Therefore, there is a need for additional fundamental research on the Bi-related NIR luminescence in optical fibres to improve the manufacturing of the fibres and the design and modification of related devices.

2.3 State of art of the Bi-doped fibre lasers

Research on Bi-doped NIR-emitting glasses and optical devices has experienced rapid growth since the discovery of the NIR luminescence of Bi-doped silica glass. This section will focus on the progress in the optical fibre laser field, particularly for CW BDFLs, tunable BDFLs and pulsed BDFLs operating in the range of 1.1-1.8 μm.

2.3.1 State of art of continuous-wave Bi-doped fibre lasers

In 2005, for the first time, BDFs were successfully fabricated by Dianov et al. using the modified-chemical-vapour-deposition (MCVD)-the solution doping technique [18]. Two fibres were manufactured with composition of $1Al_2O_3$-$9GeO_2$-$2P_2O_5$-$88SiO_2$ (BAGPSF) and $10Al_2O_3$-$90SiO_2$ (BASF), with bismuth oxide (Bi_2O_3) concentration of 0.002 and 0.03mol%, respectively. The BASF fibre showed broad absorption bands peaking at 700, 800 and 1000 nm, while these bands were slight red-shifted in the BAGPSF. In addition, the fluorescence spectrum of the BASF was observed at 750 and 1060 nm, with the FWHM of 100 and 200 nm, respectively. The BAGPSF also exhibited similar fluorescence properties with the second peak shifted to 1160 nm. Subsequently, a continuous-wave (CW) lasing was established using this type of BASFs [30]. The laser cavity was formed by two Bragg gratings and pumped by a Nd: YAG laser at 1064 nm with an output power of 5 W. A maximum laser output power of 460 mW at 1146 nm and 400 mW at 1215 nm was reported, with corresponding slope efficiencies of 10.2% and 14.3%, respectively. A few years later, Bi-doped phosphogermanosilicate fibres (BPGSFs) were used to demonstrate a BDFL lasing in the range of 1300-1470 nm, which was pumped at 1205, 1230 and 808 nm [31]. The laser was monitored at two temperatures, 300 K and 77 K, and the laser slope efficiency was found strongly dependent on the temperature, with values less than 5% in all cases. At the lasing wavelength of 1310 nm, the slope efficiency increased with reduced temperatures, while an opposite trend was observed at 1345 nm. Later, an operating wavelength range of 1470-1550 nm was also reported by pumping BPGSFs and Bi-doped germanosilicate fibres (BGSFs) at 925 nm and 1230 nm [32]. Under 1230 nm pumping at room temperature, lasing peaks were observed at 1500 nm and 1520 nm with a 30 m BPGSF, which exhibited a slope efficiency of 4.2% and 1.6%. Under the similar condition, a 30 m BGSF also demonstrated lasing at 1500 nm with the efficiency of 3%. When pumped at 926 nm, lasing

at 1550 nm was observed with BPGSF, although the slope efficiency was failed to be measured as the limited pump power exceeded only the threshold value.

The initial studies indicated the high potential of BDFs for the development of devices operating in the NIR. Significant efforts have been made to increase the fibre efficiency as well as extend the bandwidth. The presence of unsaturable loss (UL) in BDFs has been suggested as an important factor for the poor laser efficiency of BDFLs, which will be discussed in later chapters. Table 2.2 summarises the published BDFLs so far, including lasing and pumping wavelengths (λ_s and λ_p), output power (P_{out}) and slope efficiency (η) with respect to the launched or absorbed pump powers as marked by L or A respectively.

Table 2.2 List of BDFLs in the range of 1.1-1.5μm

λ_s(nm)	λ_p(nm)	P_{out}(mW)	η(%)	Note	Ref.
1146 1215	1064	460 400	10 14	L	[30]
1150 1160 1205 1215	1070	13000 15000 5000 4500	19 22 7 13	A	[33]
1160	1068 1075 1090	3000 3600(T=300K) 8600(T=77K) 5000(T=300K) 8400(T=77K)	22 21 (T=300K) 52 (77K) 28 (T=300K) 50 (77K)	A	[34]
1150 1200	1060	300 550	14 24	L	[35]
1160 1146	1064	300	10	A	[36]
1178	1070	6400	15	A	[37]
1150 1160	1070	1300 1500	19 21	A	[38]
1310 1310 1345 1470	1205 1230 1230 1230	2.5 18 5 28	1.4 (T=300K) 5.4 (77K) 3.2 (T=300K) 5.0 (77K) 0.8 (T=300K) 0.6 (77K) 3.4	A	[31] [39]
1330 1480	1230 1340	2500 2000	24 23	A	[40]
1280 1330 1340 1360 1480	1230 1230 1230 1230 1340	8900 1060 8800 5230 1940	31 37 31 18 21	A	[41]
1500 1520 1550	1230 1230 925	80 40 At threshold	4.2 1.6 -	A	[32]
1389 1480	1340	2200 8000	36 65	A	[42]

1500 1538		4000 1600	68 35		
1703	1568	560	20	L	[43]
1705	1568	1050	33	L	[44] [45]
1730	1568	15 45	5 13(thermal treatment)	L	[46]
1460	1340	400	41(PANDA)	L	[42]
1460	1310	3000	72(W-type fibre)	L	[47]
1460	808	50	0.2(cladding pump)	L	[48] [49]
1360 1460	793 808	300 150	1.4(cladding pump)	L	[50]

In the wavelength range of 1.1-1.3 μm, the maximum slope efficiencies were 28% at room temperature (300K) and 50% at 77 K at 1160 nm [34]. The output power and slope efficiency were found to be strongly dependent on temperature, with values roughly doubling when the fibre was cooled from room temperature to 77 K. The CW laser demonstrated was later applied for yellow light generation using frequency-doubling technique [36-38]. Currently, the maximum laser output power reported within 1.1-1.3 μm is around 15 W at 1160 nm with a slope efficiency of 22% with respect to absorbed pump power.

In the wavelength range of 1.3-1.5 μm, Bufetov et al. found that the laser slope efficiency depended significantly on the pump power level [41]. Two BPGSFs were pumped by a Raman laser operating at 1230 nm with 28 W power, resulting in 10.6 W output power at 1330 nm. It was observed that the slope efficiency increased from 17% to 50% at lower and higher pump power levels, respectively. A spectrum broadening was also observed at the output under high-power pumping.

The study of BDFLs has also made progress in extending the spectral range to 1.6-1.8 μm [43]. By increasing the concentration of Ge to >50mol%, luminescence at 1700 nm was observed when the excitation wavelength was around 460, 950, and 1600 nm. Using this high-Ge-doped fibre, a BDFL operating at 1703 nm with a slope efficiency of 20% and an output power of 560 mW was demonstrated [43]. The pump power was 3 W, and the pumping wavelength was 1568 nm. Several BDFLs operating in this wavelength range were later developed to the Watt-level and showed a maximum slope efficiency of 33% [44,45].

In recent years, there has been a shift in the development of BDFLs towards exploring the potential of modifying the fibre refractive index profile. This approach has shown promising results in significantly enhancing the performance of BDFLs. A PANDA-type polarisation maintaining BDFs was demonstrated with a 41% slope efficiency with respected to the launched power at 1460 nm [42]. A W-type graded-index BDFs was fabricated and improved the laser performance significantly with a 72% slope efficiency at 1460 nm [47]. Additionally, some preliminary results related to double-cladded BDFs have been reported, which show potential for future power scaling in BDFLs [48-50].

2.3.2 State of art of tunable Bi-doped fibre lasers

In the past, only a limited number of tunable BDFLs have been reported, despite their potential for applications in fibre-optic communications, sensing, and medical fields. Figure 2.2 provides a summary of published tunable BDFLs across different wavelength bands. One tunable BDFL based on a BGSF and an external diffraction grating was reported to operate from 1366-1507 nm [51]. This laser demonstrated output power ranging from 25 to 50 mW across the tuning bandwidth, using 300 mW of pump power at 1340 nm. Another tunable laser operating within the range of 1.65-1.8 µm was also demonstrated, using a BGSF with a high Ge concentration (>50%), with 300 mW pump light at 1564 nm [52]. The maximum output power was 6 mW at 1.7 µm.

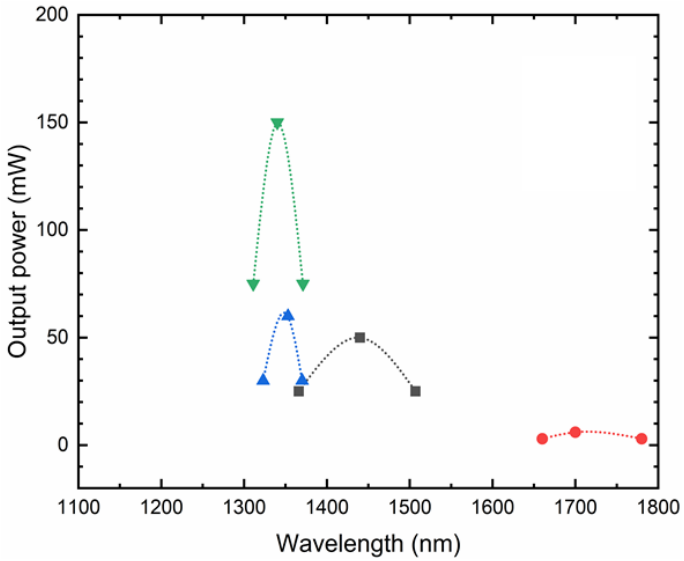

Figure 2.2 Output power and bandwidth of reported tunable BDFLs. Each curve represents one published result which can be found in [51-54].

Our group recently reported a BDFL tunable from 1315 to 1375 nm, which was pumped at 1270 nm using a BPSF as gain medium in a ring laser cavity [53]. The BDFL had a maximum output power of 60 mW and a slope efficiency of 10% at 1353 nm. The output power was further increased to 138 mW with the help of a Bi-doped fibre amplifier (BDFA). Subsequently, by improving the BDFs and further optimising the laser cavity, we demonstrated a tunable BDFL with a tuning range of 1305-1375 nm and a maximum output power of 150 mW without any additional amplification of the output light [54]. The laser's tuning was achieved using an optical filter, and its slope efficiency exceeded 25% in a 60 nm bandwidth from 1311 to 1371 nm. In parallel, another tunable BDFL was also reported with a similar output power in the 50 nm tuning bandwidth from 1320 to 1370 nm, using a mechanically-tuned fibre Bragg grating (FBG) [55,56].

2.3.3 State of art of Bi-doped fibre pulsed laser

The broad gain bandwidth of BDFs enables the development of pulsed lasers using Q-switch or mode-locking techniques. Table 2.3 and

Table 2.4 summarise the reported pulsed BDFLs, including their operating wavelength (λ_s), pulse-width (t_p), repetition rate (R), average pulse power (P_{ave}), and pulse generation mechanism. Active-mode-locked BDFLs used acousto-optic modulators (AOMs) [71,76], while passive mode-locked BDFLs were realised by using different saturable absorbers, such as carbon nanotubes (CNT) [61, 67, 72], single-walled carbon nanotubes (SWCNT) [65], semiconductor saturable absorbed mirror (SESAM) [57-60,62,63,70,74], non-linear amplifying loop mirror (NALM) [64,73], non-linear optical loop mirror (NOLM) [64], and nonlinear polarisation rotation (NPR) [75]. Pulsing can even be achieved by the BDF itself [66,68,69], as the unsaturable loss (UL) of the fibre can act as a natural absorber in the cavity.

In 2007, the first pulsed BDFL was demonstrated successfully using a 6m BDF and a SESAM [57]. The laser generated pulses at a wavelength of 1162 nm with a pulse width of 50 ps and an average power of 2 mW, which was pumped by an Ytterbium-doped fibre laser with ~800 mW power at 1064 nm. The repletion rate of the pulse was 13 MHz. Since then, BDFs co-doped with Al, P, and Ge have been utilised to demonstrate pulsed lasers at 1100-1250 nm, 1300-1500 nm, and 1600-1800 nm, respectively. For the 1100-1250 nm range, a pulsed BDFL based on a SESAM and a master oscillator power amplifier (MOPA) exhibited a pulsed

output of 150 mW average power at 1177 nm [62]. The output was then frequency doubled at 588 nm with a power of 13.7 mW. For the 1300-1500 nm wavelength range, the shortest pulse reported had a duration of 240 fs at a repetition rate of 20 MHz, achieved through a CNT and MOPA system. The peak power of the output was 3.1 KW [67]. In 2016, the first pulsed BDFL operating at 1.7 μm was demonstrated using a CNT as the saturable absorber [72]. Another pulsed BDFL at 1.7 μm was later developed with a 630 ps pulse duration and a 20 mW average power, utilising a NALM and further pulse amplification and compression [73]. Furthermore, several tunable pulsed BDFLs were demonstrated at the wavelengths of 1153-1170 nm [74, 75] and 1310-1370 nm [76].

Table 2.3 Summary of pulsed BDFLs results

λ_s: Operating signal wavelength, $t_{p:}$ pulse-width, R: repetition rate, $P_{ave:}$ average pulse power; '-' was used where the data is not given in the reference.

λ_s(nm)	**t_p(ps)**	**R(MHz)**	**P_{ave}(mW)**	**Mechanism**	**Reference**
1162	50	13	2	SESAM	[57]
1162	1.9	6	4~6	Chirped FBG+SESAM	[58]
1180	5	2.4	0.56	SESAM	[59]
1158-1168	1.1	-	0.3	SESAM	[60]
1177	4.7	5	0.015	Chirped FBG+CNT	[61]
1177	28	9.1	150	SESAM+MOPA	[62]
588.75			13.7		
1320	2.51	2.5	0.3	SESAM	[63]
1300-1340	11.3	3.5	6	NOLM/NALM+MOPA	[64]
	0.53		30		
1320	7.8	10	1.15	SWCNT	[65]
1340	1.2	6.3	18	Self-mode-lock+MOPA	[66]
1440	0.24	20	15	CNT+MOPA	[67]
1463	1.8×10^{6}	6.5×10^{-2}	20	Self-Q-switch	[68]
1470	4.7×10^{6}	3.15×10^{-2}	0.1	Self-Q-switch/ Q-switch-mode-lock	[69]
	1.2×10^{3}	3.088			
1450	0.9	9	-	SESAM	[70]
1450	1.89	9	-	AOM	[71]
1700	1.65	4	10	CNT	[72]
1700	17	3.57	0.3	NALM	[73]
	0.63		20.4	Amplify+compress	

Table 2.4 Summary of tunable pulsed BDFLs

λ_s(nm)	Min. t_p(ps)	R(MHz)	P_{ave}(mW)	Mechanism	Reference
1153-1170	0.9	7.5	-	SESAM	[74]
1153-1174	21.4	4.254	-	NPR	[75]
1300-1370	1.3×10^4	1.683	101	AOM+MOPA	[76]

2.4 State of art of Bi-doped fibre amplifiers

BDFs have found an essential application in amplifier development, particularly for extending the working bandwidth and increasing the capacity of optical fibre telecommunication. The operation wavelength for modern telecom systems can be classified into various bands, including O-band (1260-1360 nm), E-band (1360-1460 nm), S-band (1460-1530 nm), C-band (1530-1565 nm), and L-band (1565-1625 nm), which are defined by the ITU-T standard. While erbium-doped fibre amplifiers (EDFAs) are commonly used in the C-band and L-band, no efficient amplifier has been widely used for other bands. Therefore, huge efforts have been devoted to developing BDFAs that operate in O-, E-, and S- band, as well as in the extended spectral range of 1100-1250 nm and 1600-1800 nm. The performance of these BDFAs is summarised in Table 2.5, including the maximum gain and the wavelength, the operation band and its corresponding bandwidth, input signal and noise figure.

Table 2.5 Summary of BDFA parameters

λ_{gmax}: wavelength with maximum gain; BW: bandwidth; P_s: input signal power; NF_{min}: minimum noise figure; '-' used where the data is not mentioned in the reference.

λ_{gmax}(nm)	G_{max}(dB)	Operating band			P_s (dBm)	NF_{min} (dB)	Ref.
		Range(nm)	BW(nm)	Note			
1160	6.3 (T=300K) 21.2 (T=77K)	Single λ			-6	-	[77]
1180	11.5	Single λ			-4	-	[78]
1321	24	1305-1342	37	3dB	-25	4-6	[41]
1340	25 29	1320-1360	40	1dB	-10 -30	4-6	[79]
1340	39	1330-1360	30	1dB	-23	6	[80, 81]
1340	40	1300-1360	60	Min~Max	-23	4.8	[82]

	45 (T=-60°C)				-30	4	
1330	30	1287-1354	67	85%	-	7	[83]
1296	19	1272-1310	80	2dB	-6	5	[84, 85]
1320	>25	1302-1345	43	3dB	-25	5-6	[86, 87]
1343	13 (on-off)	1240-1485	245	Min~Max	-	-	[31]
1430	24	1414-1450	36	3dB	-20	6	[88, 89]
1360 1410	26	1306-1441	135	3dB	-	7.3	[90,91]
1420	31	1345-1460	115	>20dB	-23	4.8	[92]
1430	38	1410-1450	40	3dB	-23	6	[93]
1334	30.6	1325-1441	116	3dB	-23	5.6	[94-96]
1442	21	1427-1461	34	3dB	-25	4-6	[41]
1430	30.6	1405-1460	55	>20dB	-20	4.75	[97,98]
1430	29.5	1300-1467	67	>20dB	-20	4.6	[47]
1710	23	1697-1737	40	3dB	-20	7	[99,100]
1651 1687	18 26	Single wavelength			-16	-	[101]

Figure 2.3 illustrates the maximum gain of these BDFAs, along with their bandwidth over the 1.1-1.8 μm spectral range. Note that the O-, E-, and S-bands are marked on the figure, whereas the S- and C-bands were omitted since EDFAs are commonly used in those regions, and no BDFA has been developed in this area. The single star point represents the BDFA whose gain was measured only at a single wavelength.

In the O-band, the highest gain achieved to date was demonstrated in [82] at 1340 nm, with gains of 45 dB and 40 dB at temperatures of -60 °C and room temperature, respectively. A 60nm bandwidth was reported from 1300 to 1360 nm in the BDFA. In 2008 [31], the positive on-off gain was observed in a BPGSF covering both O- and E- bands from 1240 to 1485 nm. Since then, efforts have been made to extend the operating wavelength to the shorter side of the O-band within the range of 1260-1310 nm and to the longer side to E-band. Amplification was proven at the wavelength of 1280-1370 nm in [41], with a 37 nm 3 dB bandwidth centred at 1321 nm. In [86], another BDFA was developed with only 36 m BPSF, operating from 1287-1354 nm with a maximum gain of 30 dB, with a 3 dB bandwidth of >40 nm. To cover the entire O-band, a BDFA was demonstrated with a 6 dB bandwidth of 80 nm and a maximum gain of 19 dB at a wavelength centred flexibly at 1305-1325 nm [84, 85]. Regarding the E-band BDFA, a maximum gain of 38 dB was achieved at 1430 nm

with an input signal power of -23 dBm. The 3 dB bandwidth was 40 nm. More importantly, BDFAs covering both O- and E- bands were under deep investigation, with results discussed in [90-92, 94-96]. In addition to standard optical fibre telecom bands, BDFAs also demonstrate amplification in extended spectral range of 1100-1250 nm and 1600-1800 nm [77,78,99-101].

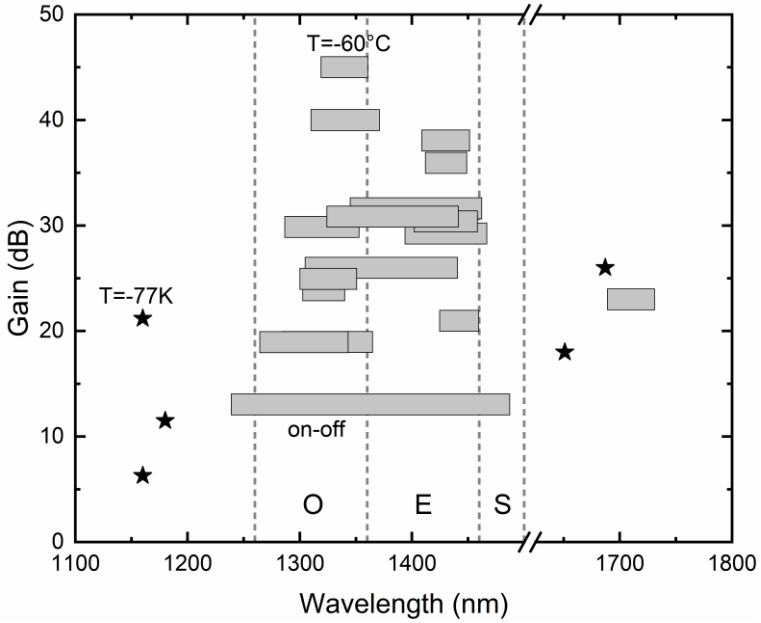

Figure 2.3 Operation wavelength and maximum gain of BDFAs demonstrated so far [31, 41, 47, 77-101]. Star point: amplification only measured at a single wavelength. Special conditions including low temperatures and on-off gain are marked.

2.5 Conclusion

This chapter provides an overview of the current research state of BDFs, including the discussion of the NIR luminescence origin, and the introduction of two main applications of BDFs: BDFL and BDFA. Significant progress has been made in the development of these fibres and the devices, to achieve the higher output power and efficiency of the laser as well as the higher gain and broader bandwidth of the amplifier. For BDFLs, CW and broadband tunable BDFLs have been demonstrated operating in the spectra range of 1.1-1.8μm. Pulsed lasers with pulse duration at ps/fs level have also been developed. Meanwhile, BDFAs have been successfully demonstrated in a wide spectral range in the O, E, S-bands, with over 20dB gain in most situations, as shown in Figure 2.3. Amplification in the shorter side of 1.1-1.2 μm and the longer side of 1,7-1.8μm has also been approved

and under progress, which can further enhance the capabilities of optical fibre telecommunications. These achievements not only demonstrate the enormous potential of BDFs, but also encourage further research to improve their performance in the future. Additionally, efforts have also been made to reduce the fibre length used in the system, which is a crucial challenge in enhancing BDFs-based devices. This is because fibres with higher Bi concentration and NIR absorption tends to exhibit high UL at the pump wavelength, comparing to low Bi-doped fibres. Overall, the development of BDFs still leaves a vast space that requires researchers to conduct in-depth investigations into the underlying physics and mechanisms.

2.6 Reference

[1] K. Murata, Y. Fujimoto, T. Kanabe, H. Fujita, and M. Nakatsuka, "Bi-doped SiO2 as a new laser material for an intense laser," *Fusion engineering and design*, **44**(1-4), 437-439 (1999).

[2] M. Peng, J. Qiu, D. Chen, X. Meng, and C. Zhu, "Superbroadband 1310 nm emission from bismuth and tantalum codoped germanium oxide glasses," *Optics Letters*, **30**, 2433-2435 (2005)

[3] M. Peng, C. Zollfrank, and L.Wondraczek, "Origin of broad NIR photoluminescence in bismuthate glass and Bi-doped glasses at room temperature." *Journal of Physics: Condensed Matter*, **21**(28), 285106 (2009).

[4] X. Meng, J. Qiu, M. Peng, D Chen, Q Zhao, X Jiang, and C. Zhu, "Infrared broadband emission of bismuth-doped barium-aluminum-borate glasses," *Optics Express* **13**, 1635-1642 (2005)

[5] X. Meng, J. Qiu, M. Peng, D. Chen, Q. Zhao, X. Jiang, and C. Zhu, "Near infrared broadband emission of bismuth-doped aluminophosphate glass," *Optics Express* **13**, 1628-1634 (2005)

[6] M. Peng, J. Qiu, D. Chen, X. Meng, I. Yang, X. Jiang, and C. Zhu, "Bismuth-and aluminum-codoped germanium oxide glasses for super-broadband optical amplification." *Optics letters*, **29**(17), 1998-2000 (2004).

[7] V. V. Dvoyrin, V. M. Mashinsky, L. I. Bulatov, I. A. Bufetov, A. V. Shubin, M. A. Melkumov, E. F. Kustov, E. M. Dianov, A. A. Umnikov, V. F. Khopin, M. V. Yashkov, and A. N. Guryanov,

"Bismuth-doped-glass optical fibers-a new active medium for lasers and amplifiers," *Optics Letters* **31**, 2966-2968 (2006)

[8] Y. Qiu, and Y. Shen, "Investigation on the spectral characteristics of bismuth doped silica fibers." *Optical Materials*, **31**(2), 223-228 (2008)

[9] V.G. Truong, L. Bigot, A. Lerouge, M. Douay, and I. Razdobreev, "Study of thermal stability and luminescence quenching properties of bismuth-doped silicate glasses for fiber laser applications." *Applied Physics Letters*, **92**(4), 041908 (2008).

[10] J. Ren, J. Qiu, D. Chen, X. Hu, X. Jiang, and C. Zhu, "Ultrabroad infrared luminescence from Bi-doped aluminogermanate glasses." *Solid state communications*, **141**(10), 559-562 (2007).

[11] Y.Fujimoto, and M. Nakatsuka, "Infrared luminescence from bismuth-doped silica glass." *Japanese Journal of Applied Physics*, **40**(3B), L279 (2001).

[12] H.P. Xia, and X.J. Wang, "Near infrared broadband emission from Bi^{5+}-doped Al_2O_3-GeO_2-X (X= Na_2O, BaO, Y_2O_3) glasses." *Applied physics letters*, **89**(5), 051917 (2006).

[13] S. Khonthon, S. Morimoto, Y. Arai, and Y. Ohishi, "Luminescence characteristics of Te- and Bi-doped glasses and glass-ceramics." *Journal of the Ceramic Society of Japan*, **115**(1340), 259-263 (2007).

[14] V. O. Sokolov, V. G. Plotnichenko, and E. M. Dianov, "Origin of broadband near-infrared luminescence in bismuth-doped glasses," *Optics Letters*, **33**, 1488-1490 (2008)

[15] E.F. Kustov, L.I. Bulatov, V.V. Dvoyrin, and V.M. Mashinsky, "Molecular orbital model of optical centers in bismuth-doped glasses." *Optics letters*, **34**(10), 1549-1551 (2009).

[16] E.F. Kustov, L.I. Bulatov, V.V. Dvoyrin, V.M. Mashinsky, and E.M. Dianov, "Crystal field and molecular orbital theory of MBm centres in glasses." *Journal of Physics B: Atomic, Molecular and Optical Physics*, **43**(2), 025402 (2010).

[17] I. Razdobreev, V.Y. Ivanov, L. Bigot, M. Godlewski, and E.F. Kustov, "Optically detected magnetic resonance in bismuth-doped silica glass." *Optics Letters*, **34**(17), 2691-2693 (2009).

[18] V. V. Dvoyrin, V. M. Mashinsky, E. M. Dianov, A. A. Umnikov, M. V. Yashkov and A. N. Guryanov, "Absorption, fluorescence and optical amplification in MCVD bismuth-doped silica glass optical fibres," 31st European Conference on Optical Communication,(ECOC 2005), pp. 949-950 (2005)

[19] M.Y. Sharonov, A.B. Bykov, V. Petricevic, and R.R. Alfano, "Spectroscopic study of optical centers formed in Bi^{-}, Pb^{-}, Sb^{-}, Sn^{-}, Te^{-}, and In-doped germanate glasses." *Optics Letters*, **33**(18), 2131-2133 (2008).

[20] P. Jeyagopal, R. Jaganathan, M. Kottaisamy, K.R. Kannan, and R.L. Narayanan, "Luminescence of Bi^{3+} in boron rich La_2O_3 CaO B_2O_3 (glass and crystalline) ternary system." *Materials research bulletin*, **26**(6), 481-486 (1991).

[21] C.H. Kim, H.L. Park, and S.I. Mho, "Photoluminescence of Eu^{3+} and Bi^{3+} in $Na_3YSi_3O_9$." *Solid state communications*, **101**(2), 109-113 (1997).

[22] A.M. Srivastava, "Luminescence of divalent bismuth in M^{2+} BPO_5 (M^{2+}= Ba^{2+}, Sr^{2+} and Ca^{2+})." *Journal of Luminescence*, **78**(4), 239-243 (1998).

[23] M. Wang, X. Fan, and G. Xiong, "Luminescence of Bi^{3+} ions and energy transfer from Bi^{3+} ions to Eu^{3+} ions in silica glasses prepared by the sol-gel process," *Journal of Physics and Chemistry of Solids*, **56**(6), 859-862 (1995)

[24] G. Yang, D. Chen, J. Ren, Y. Xu, H. Zeng, Y. Yang, and G. Chen, "Effects of melting temperature on the broadband infrared luminescence of Bi-doped and Bi/Dy co-doped chalcohalide glasses." *Journal of the American Ceramic Society*, **90**(11), 3670-3672 (2007).

[25] J. Ren, L. Yang, J. Qiu, D. Chen, X. Jiang, and C. Zhu, "Effect of various alkaline-earth metal oxides on the broadband infrared luminescence from bismuth-doped silicate glasses." *Solid state communications*, **140**(1), 38-41 (2006).

[26] M. Peng, G. Dong, L. Wondraczek, L. Zhang, N. Zhang, and J. Qiu, "Discussion on the origin of NIR emission from Bi-doped materials," *Journal of Non-Crystalline Solids*, 357(11), 2241-2245 (2011).

[27] S. V. Firstov, V. F. Khopin, I. A. Bufetov, E. G. Firstova, A. N. Guryanov, andE. M. Dianov, "Combined excitation-emission spectroscopy of bismuth active centers in optical fibers," *Optics Express*, **19**(20), 19551-19561(2011).

[28] E. G. Firstova, I. A. Bufetov, V. F. Khopin, V. V. Vel'miskin, S. V. Firstov, G. A. Bufetova, K. N. Nishchev, A. N. Gur'yanov, and E. M. Dianov, "Luminescence properties of IR-emitting bismuth centres in SiO2-based glasses in the UV to near-IR spectral region," *Quantum Electronics*, **45**, 59-65(2015).

[29] A. M. Khegai, S. V. Alyshev, A. S. Vakhrushev, K. E. Riumkin, A. A. Umnikov, and S. V. Firstov. "Recent advances in Bi-doped silica-based optical fibers: A short review." *Journal of Non-Crystalline Solids: X* 100126(2022).

[30] E.M. Dianov, V.V. Dvoyrin, V.M. Mashinsky, A.A. Umnikov, M.V. Yashkov, and A.N. Gur'yanov, "CW bismuth fibre laser," *Quantum Electronics*, **35**(12), 1083(2005).

[31] I.A. Bufetov, S.V. Firstov, V.F. Khopin, O.I. Medvedkov, A.N. Guryanov, and E.M. Dianov, "Bi-doped fiber lasers and amplifiers for a spectral region of 1300-1470 nm," *Optics letters*, **33**(19), 2227-2229 (2008).

[32] E.M. Dianov, S.V. Firstov, V.F. Khopin, O.I. Medvedkov, A.N. Guryanov, and I.A. Bufetov, "Bi-doped fibre lasers operating in the range 1470–1550nm," *Quantum electronics*, **39**(4), 299 (2009).

[33] E. M. Dianov, A. V. Shubin, M. A. Melkumov, O. I. Medvedkov, and I. A. Bufetov, "High power CW bismuth fiber lasers," *Journal of the Optical Society of America B* **24**(8), 1749–1755 (2007).

[34] V. V. Dvoyrin, V. M. Mashinsky, and E. M. Dianov, "Efficient bismuth-doped fiber lasers," *IEEE Journal of Quantum Electronics* **44**(9), 834–840 (2008).

[35] I. Razdobreev, L. Bigot, V. Pureur, A. Favre, G. Bouwmans, and M. Douay, "Efficient all-fiber bismuth-doped laser," *Applied Physics Letters* **90**(3), 031103 (2007).

[36] E. M. Dianov, V. V. Dvoyrin, V. M. Mashinsky and O. I. Medvedkov, "Yellow frequency-doubled bismuth fibre laser," 2006 European Conference on Optical Communications, pp. 1-2, France, 2006

[37] A. B. Rulkov, A. A. Ferin, S. V. Popov, J. R. Taylor, I. Razdobreev, L. Bigot, and G. Bouwmans, "Narrow-line, 1178nm CW bismuth-doped fiber laser with 6.4W output for direct frequency doubling," *Optics Express* **15**, 5473-5476 (2007)

[38] I. A. Bufetov, and E. M. Dianov, “Bi-doped fiber lasers,” *Laser physics letters*, **6**(7), 487 (2009).

[39] E. M. Dianov, S. V. Firstov, V. F. Khopin, A. N. Gur'yanov, and I. A. Bufetov, “Bi-doped fibre lasers and amplifiers emitting in a spectral region of 1.3 μm”. *Quantum Electronics*, **38**(7), 615 (2008).

[40] S. V. Firstov, I. A. Bufetov, V. F. Khopin, A. Shubin, A. V. Smirnov, L. D. Iskhakova, N. N. Vechkanov, A. N. Guryanov, and E. M. Dianov, “2W bismuth doped fiber lasers in the wavelength range 1300-1500 nm and variation of Bi-doped fiber parameters with core composition,” *Laser Physics Letters* 6(9), 665–670 (2009).

[41] I. A. Bufetov, M. A. Melkumov, V. F. Khopin, S. V. Firstov, A. V. Shubin, O. I. Medvedkov, A. N. Guryanov, and E. M. Dianov, “Efficient Bi-doped fiber lasers and amplifiers for the spectral region 1300-1500 nm,” *Fiber Lasers VII: Technology, Systems, and Applications* SPIE, 7580, 758014 (2010)

[42] A. V. Shubin, I. A. Bufetov, M. A. Melkumov, S. V. Firstov, O. I. Medvedkov, V. F. Khopin, A. N. Guryanov, and E. M. Dianov, “Bismuth-doped silica-based fiber lasers operating between 1389 and 1538 nm with output power of up to 22 W,” *Optics Letters* **37**, 2589-2591 (2012)

[43] S. Firstov, S. Alyshev, M. Melkumov, K. Riumkin, A. Shubin, and E. Dianov, “Bismuth-doped optical fibers and fiber lasers for a spectral region of 1600–1800 nm,” *Optics Letters*. **39**, 6927-6930 (2014)

[44] S. V. Firstov, S. V. Alyshev, K. E. Riumkin, M. A. Melkumov, O. I. Medvedkov, and E. M. Dianov, “Watt-level, continuous-wave bismuth-doped all-fiber laser operating at 1.7 μm,” *Optics Letters*, **40**, 4360-4363 (2015)

[45] E. Dianov, S. Firstov, V. Khopin, S. Alyshev, K. Riumkin, A. Gladyshev,M. Melkumov, N. Vechkanov, and A. Guryanov, “Bismuth-doped bers and berlasers for a new spectral range of 1600-1800 nm,” *Fiber Lasers XIII: Technology,Systems, and Applications*, 9728, 97280U, International Society for Optics and Photonics, 2016.

[46] A. Kharakhordin, S. Alyshev, E. Firstova, A. Lobanov, V. Khopin, A. Khegai, M. Melkumov, A. Guryanov, and S. Firstov, "Lasing properties of thermally treated GeO2-SiO2 glass fibers doped with bismuth," *Applied Physics B*, **126**(5), 1-8 (2020).

[47] A. S. Vakhrushev, A. A. Umnikov, A. S. Lobanov, E. G. Firstova, E. B. Evlampieva, K. E. Riumkin, A. V. Alyshev, A. M. Khegai, A. N. Guryanov, L. D. Iskhakova, M. A. Melkumov, and S. V. Firstov, "W-type and Graded-index bismuth-doped fibers for efficient lasers and amplifiers operating in E-band," *Optics Express* **30**, 1490-1498 (2022)

[48] A. S. Vakhrushev, A. V. Kharakhordin, Ya Zh Ososkov, A. M. Khegai, S. V. Alyshev, K. E. Riumkin, E. G. Firstova, M. A. Melkumov, and S. V. Firstov. "Cladding-pumped bismuth-doped fiber laser with brightness enhancement." In *2022 International Conference Laser Optics (ICLO)*, pp. 1-1. IEEE, 2022.

[49] S. Firstov, A. Umnikov, A. Kharakhordin, A. Vakhrushev, E. Firstova, S. Alyshev, A. Khegai, K. Riumkin, Y. Ososkov, A. Guryanov, and M. Melkumov, "Cladding-pumped bismuth-doped fiber laser," *Optics Letters*, **47**, 778-781 (2022)

[50] A. Vakhrushev, Y. Ososkov, S. Alyshev, A. Khegai, A. Umnikov, F. Afanasiev, K. Riumkin, E. Firstova, A. Guryanov, M. Melkumov, and S. Firstov, "Output power saturation effect in cladding-pumped bismuth-doped fiber lasers". *Journal of Lightwave Technology*, **41**(2), 709-715 (2022).

[51] V. M. Paramonov, M. I. Belovolov, V. F. Khopin, A. N. Gur'yanov, S. A. Vasil'ev, O. I. Medvedkov, M. A. Mel'kumov, and E. M. Dianov, "Bismuth-doped fiber laser continuously tunable within the range from 1.36 to 1.51μm," *Quantum Electronics*, **46**, 1068-1070 (2016).

[52] V. M. Paramonov, S. A. Vasil'ev, O. I. Medvedkov, S. V. Firstov, M. A. Melkumov, V. F. Khopin, A. N. Gur'yanov, and E. M. Dianov, "Continuous-wave bismuth fiber laser tunable from 1.65 to 1.8 μm," *Quantum Electronics*, **47**, 1091–1093 (2017).

[53] N. K. Thipparapu, S. Wang, A. A. Umnikov, P. Barua, and J. K. Sahu, "All-fiber Bi-doped laser continuously tunable from 1317-1375nm," in *Conference on Lasers and Electro-Optics Europe and European Quantum Electronics Conference, OSA Technical Digest (Optical Society of America, 2019)*, paper cj_12_6.

[54] S. Wang, Y. Wang, N. K. Thipparapu, M. Ibsen, D.J. Richardson, and J. K. Sahu, "All-fiber wavelength-tunable Bi-doped laser employing a fiber Bragg grating operating in the 1300nm band," *Conference on Lasers and Electro-Optics Europe (CLEO), OSA Technical Digest (Optical Society of America, 2020)*, paper STh1P.7.

[55] S. Wang, N. K. Thipparapu, Y. Wang, M. Ibsen, D.J. Richardson, and J. K. Sahu, "Widely-tunable Bismuth-doped fiber laser for the 1305-1375nm wavelength range," *OSA Advanced Photonic Congress, Specialty Optical Fibers*, 2020, paper SoM4H.6.

[56] S. Wang, Y. Wang, N. K. Thipparapu, M. Ibsen, D. J. Richardson, and J. K. Sahu, "Tunable CW Bi-doped fiber laser system from 1320 to 1370 nm using a ber Bragg grating," *IEEE Photonics Technology Letters*, **32**(22), 1443-1446 (2020).

[57] E.M. Dianov, A.A. Krylov, V.V. Dvoyrin, V.M. Mashinsky, P.G. Kryukov, O.G. Okhotnikov, and M. Guina, "Mode-locked Bi-doped fiber laser." *JOSA B*, **24**(8), 1807-1808 (2007).

[58] S. Kivisto, R. Gumenyuk, J. Puustinen, M. Guina, E. M. Dianov, and O. G. Okhotnikov, "Mode-locked Bi-doped all-fiber laser with chirped fiber Bragg grating," *IEEE Photonics Technology Letters*, **21**(9) 599-601 (2009).

[59] A. A. Krylov, P. G. Kryukov, E. M. Dianov, O. G. Okhotnikov, and M. Guina, "Pulsed bismuth fibre laser with the intracavity-compensated group velocity dispersion," *Quantum Electronics*, **39**(1) (2009).

[60] A. A. Krylov, P. G. Kryukov, E. M. Dianov, and O. G. Okhotnikov, "Picosecond pulse generation in a passively mode-locked Bi-doped fibre laser," *Quantum Electronics*, **39**(10) 882 (2009).

[61] E. Kelleher, J. Travers, Z. Sun, A. Ferrari, K. Golant, S. Popov, and J. Taylor, "Bismuth fiber integrated laser mode-locked by carbon nanotubes," *Laser Physics Letters*, **7**(11), 790 (2010).

[62] B. H. Chapman, E. J. Kelleher, S. V. Popov, K. M. Golant, J. Puustinen, O. Okhotnikov, and J. R. Taylor, "Picosecond bismuth-doped fiber MOPFA for frequency conversion," *Optics letters*, **36**(19), 3792-3794 (2011).

[63] R. Gumenyuk, J. Puustinen, A. V. Shubin, I. A. Bufetov, E. M. Dianov, and O. G. Okhotnikov, "1.32 m mode-locked bismuth-doped fiber laser operating in anomalous and normal dispersion regimes," *Optics letters*, **38**(20), 4005-4007 (2013).

[64] A. Khegai, M. Melkumov, K. Riumkin, V. Khopin, F. Afanasiev, D. Myasnikov, and E. Dianov, "Figure-of-eight bismuth doped fiber laser operating at 1.3 microns in dissipative soliton regime," *Fiber Lasers XIV: Technology and Systems*, 10083, 43-50, SPIE, 2017.

[65] A. Khegai, M. Melkumov, S. Firstov, K. Riumkin, Y. Gladush, S. Alyshev, A. Lobanov, V. Khopin, F. Afanasiev, A. G. Nasibulin, et al., "Bismuth-doped fiber laser at 1.32 m mode-locked by single-walled carbon nanotubes," *Optics Express*, **26**(18), 23911-23917 (2018).

[66] N. K. Thipparapu, C. Guo, A. Umnikov, P. Barua, A. Taranta, and J. Sahu, "Bismuth-doped all-fiber mode-locked laser operating at 1340 nm," *Optics Letters*, **42**(24), 5102-5105, (2017).

[67] T. Noronen, M. Melkumov, D. Stolyarov, V. F. Khopin, E. Dianov, and O. G. Okhotnikov, "All-bismuth fiber system for femtosecond pulse generation, compression, and energy scaling," *Optics letters*, **40**(10), 2217-2220 (2015).

[68] M. Jung, M. Melkumov, V. Khopin, E. Dianov, J. Kim, and J. Lee, "Self-Qswitching of a bismuth-doped germanosilicate fiber laser operating at 1.46 m," *Laser Physics Letters*, **10**(12), 125104 (2013).

[69] M. Jung, J. Lee, M. Melkumov, V. Khopin, E. Dianov, and J. Lee, "Burst-mode pulse generation from a bismuth-doped germanosilicate fiber laser through self Q-switched mode-locking," *Laser Physics Letters*, **11**(12), 125102 (2014).

[70] R. Gumenyuk, M. Melkumov, V. Khopin, E. Dianov, and O. Okhotnikov, "Effect of absorption recovery in bismuth-doped silica glass at 1450 nm on soliton grouping in fiber laser," *Scientific reports*, **4**(1), 1-5 (2014).

[71] J. Rissanen, D. A. Korobko, I. O. Zolotovsky, M. Melkumov, V. F. Khopin, and R. Gumenyuk, "Infiltrated bunch of solitons in Bi-doped frequency-shifted feedback fibre laser operated at 1450 nm," *Scientific reports*, **7**(1), 1-10 (2017).

[72] T. Noronen, S. Firstov, E. Dianov, and O. G. Okhotnikov, "1700 nm dispersion managed mode-locked bismuth fiber laser," *Scientific reports*, **6**(1), 1-6 (2016).

[73] A. Khegai, M. Melkumov, K. Riumkin, V. Khopin, S. Firstov, and E. Dianov, "Nalm-based bismuth-doped fiber laser at 1.7 μm," *Optics Letters*, **43**(5), 1127-1130 (2018).

[74] S. Kivisto, J. Puustinen, M. Guina, O. Okhotnikov, and E. Dianov, "Tunable modelocked bismuth-doped soliton fibre laser," *Electronics letters*, **44**(25), 1456-1458 (2008).

[75] A. Luo, Z. Luo, W. Xu, V. Dvoyrin, V. Mashinsky, and E. Dianov, "Tunable and switchable dual-wavelength passively mode-locked Bi-doped all-fiber ring laser based on nonlinear polarization rotation," *Laser Physics Letters*, **8**(8), 601 (2011).

[76] N. Thipparapu, S. Alam, Y. Wang, P. Shankar, D. J. Richardson, and J. K. Sahu, "Widely tunable actively mode-locked Bi-doped fiber laser operating in the Oband," *IEEE Photonics Technology Letters*, **34**(13), 711-714 (2022).

[77] B. H. Chapman, E. Kelleher, K. M. Golant, S. Popov, and J. Taylor, "Amplification of picosecond pulses and gigahertz signals in bismuth-doped fiber amplifiers," *Optics letters*, **36**(8), 1446-1448 (2011).

[78] N. K. Thipparapu, S. Jain, A. A. Umnikov, P. Barua, and J. K. Sahu, "1120nm diode-pumped Bi-doped fiber amplifier," *IEEE Journal of Selected Topics in Quantum Electronics*, **40**(10), 2441-2444 (2015).

[79] N. K. Thipparapu, A. A. Umnikov, P. Barua, and J. K. Sahu, "Bi-doped fiber amplifier with a flat gain of 25 dB operating in the wavelength band 1320–1360 nm," *Optics letters*, **41**, 1518-1521 (2016)

[80] N. K. Thipparapu, Y. Wang, A. A. Umnikov, P. Barua, D. J. Richardson, and J. K. Sahu, "High gain Bi-doped all fiber amplifier for O-band DWDM optical fiber communication," in *OFC* 2019, OSA, paper M1J.5.

[81] N. K. Thipparapu, Y. Wang, A. A. Umnikov, P. Barua, D. J. Richardson, and J. K. Sahu, "40 dB gain all fiber bismuth-doped amplifier operating in the Oband," *Optics Letters*, **44**(9), 2248-2251 (2019).

[82] Y. Wang, N. K. Thipparapu, S. Wang, P. Barua, D. J. Richardson, and J. K. Sahu, "Study on the temperature dependent characteristics of O-band bismuth-doped fiber amplifier," *Optics letters*, **44**, 5650-5653 (2019)

[83] A. Khegai, Y. Ososkov, S. Firstov, K. Riumkin, S. Alyshev, A. Kharakhordin, E. Firstova, F. Afanasiev, V. Khopin, A. Guryanov, and M. Melkumov, "O-band bismuth-doped fiber amplifier with 67 nm bandwidth," in *OFC* 2020, OSA, paper W1C.4.

[84] V. Mikhailov, M. A. Melkumov, D. Inniss, A. M. Khegai, K. E. Riumkin, S. V. Firstov, F. V. Afanasiev, M. F. Yan, Y. Sun, J. Luo, G. S. Puc, S. D. Shenk, R. S. Windeler, P. S. Westbrook, R. L. Lingle, E. M. Dianov, and D. J. DiGiovanni, "Simple Broadband Bismuth Doped Fiber Amplifier (BDFA) to Extend O-band Transmission Reach and Capacity," in *OFC* 2019, OSA, paper M1J.4.

[85] V. Mikhailov, J. Luo, M. Yan, G. S. Puc, Y. Sun, S. D. Shenk, D. Yuriy, R. S. Windeler, P. S. Westbrook, D. Inniss, and D. J. DiGiovanni, "Bismuth-doped fiber amplifiers (BDFA) to extend O-band transmission reach and capacity (Conference Presentation)," in *Next-Generation Optical Communication: Components, Sub-Systems, and Systems IX*, vol. 11309, International Society for Optics and Photonics, SPIE, 2020.

[86] E. Firstova, A. Kharakhordin, S. Alyshev, A. Khegai, M. Melkumov, and S. Firstov, "Depressed-Cladding Bi-doped P2O5 – SiO2 Fiber For Efficient Optical Devices Operating Near 1.3 μm," in *OSA Advanced Photonics Congress (AP)* 2020, paper SoM4H.3.

[87] S.V. Firstov, A.M. Khegai, A.V. Kharakhordin, S.V. Alyshev, E.G. Firstova, Y.J. Ososkov, M.A. Melkumov, L.D. Iskhakova, E.B. Evlampieva, A.S. Lobanov, and M.V. Yashkov, "Compact and efficient O-band bismuth-doped phosphosilicate fiber amplifier for fiber-optic communications." *Scientific Reports*, **10**(1), 11347 (2020).

[88] M. A. Melkumov, I. A. Bufetov, A. V. Shubin, S. V. Firstov, V. F. Khopin, A. N. Guryanov, and E. M. Dianov, "Bismuth-Doped Optical Fiber Amplifier for 1430 nm Band Pumped by 1310 nm Laser Diode," in *Optical Fiber Communication Conference/National Fiber Optic Engineers Conference* 2011, OSA, paper OMH1.

[89] M. A. Melkumov, I. A. Bufetov, A. V. Shubin, S. V. Firstov, V. F. Khopin, A. N. Guryanov, and E. M. Dianov, "Laser diode pumped bismuth-doped optical fiber amplifier for 1430 nm band," *Optics letters*, **36**, 2408-2410 (2011)

[90] A. M. Khegai, Y. Z. Ososkov, S. V. Firstov, K. E. Riumkin, S. V. Alyshev, V. F. Khopin, F. V. Afanasiev, A. S. Lobanov, A. N. Guryanov, O. I. Medvedkov, and M. A. Melkumov,

"Wideband 26 dB bismuth-doped fiber amplifier in the range 1.3-1.44 μm," *2020 International Conference Laser Optics (ICLO)*, St. Petersburg, Russia, 2020, pp. 1-1

[91] A. Khegai, Y. Ososkov, S. Firstov, K. Riumkin, S. Alyshev, A. Kharakhordin, V. Khopin, F. Afanasiev, A. Guryanov, and M. Melkumov, "Gain Clamped Bi-Doped Fiber Amplifier With 150 nm Bandwidth for O- and E-Bands," *Journal of Lightwave Technology*, **40**, 1161-1166 (2022)

[92] Y. Wang, N. K. Thipparapu, D. J. Richardson, and J. K. Sahu, "Ultra-Broadband Bismuth-Doped Fiber Amplifier Covering a 115-nm Bandwidth in the O and E Bands," *Journal of Lightwave Technology*, **39**, 795-800 (2021)

[93] Y. Wang, N. K. Thipparapu, D. J. Richardson, and J. K. Sahu, "High Gain Bi-Doped Fiber Amplifier Operating in the E-band with a 3-dB Bandwidth of 40nm," in *Optical Fiber Communication Conference (OFC)* 2021, OSA, paper Tu1E.1.

[94] Y. Ososkov, A. Khegai, S. Firstov, K. Riumkin, S. Alyshev, A. Kharakhordin, A. Guryanov, A. Lobanov, and M. Melkumov, "Low-Water-Peak Bismuth-Doped Fiber for Efficient O+E Band Amplifiers," in *Laser Congress 2021 (ASSL,LAC)*, (Optica Publishing Group, 2021), paper AW1A.3.

[95] A. Khegai, Y. Ososkov, S. Firstov, K. Riumkin, S. Alyshev, A. Kharakhordin, A. Lobanov, A. Guryanov, and M. Melkumov, "O+E Band BDFA with Flattop 116 nm Gain Bandwidth Pumped with 250 mW at 1256 nm," in *Optical Fiber Communication Conference (OFC)* 2021, OSA, paper Tu1E.4.

[96] Y. Ososkov, A. Khegai, S. Firstov, K. Riumkin, S. Alyshev, A. Kharakhordin, A. Lobanov, A. Guryanov, and M. Melkumov, "Pump-efficient flattop O+E-bands bismuth-doped fiber amplifier with 116 nm 3 dB gain bandwidth," *Optics Express*, **29**(26) 44138-44145, 2021.

[97] V. V. Dvoyrin, V. M. Mashinsky, and S. K. Turitsyn, "Bismuth-Doped Fiber Amplifier Operating in the Spectrally Adjacent to EDFA Range of 1425-1500 nm," in Optical Fiber Communication Conference (OFC) 2020, OSA, paper W1C.5.

[98] A. Donodin, V. Dvoyrin, E. Manuylovich, L. Krzczanowicz, W. Forysiak, M. Melkumov, V. Mashinsky, and S. Turitsyn, "Bismuth doped fibre amplifier operating in E- and S-optical bands," *Optical Materials Express*, **11**(1), 127-135 (2021).

[99]S. V. Firstov, S. V. Alyshev, K. E. Riumkin, V. F. Khopin, A. N. Guryanov, M. A. Melkumov, and E. M. Dianov, “A 23-dB bismuth-doped optical fiber amplifier for a 1700-nm band,” *Scientific Reports*, 6(28939), 1-6, (2016).

[100] S. V. Firstov, S. V. Alyshev, K. E. Riumkin, A. M. Khegai, A. V. Kharakhordin, M. A. Melkumov, and E. M. Dianov, “Laser-active fibers doped with bismuth for a wavelength region of 1.6-1.8μm,” *IEEE Journal of Selected Topics in Quantum Electronics*, 24(5), 1-15, (2018).

[101] G. Gomolka, M. Krajewska, M. Kaleta, A. M. Khegai, S. V. Alyshev, A. S. Lobanov, S. V. Firstov, and M. Nikodem, “Operation of a single-frequency bismuth-doped fiber power amplifier near 1.65μm," *Photonics*, 7, 128, MDPI, (2020)

Chapter 3 Introduction to optical fibre fabrication

3.1 Introduction

The purpose of this section is to present a comprehensive introduction to the silica fibre fabrication process, which was utilised in the preparation of all the Bi-doped fibres (BDFs) in this project. The fibre fabrication typically consists of two essential stages, namely preform fabrication and fibre drawing. Additional glass working processes, such as sleeving and jacketing, may also be incorporated between these stages, depending on the intended geometry of the final product. In Section 3.2, the modified chemical vapour deposition (MCDV), combined with solution doping technique for preform fabrication is elaborated in detail. Subsequently, the preform processing and analysis are presented in Section 3.3. Section 3.4 outlines the fibre drawing process. Finally, a conclusion is provided in Section 3.5.

3.2 Fabrication of the preform

A fibre preform is typically a cylindrical rod of optical glass with a cladding layer and a core layer. Various chemical elements are doped into the two layers to create the desired fibre refractive index profile. The preforms fabricated in this work are typically around 40 cm with a diameter of approximately 10 mm, although it can be longer and larger diameter in particular for telecom preforms. The preform is subsequently processed in a fibre drawing tower, where it is drawn into optical fibres with much smaller diameters, typically around 125 µm.

Several deposition methods are available for fabricating a standard preform. The four primary techniques include MCVD [1], Outside Vapour Deposition (OVD) [2,3], Vapour Axial Deposition (VAD) [4] and Plasma-activated Chemical Vapour Deposition (PCVD) [5]. Recently, a unique method for preform fabrication using 3D printing has been developed and studied for different glass hosts and fibre geometry structures [6,7]. In situations where the vapour deposition cannot be applied due to the absence of suitable raw precursors, the rod-in-tube technique may be used as an alternative [8]. Additionally, for specialty fibres such as multi-core fibres, photonic crystal fibres, and hollow-core fibres, preforms are fabricated using the stacking-and-draw technique [9,10].

Among the four vapour deposition techniques, MCVD is widely used in both industry and research for specialty fibres for its ability to provide low background loss and also for the control of dopants to achieve the desired refractive index profile in fibres. This method was developed in the 1970s, with pioneering contributions from the Bell Telephone Laboratories (Bell Labs) Corning and NTT (Nippon Telegraph and Telephone Corporation). The process was later improved for Res doped fibre fabrication by combining a solution-doping technique by the Optoelectronics Research Centre (ORC) in University of Southampton (UK) [1]. In the MCVD process, the dopant chemical is introduced in vapour form inside a horizontal glass tube, whereas in OVD process, the deposition occurs outside a target rod which is subsequently removed. When it comes to VAD, the deposition occurs at the end of a target rod, and the preform grows in an axial direction. In addition, it requires an extra drying process as a huge amount of moisture is involved when the reaction happens. This technique can produce preforms with a very long length. In PCVD, the reaction happens with the help of microwave-induced plasmas instead of a traditional burner, resulting in precise deposition control of dopant/refractive index profile.

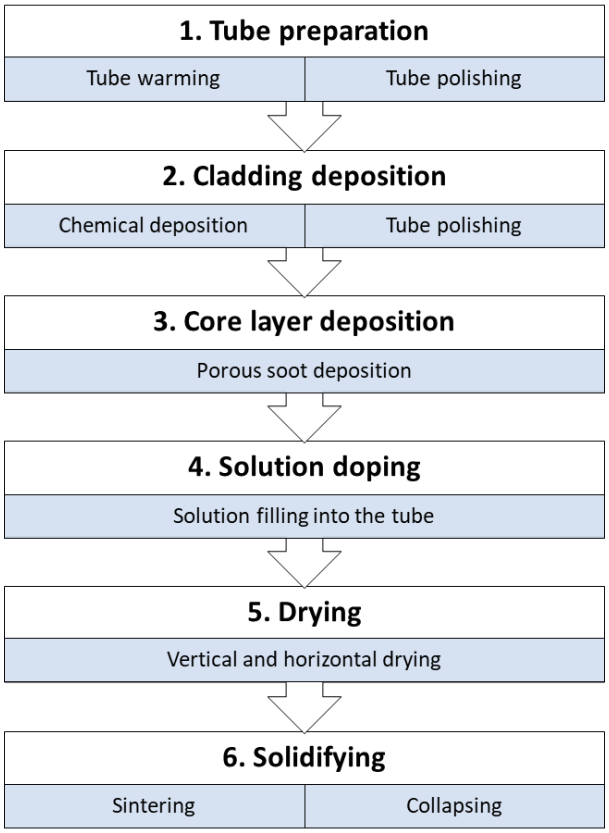

Figure 3.1 Procedure of standard MCVD-solution doping technique

MCVD combined with solution doping is a mature technique to fabricate rare-earth (RE)-doped fibres and has been applied to make Bi-doped preforms in this study. The flow chat of the MCVD-solution doping process is shown in Figure 3.1, which consists of six main steps. The preform fabrication process begins with the warmup pass during which the substrate tube is heated to a temperature of approximately 1800 °C. Next, the substrate tube undergoes a gas-phase etching with SF6 to remove any existing impurities, and subsequently flame polished to smooth out the inner surface. The next two steps involve the deposition of cladding layers and porous soot layer inside the tube. The chemical vapor used in these steps depends on the refractive index profile and the fibre design. After the tube is separated from the lathe, the process moves to solution doping. Solution containing RE ions or Bi ions, in this case, is incorporated into the inner surface of the tube. A detailed explanation of the deposition and solution doping processes will be given later. Next, the tube is dried and returned to the MCVD lathe, where it is sintering into a transparent core layer and eventually the tube is collapsed into a solid rod at high temperatures at around 2000 °C (heated by the burner on the lather), driven by the surface tension effect of the glass on the inner wall.

Figure 3.2 shows the schematic diagram of an MCVD system. The system employs a bubbler system to generate chemical vapour, which is delivered to the tube through a rotary seal. The tube is heated by a burner that moves along the MCVD lathe, facilitating the chemical reaction. An extract line is installed at the end of the tube to collect wasted gas. Cameras are positioned at the top of the lathe to monitor the temperature and diameter of the tube during the fabrication. The MCVD process is primarily computer-controlled, but manual operation can be employed when necessary.

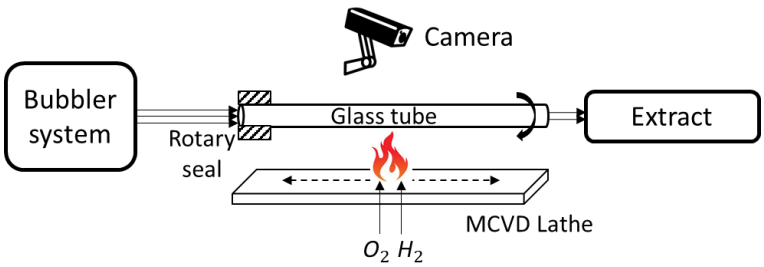

Figure 3.2 Schematic diagram of the MCVD system structure

A schematic diagram of a bubbler system is shown in Figure 3.3. The MCVD process involves vaporising halide precursors such as $SiCl_4$, $GeCl_4$ or $POCl_3$ and delivering them via a carrier gas, usually oxygen (O_2), through a bubbler system containing the liquid precursor. The

states of $SiCl_4$, $GeCl_4$ or $POCl_3$ shown in the chemistry equations (3-1, 3-2 and 3-3) below are in gas form.

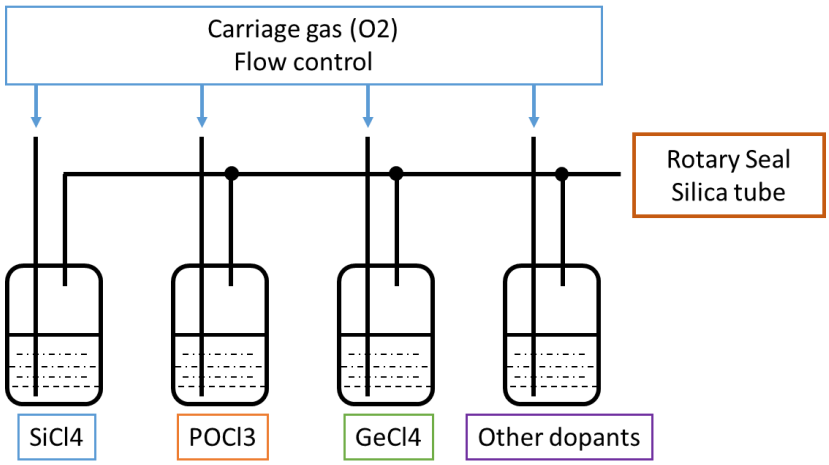

Figure 3.3 Diagram of bubbler system of the MCVD process

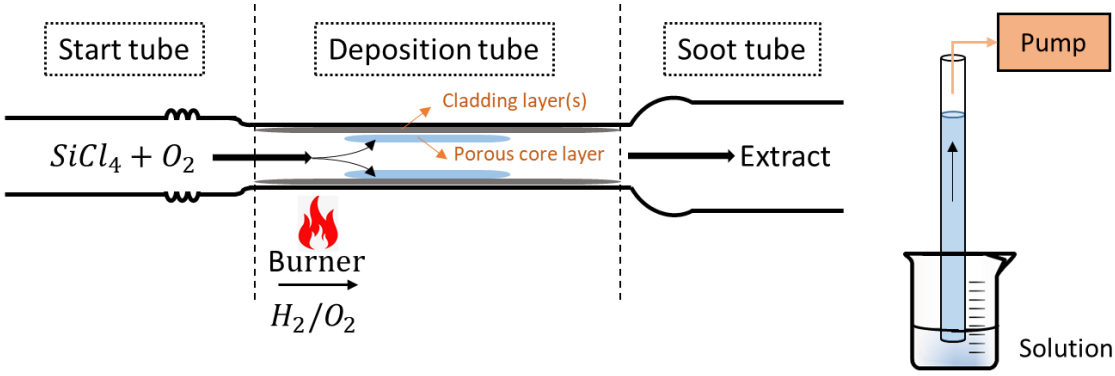

(A) (B)

Figure 3.4 Principal diagram of the MCVD process. (A): Configuration of the tube on the MCVD lathe, including a start tube, a deposition tube, and a soot tube with typical outer/inner diameters of 20/16, 16/13 and 36/31 mm, respectively. The reaction takes place inside the tube, with a burner move forwards and backwards. B: A simplified diagram of the solution doping step, where the tube is placed vertically and connected to a pump for maintaining the liquid level.

Figure 3.4 (a) displays the configuration of the tube assembly on the lathe and the deposition process occurring inside the tube. The process first involves joining a CFQ (clear fused quartz) start tube, an F300 deposition tube (made of Heraeus F300® material with high purity, commonly used for standard fibre fabrication) and a CFQ soot tube on the

MCVD lathe. The typical outer/inner diameters of the three tubes used for BDFs fabrication are 20/16, 16/13 and 36/31 mm, respectively. In most cases, the deposition tube for REs doped fibres fabrication has the outer/inner diameter of 20/16 mm, but a smaller tube is preferred in this study because less collapse pass would be required after the solution doping, which can reduce the evaporation of the Bi ions. The F300 tube is gas phase etched by passing through O_2 and SF_6 at a high temperature followed by the flame polishing at ~2000 °C. Depending on the preform design, several silica inner cladding layers are deposited and sintered at a temperature ~2000°C, based on the chemical equation:

$$SiCl_4(g) + O_2(g) = SiO_2(s) + 2Cl_2(g) \quad 3\text{-}1$$

The chemical reaction happens at the hot zone and forms glassy particles that deposit at the cooler zone (downstream) of the tube and subsequently sintered into a transparent glassy layer as the burner passes over. (Note that Figure 3.4(a) shows a forward-moving burner as an example, but it can move in both directions.) This process follows the principle known as thermophoresis [21], which suggests that particles suspend in a gas with a temperature gradient tends to move towards the direction of decreasing temperature. Therefore, SiO_2 particles move with the gas flow and adhere to the inner wall of the substrate tube. Obviously, when the burner moves in the forward direction, the deposition occurs ahead of the burner, while when the burner moves in the reverse direction, the deposition occurs behind of it.

After deposition of the cladding layers, the temperature is lowered to ~1400-1600°C for the deposition of the soot. A porous core layer with white colour is formed in this step, which will form as the preform core at the end of the whole fabrication. The core can be deposited with a pure silica, or combined with other dopants such as Ge and P. The balanced oxidation reactions involved in the deposition process are shown in equation 3-2 and 3-3.

$$GeCl_4(g) + O_2(g) = GeO_2(s) + 2Cl_2(g) \quad 3\text{-}2$$

$$4POCl_3(g) + 5O_2(g) = 2P_2O_5(s) + 6Cl_2(g) \quad 3\text{-}3$$

The optimal soot deposition temperature depends on the glass composition, and adjustments may be necessary to achieve the desired porosity. A higher soot deposition temperature may cause partial sintering of the soot body, in which the porosity of the soot is reduced, resulting in poor incorporation of the dopants from the solution. Conversely, if

the deposition temperature is too low, the soot layer may peel off from the inner surface of the tube during subsequent steps due to inadequate adhesion.

Another crucial step in the RE/Bi-doped preform fabrication process is solution doping [12]. Figure 3.4(b) presents a simplified diagram of the solution doping procedure. After the soot deposition stage is completed, the tube is removed from the lathe and soaked in a solution for approximately one hour. Subsequently, the tube is slowly drained and dried both vertically and horizontally. The horizontal drying is performed by placing the tube back into the MCVD lathe with a slow rotation speed and allowing nitrogen/oxygen/helium (N2/O2/He) gas to flow through it. Once the tube is thoroughly dried, it is joined with another soot tube with an outer/inner diameter of 20/16 mm. An oxidation/sintering pass is then applied with a certain amount of O_2 flowing through the tube, to oxidize the incorporated ions from the solution and to transform the porous soot layer into a clear and transparent glass. Lastly, the deposition tube is collapsed to a solid preform that requires several passes of the burner at high temperatures exceeding 2000 °C.

3.3 Preform processing

After the MCVD-solution doping process, the preform undergoes analysis using a commercial preform refractive index profiler (Photon Kinetics PK2600). The preform is fixed vertically and partially immersed in a cell containing a specific oil with a slightly higher index than pure silica. A laser at a specific wavelength (633 nm in this study) spans around a specific position of the preform and some of the incident light will be reflected. Based on the angle of the reflected light, the index of the core and the cladding is measured. The preform is rotated and moved longitudinally to measure the profile at different angles and positions.

Figure 3.5 and Figure 3.6 depict the refrative index profiles of a Bi-doped phosphosilicate preform (L10619) and a Bi-doped aluminosilicate preform (L10730), respectively. The position of measurement on the preform cross section is shown on the x-axis while the y-axis displays the refractive index of the core at each point. The Z value indicate the position of this sampled cross section along the entire preform, for instance Z=180mm means the measurement was take at a position of 180mm from the preform tip. The angle between two consecutive measurements is 90 degrees, which is denoted by W=0/90. The circularity

of the core can be assessed by the consistency of the refractive index measurements at different angles. By comparing the profiles measured at different positions (Z values), the uniformity of the preform can be estimated, which is a critical parameter determining the section for subsequent fibre drawing and other investigations.

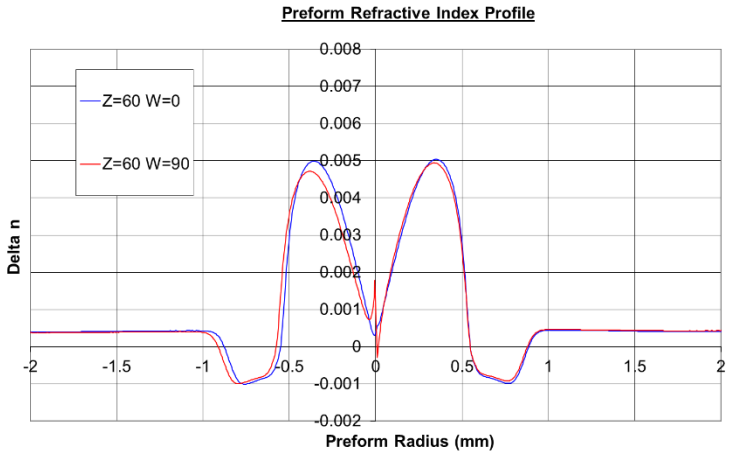

Figure 3.5 Refractive index profile of the Bi-doped phosphosilicate preform (L10619)

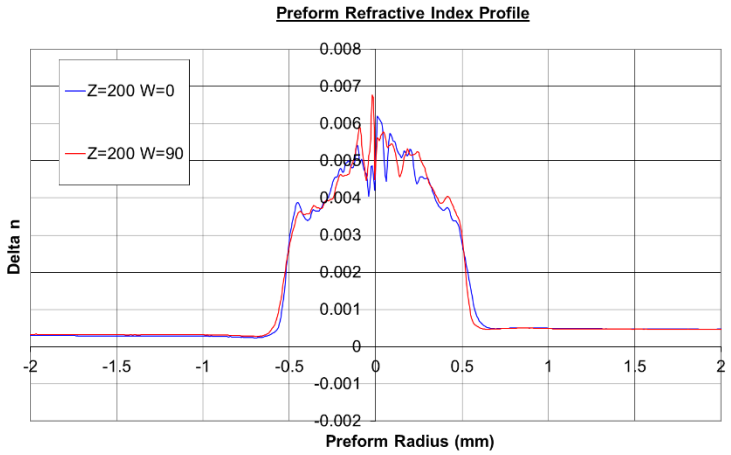

Figure 3.6 Refractive index profile of the Bi-doped aluminosilicate preform (L10730)

The L10619 profile (Figure 3.5) exhibits a central index depression, which is caused by the high volatility of phosphorous during high-temparature treatment, such as sintering and collapsing passes, at a temperature above 2000°C. Conversely, this phenomenon does not happen in case of aluminosilicate preform, L10730 (figure 2.3) because the chemical bond between aluminium and oxygen is stronger than that between phosphorus and oxygen, making aluminium oxide more difficult to decompose and evaporate under high temperatures. In most cases this central depression would impact the overlap of the light

and the doped area, depending on the transmission mode. For instance, the fundamental mode of light propagating within the fibre would exhibit a peak at the core's center where the refractive index undergoes a significant reduction.

Based on the obtained refractive index profile, the concentration of P_2O_5 and Al_2O_3 can be estimated using equations 3-4 and 3-5 [13,14]:

$$\Delta n \approx (0.88 \times 10^{-3}) \times C_{P2O5}(mol\%) \quad 3\text{-}4$$

$$\Delta n \approx (2.44 \times 10^{-3}) \times C_{Al2O3}(mol\%) \quad 3\text{-}5$$

Here, Δn is the refractive index difference between the core and cladding shown in the measured profiles, C_{P2O5} and C_{Al2O3} are the concentration of the corresponding oxides in mol% unit.

3.4 Fibre drawing

The final step in the manufacturing of optical fibres is the drawing of the preform on a fibre drawing tower. This process can be divided into several stages, as depicted in Figure 3.7(a): Preparation, glass pulling, coating, diameter adjustment, cross-section checking, and fibre collection. The individual stages involve various procedures such as furnace purging and positioning the preform inside the furnace, preform heating, formation of preform neck-down once the draw temperature is reached and drop-down of the preform, preform feeding, fibre drawing speed adjustment, coating and UV curing of fibre, and concentricity checking before collection. Figure 3.7(b) shows a schematic of the drawing tower which consists of a preform chuk on the top for holding the preform, a furnace, a first diameter gauge to measure the diameter of the bare fibre, a cane puller used to start the fibre drawing process, a coating applicator containing liquid coating material, a ultraviolet (UV) light to cure the coating liquid to a solid state, a second diameter gause to measure the coated fibre diameter, a rotating capstan and a spool for the fibre collection.

The optical fibre drawing process starts with the preparation of the preform and furnace. The preform is mounted vertically on the top of the furnace, with its x-y position aligned to the furnace's central point. Before loading the preform, the graphite furnace which is widely used for the fibre drawing is purged with an inert gas (Argon, Ar) to prevent any reaction of the graphite at high temperature with oxygen. The preform is then loaded into

the hot zone and heated to a temperature above the glass softening point, which is approximately 2000°C. At this point, a necked-down region is formed, and the tip of the preform falls down due to the force of gravity. The drop is then cut, and the tapered region is fed into a cane puller that applies drawing force on the glass. As a result, the bare fibre diameter monitored by the first diameter gauge will see a preliminary decrease with continuously pulling.

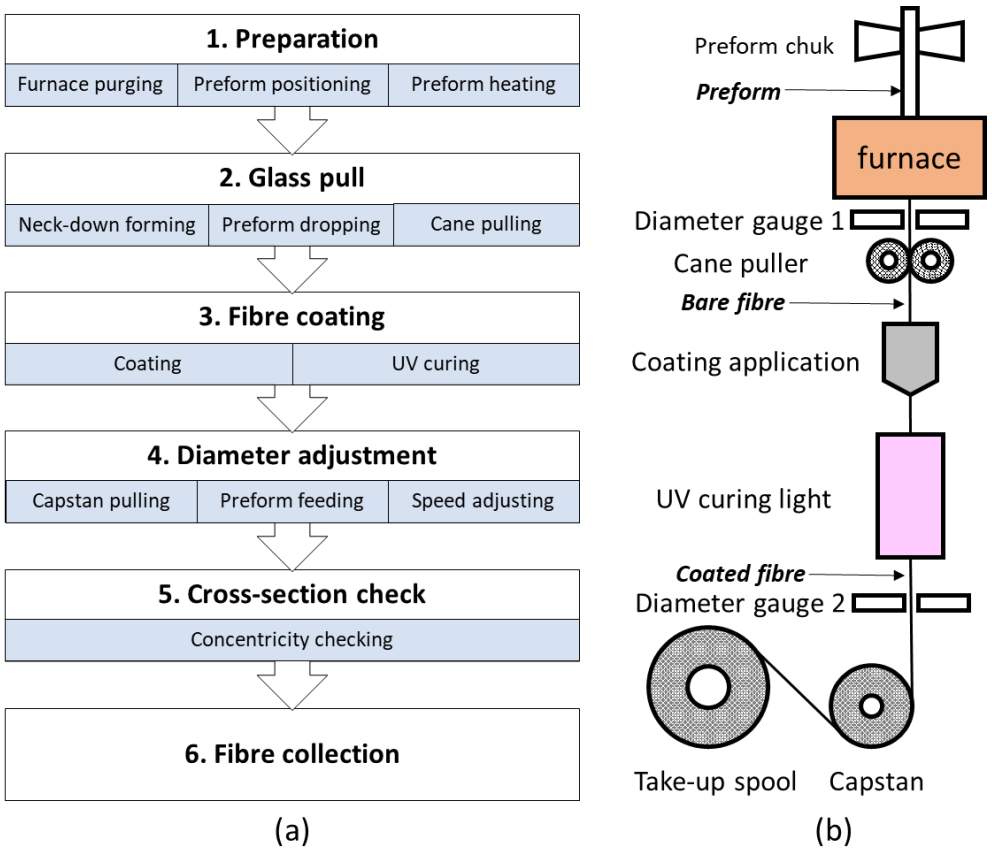

Figure 3.7 (a) Procedure of standard fibre drawing; (b) Schematic of a fibre drawing tower.

Once the fibre diameter has decreased to a suitable value, the coating step begins. The bare fibre is placed into a coating cup containing liquid polymer coating material, and a UV light is used to cure the liquid. The coated fibre is then wound onto a bottom capstan, while the cane puller must be realised at this time. The fibre should be only pulled by cane puller or the capstan. A second diameter gauge is installed below the UV light to monitor the coated fibre diameter. The preform starts moving down into the furnace at a feeding speed, balancing with the capstan pulling speed to obtain the fibre diameter to the target value. Once the target diameter is reached and maintained stably, a short piece of fibre is cut as

a sample for checking the concentricity of fibre and coating under optical microscope. Eventually, the fibre is wrapped onto a take-up drum for collection.

As previously mentioned, the diameter of the optical fibre is adjusted by balancing the preform feeding speed and the fibre drawing speed provided by the capstan. According to the principle of conservation of volume, these two speeds are related by the following equation:

$$V_p \cdot {D_p}^2 = V_f \cdot {D_f}^2 \qquad 3\text{-}6$$

Here, V_p, V_f, D_p, D_f, refer to the preform feeding speed, the fibre drawing speed, the diameter of the preform, and the diameter of the fibre, respectively.

Fibre drawing temperature and speed play crucial roles in the fibre fabrication and are investigated by many researchers [15, 16]. Firstly, a higher drawing temperature can reduce the viscosity of the glass and make the fibre easier to draw. Conversely, a lower drawing temperature can increase the viscosity and lead to a more stable fibre, but it may also require a higher drawing force and increase the risk of breakage. On top of that, the fibre drawing is affected by the temperature distribution at the hot zone inside the furnace. In addition, the fibre to be cooled before the coating can be applied and is affected by the drawing speed. For the high-speed fibre drawing, the natural cooling of fibre is not sufficient to bring the fibre temperature lower to a level as required for applying the coating and as such forced cooling is used. The drawing temperature and the drawing speed give a combined effect on the tension being exerted upon the optical fibre, which also influence the ultimate performance characteristics of the resulting fibre [17]. Other parameters such as the cleanliness of the furnace, the preform quality, and the coating process quality can also impact the drawing process and the final product [18].

In our study, the drawing speed typically ranged from 10~40 m/min, with most samples being drawn at a speed of 10 m/min. The drawing temperature is 2000 °C. The typical diameter of a bare fibre is around 125μm, although this value may vary depending on the fibre design. In this study, diameters of BDFs are within the range of 100~125 μm. The coating material is DSM-314 with high refractive index.

3.5 Conclusion

This chapter introduces a complete process of optical fibre manufacturing, from preform fabrication, analysis, to the fibre drawing. The MCVD-solution doping technique is used widely for RE-doped active fibres. The development of Bi-doped fibres in this work is also based on this fabrication procedure.

3.6 Reference

[1] S. R. Nagel, J. B. MacChesney and K. L. Walker, "An Overview of the Modified Chemical Vapor Deposition (MCVD) Process and Performance," in *IEEE Transactions on Microwave Theory and Techniques*, **30**(4), 305-322(1982).

[2] P. C. Schultz, "Fabrication of optical waveguides by the outside vapor deposition process," *Proceedings of the IEEE*, **68**(10), 1187-1190 (1980).

[3] M. Blankenship, and C. Deneka, "The outside vapor deposition method of fabricating optical waveguide fibers." *IEEE journal of Quantum Electronics*, **18**(10), 1418-1423 (1982).

[4] S. Sudo, , M. Kawachi, , T. Edahiro, , T. Izawa, , T. Shioda, and H. Gotoh, "Low-OH-content optical fibre fabricated by vapour-phase axial-deposition method." *Electronics Letters*, **17**(14), 534-535 (1978).

[5] H. Lydtin, "PCVD: A technique suitable for large-scale fabrication of optical fibers," *Journal of Lightwave Technology*, **4**(8), 1034-1038 (1986).

[6] K. Cook, J. Canning, S. Leon-Saval, Z. Reid, M.A. Hossain, J.E. Comatti, Y. Luo, and G.D. Peng, "Air-structured optical fiber drawn from a 3D-printed preform." *Optics letters*, **40**(17), 3966-3969 (2015).

[7] A. L. C. Rosales, M. M. N. Velázquez, X. Zhao, and J.K. Sahu, "Optical fibers fabricated from 3D printed silica preforms". In *Laser 3D Manufacturing VII*, SPIE, **11271**, 93-99 (2020)

[8] X. Wang, Q. Nie, T. Xu, and L. Liu, "A review of the fabrication of optic fiber". *ICO20: Optical Design and Fabrication*, 6034, 346-354 International Society for Optics and Photonics. SPIE; (2006).

[9] L. Brilland, F. Smektala, G. Renversez, T.Chartier, J. Troles, T. N. Nguyen, N. Traynor, and A. Monteville, "Fabrication of complex structures of Holey Fibers in Chalcogenide glass," *Optics Express*, **14**, 1280-1285 (2006)

[10] I. Ishida, T. Akamatsu, Z. Wang, Y. Sasaki, K. Takenaga and S. Matsuo, "Possibility of stack and draw process as fabrication technology for multi-core fiber," *2013 Optical Fiber Communication Conference and Exposition and the National Fiber Optic Engineers Conference (OFC/NFOEC)*, 2013, 1-3

[11] K. L. Walker, F. T. Geyling and S. R. Nagel, "Thermophoretic deposition of small particles in the modified chemical vapor deposition (MCVD) process," *Journal of the American Ceramic Society* **63**(9-10), 552-558 (1980).

[12] J. E. Townsend, S. B. Poole, and D. N. Payne, "Solution-doping technique for fabrication of rare-earth-doped optical fibres," *Electronics letters* **23**(7) 329-331 (1987).

[13] L. Thevenaz, ed., Advanced fiber optics: concepts and technology. EPFL press. 2011.

[14] K. Oh, and U.C. Paek, Silica optical fiber technology for devices and components: design, fabrication, and international standards. John Wiley & Sons. 2012.

[15] A. Alessi, S. Girard, M. Cannas, S. Agnello, A. Boukenter, and Y. Ouerdane, "Influence of drawing conditions on the properties and radiation sensitivities of pure-silica-core optical fibers." *Journal of Lightwave Technology*, **30**(11), 1726-1732, (2012).

[16] G. Luzi, P. Epple, M. Scharrer, K. Fujimoto, C. Rauh, and A. Delgado, "Influence of surface tension and inner pressure on the process of fibre drawing." *Journal of Lightwave Technology*, **28**(13), 1882-1888 (2010).

[17] Y. Hibino, F. Hanawa, and M. Horiguchi, "Drawing-induced residual stress effects on optical characteristics in pure-silica-core single-mode fibers". *Journal of applied physics*, **65**(1), 30-34, (1989).

[18] L.L. Blyler, and F.V. DiMarcello, "Fiber drawing, coating, and jacketing." *Proceedings of the IEEE*, **68**(10), 1194-1198 (1980).

Chapter 4 Development of Bi-doped phosphosilicate fibres

4.1 Introduction

This chapter presents the fabrication and spectroscopic characterisation of Bi-doped phosphosilicate optical fibres (BPSFs), which are utilised for lasers and amplifiers developments in the wavelength range of 1300-1380 nm. Section 4.2 details the efforts made to produce efficient BPSFs by modifying different fabrication conditions, while Section 4.3 outlines the analyses and measurements carried out on these fibres. The glass composition has been analysed by secondary ion mass spectrometry (SIMS) or electron probe microanalysis (EPMA). In addition, the absorption and unsaturable loss, two critical factors used to evaluate the performance of BPSFs, have been measured and presented in detail. The results were used as feedback to optimise fabrication parameters. A reproducible fabrication process of BPSFs was established, which yielded fibre capable of providing a >25 dB gain in the amplifier [1], or a >170 mW output power and a >35% slope efficiency in the laser [2]. (Laser development will be presented in Chapter 5.) Section 4.4 provides a summary of the BPSF development.

4.2 Fabrication of the Bi-doped phosphosilicate fibres

A sequence of Bi-doped phosphosilicate preforms were fabricated in this study based on the MCVD-solution doping technique. A conventional procedure of this technique was introduced in Chapter 3, while this section outlines fabrication parameters and their modifications used in the development of BPSF specifically. F300 silica tubes with external and internal diameters of 16 and 13mm, respectively, were employed as deposition tubes throughout the entire study. The core of the Bi-doped phosphosilicate preforms contains Si, P and Bi ions. Among the three elements, Si was incorporated during the porous soot deposition stage, while both Bi and P ions were introduced through a solution containing both Bi and P precursors dissolved in ethanol (EtOH). The soot layer was deposited on the inner surface of the tube in the temperature range from 1300 to 1400 °C. The soot deposition temperature is correlated with the tube's cross-sectional area (CSA), which will be higher around 1400-1450 °C if a tube with a 20/16 mm (outer/inner) diameter is used. This is due to the larger CSA of such tubes than that of 16/13 mm diameter tubes used in this work, requiring a higher temperature to attain the appropriate temperature inside the

tube for the chemical reactions to occur. Afterward, the tube was removed from the MCVD lathe and subjected to solution doping, followed by drying, sintering, collapsing and sealing procedures as described in Section 3.2 and in Figure 3.1. For BPSF fabrications, there was no individual oxidation pass, as oxidation occurred simultaneously during the sintering pass.

In this study, the impact of varying the (1) soot deposition temperature and (2) solution concentration on the doped Bi concentration and corresponding fibre performance was investigated. Details of the BPSFs fabricated in this project are shown in Table 4.1 below. Except from these two parameters, other conditions remained same in the fabrication of all BPSFs. The fibre drawing speed was 10 m/min.

The soot deposition temperature is an important parameter in the fabrication of Bi-doped phosphosilicate preforms, as it affects the morphology and structure of the deposited layer. A lower deposition temperature can result in a more porous layer with a larger surface area, which can be beneficial for achieving a higher Bi concentration. However, this also increases the risk of soot peeling off from the substrate during subsequent processing steps. On the other hand, a higher deposition temperature can produce a more compact and stable layer, but it can also make it more difficult for the solution to penetrate and bond with the SiO_2 host, especially if the soot has already been pre-sintered [3].

In addition to the deposition temperature, the solution concentration is another important parameter that can impact the performance of the BPSFs. Increasing the concentration of the dopants in the solution can result in a stronger incorporation of Bi and P ions during the solution doping process thus a higher Bi concentration in the core of the fibre. However, using a highly concentrated solution also poses some challenges, such as increased viscosity and the risk of precipitation or agglomeration of the dopant ions [4]. Therefore, finding the optimal solution concentration is crucial for achieving high-quality BPSFs with desirable performance characteristics.

Table 4.1 List of fabricated BPSFs (Manual: manually H_2/O_2 flow control)

Dopants /Host	Preform No.	Fibre No.	Solution			T_{soot}(°C)	Draw speed (m/min)	D_{Core}/D_{Clad} (μm)	refractive index difference Δn
			$BiCl_3$ concentration (gm/100mL)	P_2O_5 concentration (gm/100mL)	Solvent				
Bi+P/Si	L10619	A1340	0.04	7.5	EtOH	1400±20*	10	12.5/125	0.004
	L10625	A1351				1360±20			0.003
	L10626	A1353				1340±25			0.004
	L10627	A1356				1320±25			0.005
	L10628	A1359				1300±25			0.005
	L10629	A1368				1340±10 (Manual)			0.005
	L10651	A1496				1350±5 (Manual)			0.005
	L10642	A1435	0.08	7.5		1340±10 (Manual)		10/100	0.005
	L10645	A1350	0.16	9.5		1340±10 (Manual)		10/100	0.006

*This preform was fabricated prior to a maintenance operation on the fabrication system. The soot temperature here should not be directly compared to those of other preforms, as the engineering work may have had an impact on the system's temperature and gas regulation.

From the table it can be found that, the change in soot temperature from 1360°C to 1300°C during the fabrication of preforms L10625 to L10628 led to an increase in refractive index difference (Δn) from 0.003 to 0.005. However, a further reduction in temperature resulted in a fragile soot layer and peel-off from the substrate tube causing difficulties for subsequent steps in the preform fabrication. Therefore, a temperature of 1340°C was chosen for subsequent Bi-doped preform fabrication (L10629, L10651, L10642 and L10645). It should be noted that the relatively high temperature fluctuation of 25 °C in preforms L10619~L10628 was due to the temperature auto-control mode of the system. The fluctuation came from the small diameter of the tube and slight mismatch of the camera monitoring the temperature in the central of the tube. The use of the manual control mode, which fixed the flow of H_2/O_2 at a certain value instead of adjusting it based on real-time temperature measurements, resulted in a much tighter temperature fluctuation of within 10 °C. This can be observed in preforms L10629 to L10645, which were fabricated under this mode.

Two preforms, L10642 and L10645, were fabricated with a higher concentration of Bi solution. Specifically, the concentration of Bi in the solution for the two preforms was double and four times respectively, than the concentration used in the majority of the preforms. To ensure full dissolution of $BiCl_3$, a higher P concentration in the solution was required for the fabrication of L10645, in order to balance the pH of the solution. The aim of fabricating these two preform was to study the impact of Bi concentration on the absorption and unsaturable loss of BPSFs.

After fabrication, the resulting BPSFs were subjected to a series of characterisation techniques, including chemical analysis to determine their composition, measurement of absorption in the near-infrared region, and assessment of unsaturable loss, which is described in the following section.

4.3 Characterisation of Bi-doped phosphosilicate fibres

In order to gain a better understanding of optical properties and performance characteristics of BPSFs, and to optimise the parameters for the construction of an efficient fibre fabrication process, it is necessary to analyse the glass composition, as well as to characterise their absorption spectrum and unsaturable loss. The spectroscopic

characterisation of BPSFs including fluorescence spectrum and lifetime measurements were carried out previously by another colleague [5] thus the full study about these parameters will not be discussed in detailed here. The lifetime of the BPSFs is in the range of 740-780 μs. The absorption cross-section (σ_a) and the emission cross-section (σ_e) are measured to be 2.7 and 1.8 pm^2 at 1295 and 1360 nm, respectively.

4.3.1 Glass composition of BPSFs

It has been observed that with an increase of the Bi concentration, the preform core tends to show a red-brown colour when viewed through the preform tip, whereas a yellow-pink colour is more likely to appear when the concentration is low. It should be noted that this colour can only be observed when looking along the axis of the rod and appears transparent when viewed along the radial direction. An example of the Bi-doped preform core is presented in Figure 4.1. This approach can provide a quick and simple assumption that whether Bi is doped in the preform successfully.

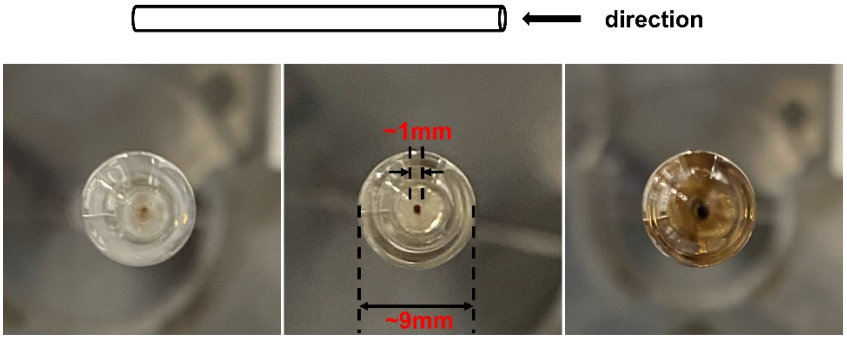

Figure 4.1 Pictures of some Bi-doped preforms' core. When the Bi doping concentration in the preform changes from low to high, the core appears yellow, pink, red, brown, and even black colour.

In addition, another quick indication of whether the Bi is doped in the preform is by relating it to the P concentration, assuming that the ratio of doped P ions and Bi ions remains the same as it in the solution. However, in reality, the Bi and P ions do not strictly adhere to this assumption; thus, this indication is merely used to establish a relative value among preforms of the same type.

Based on the fact that the refractive index difference (Δn) of BPSFs is only affected by P ions in the preform while Bi ions do not have any contribution, the concentration of P ions can be calculated from the Δn using the following equation:

$$C_{P2O5}(mol\%) \approx \Delta n/(0.88 \times 10^{-3}) \quad 4\text{-}1$$

where C is the concentration of P_2O_5 and 0.88×10^{-3} is the contribution to the refractive index of the preform per mol% of P_2O_5.

In case of preforms fabricated with the same solution, the preform with a higher Δn has more P ions in the core, which often corresponds a higher Bi concentration than the preform with a lower Δn. However, it should also be noted that the actual deposition rate between Bi and P may not always follow the same rate as that in the solution, as fabrication conditions during MCVD process can impact the final product.

To gain a more accurate understanding of the glass composition in both the preforms and fibres, two techniques were utilised to determine the radial distribution of the chemical composition in the core: secondary ion mass spectrometry (SIMS) and electron probe micro-analysis (EPMA).

The SIMS analysis was conducted by Loughborough Surface Analysis Ltd, UK. This technique provides a direct analysis of composition of solid surface and thin film. It involves the bombardment of a sample surface with a primary ion beam, which then result in a eject of the charged secondary ions from the surface. These ions are then analysed by a mass spectrometer to identify and quantify the elements existing in the sample [6]. In this study, the measurement was performed on preform slices with a diameter of around 9 mm, or BPSFs with a core and cladding diameter of 12 and 125 μm, respectively. The SIMS linescan measurements were performed at an interval of 2 μm. The SIMs intensity profile of preform L10619 is presented in Figure 4.2 as an example, revealing the presence of Si, O, P and Bi ions. The number indicated in front of each element corresponds to its molar mass. The distribution of Si and O was found to be uniform, as these ions exist as SiO_2 in both the cladding and core in the preform. Conversely, the distribution of P and Bi ions follows the refractive index profile of the preform. This method can provide a qualitative comparison of the elements in the preform, however the calculation of Bi concentration was not possible due to the absence of a standard profile for comparison. However, it is worth comparing the ratio between the intensity of Bi and P among different BPSFs, as it might establish a relative relationship between the fibre's concentration and other characteristics, such as the NIR absorption or the UL.

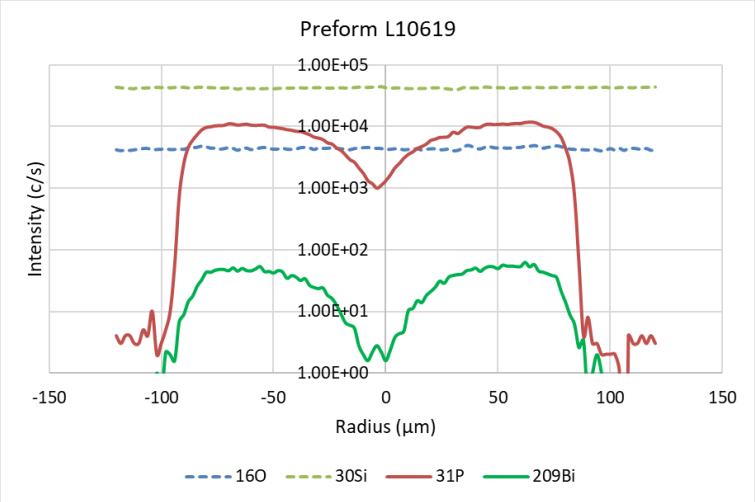

Figure 4.2 SIMS analysis result of the preform L10619, showing the distribution of O, Si, P, and Bi ions.

The EPMA analysis was performed by the University of Massachusetts, USA. The analysis works by directing a focused electron beam onto the fibre and detecting the X-ray photons emitted by the various elemental species present in the core [7]. The wavelength of these X-rays is dependent on the emitting species, thus allowing the identification of composition and distribution by recording the spectrum. Figure 4.3 displays the distribution of P and Bi in BPSF L10626-A1353 and L10645-A1450 along a 30 µm diameter scan with 1 µm step. For the purpose of clear presentation and comparison, the concentration of Bi was magnified by a factor of 100. The fluctuation of Bi concertation observed in the two fibres is attributed to EPMA noise. The calculated concentration of Bi and P ions in the BPSF samples are listed in Table 4.2. The absorption at 1240 nm of these two fibres are given for comparison. When the glass was doped with 0.004 mol% Bi ions, an absorption of 0.57 dB/m was observed, while a doping concentration of 0.014 mol% resulted in an increase in absorption of approximately three times. The values are calculated by integrating the concentration profile along the core area and taking the effective result.

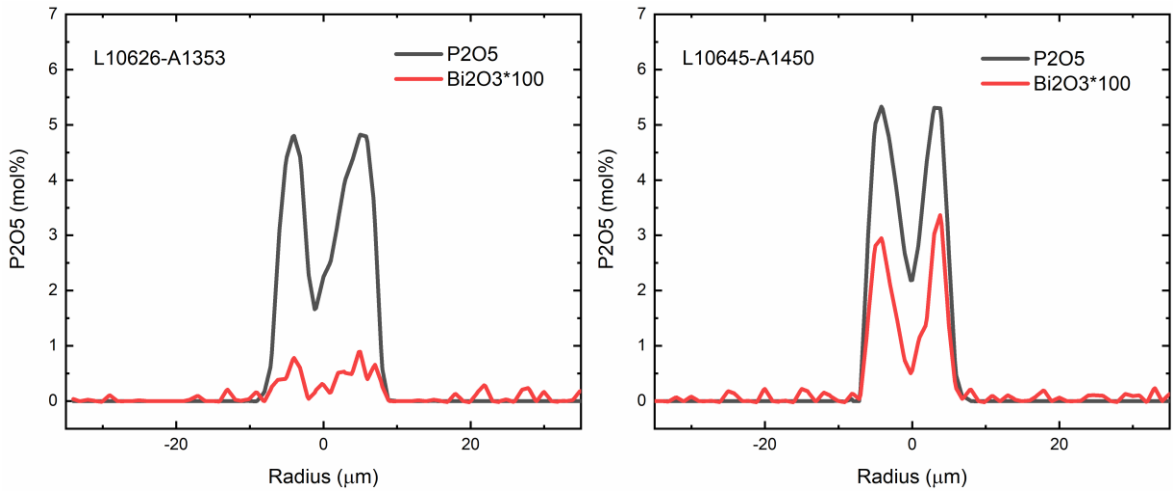

Figure 4.3 Radial distribution of P_2O_5 and Bi_2O_3 in mol% for fibres L10626-A1353 (left) and L10645-A1450 (right) determined by EPMA. (The concentration of Bi was magnified by a factor of 100).

Table 4.2 Concentration of Bi and P in BPSF measured using EPMA technique.

(The concentration of Bi presented here represents an average across the core area, while the Al results correspond to peak values)

Analysis	Preform No.	Fibre No.	Bi_2O_3 (mol%)	P_2O_5 (mol%)	Δn	Absorption @1240nm(dB/m)
EPMA	L10626	A1353	0.004	4.80	0.004	0.57
	L10645	A1350	0.014	5.28	0.006	1.3

It needs to be noted that different chemical analysis methods such as the SIMS and EPMA sometimes provide different values for the same sample. That is the limitation of these technique. Although in our study the SIMS cannot provide an exact concentration of Bi ions, it is still worth to using multiple methods and compare the results.

4.3.2 Fundamentals of optical fibre loss and absorption

The loss of an optical fibre can be classified intrinsic and extrinsic. The intrinsic loss is primarily caused by ultraviolet absorption, infrared absorption, and Rayleigh scattering [8]. Figure 4.4 illustrates the fundamental loss of silica-based fibres. The lowest loss of a silica glass fibre is limited by the Rayleigh scattering at short wavelengths and infrared absorption at long wavelengths, and the minimum value occurs at a wavelength around 1550 nm. On the other hand, extrinsic loss can result from micro and macro bending or any impurities in the glass. Hydroxyl (OH-) groups as one of the impurities, can be identified by observing the

loss at specific wavelengths. In a silicate fibre, absorption peaks at 950 nm, 1240 nm, and 1380 nm are indicative of OH- groups with corresponding absorptions of 1, 2 and 50 dB/km, respectively, at an OH- concentration of 1 ppm [8].

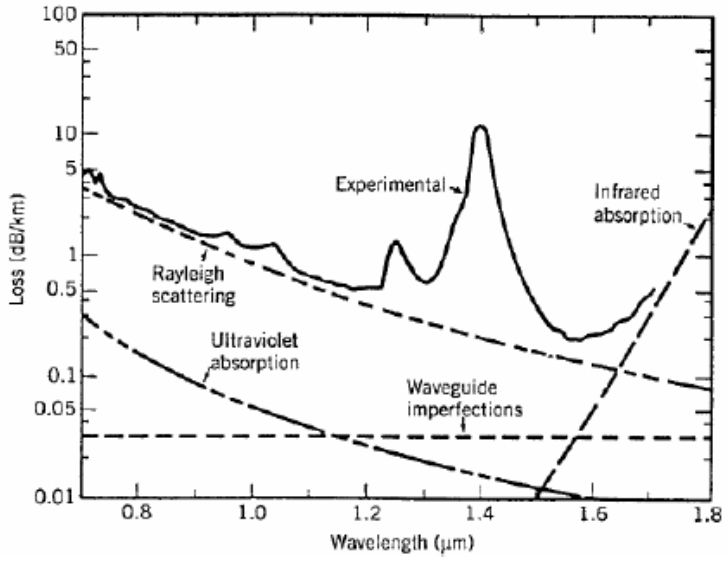

Figure 4.4 Fundamental loss of silica fibres including Rayleigh scattering, UV absorption and infrared absorption at different wavelength bands [4]

The absorption spectrum represents the fraction of incident light absorbed by the material at certain wavelengths. Special absorption bands will occur if there are any active dopants in the material, such as Bi ions in our BDFs. The small signal absorption was measured based on the conventional cut-back technique. The schematic diagram of the setup is shown in Figure 4.5, including a white light source (WLS) as input, a collimated objective to launch the light into the fibre under test (FUT), and an optical spectrum analyser (OSA, Yokogawa AQ-6315A in this study) to collect the transmitted light through the fibre.

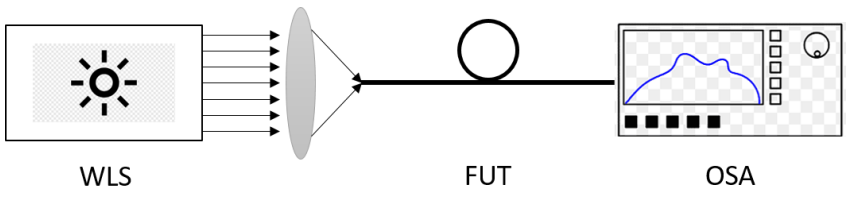

Figure 4.5 Schematic of the absorption measurement setup

In theory, the power of incident light is expected to experience an exponential decrease after propagating a certain length of the fibre, which can be expressed as:

$$P = P_0 e^{-\alpha L} \tag{4-2}$$

Where L is the fibre length, P_0 is the initial power of light launched to the fibre. α is the attenuation coefficient. By changing the propagating fibre length, we have:

$$P_1 = P_0 e^{-\alpha L_1}, P_2 = P_0 e^{-\alpha L_2} \tag{4-3}$$

Therefore, the absorption coefficient is calculated as:

$$\alpha(m^{-1}) = \frac{lnP_2 - lnP_1}{L_1 - L_2} = \frac{ln\frac{P_2}{P_1}}{L_1 - L_2} \tag{4-4}$$

As mostly the active fibre absorption is measured in dB/m unit, the equation is revised as:

$$\alpha(dB/m) = 10\frac{log\frac{P_2(mW)}{P_1(mW)}}{L_1 - L_2} = \frac{P_2(dBm) - P_1(dBm)}{L_1 - L_2} \tag{4-5}$$

Therefore, the absorption spectra can be measured by recording the intensity of the output light across a wavelength range with a constant input and varying fibre lengths. In this study, the absorption was measured in a continuous wavelength range from 350 to 1750 nm. Measured absorption spectrums in this wavelength range will be given in section 4.3.4 (Figure 4.8) for BPSFs and in section 6.4 (Figure 6.5) for BASFs. The length of the fibre depends on the absorption level at the target wavelength and is typically 100m and 10m for background loss and near-infrared absorption, respectively.

4.3.3 Fundamental of unsaturable loss

BDFs are known to exhibit unsaturable loss (UL), where the absorption at a certain wavelength, usually pump wavelength, differs when the incident power is at a small signal or a relative high level. This phenomenon is typically observed in both RE-doped fibres and BDFs due to interaction between active ions. It becomes particularly significant at high concentrations of these active ions and can have a large impact on the fibre performance. Figure 4.6 depicts a diagram illustrating the concept of ion interactions, including cooperative upconversion, cross relaxation and energy migration, which have been observed in RE-doped fibres [9]. In the cooperative upconversion process, a first excited ion transfers its energy to a second excited ion and returns to ground level. The second ions also release its energy by a radiative or non-radiative emission. During cross relaxation process, a first ions at excited state transfers part of its energy to its neighbouring ion, leaving both ions at an intermediate level and eventually decay to the ground state. When certain energy matching conditions are achieved, energy migration process occurs with a

first excited ion gives its energy to a different ion, lifting it from the ground level to a higher level and then decay to the upper level of the desired laser process.

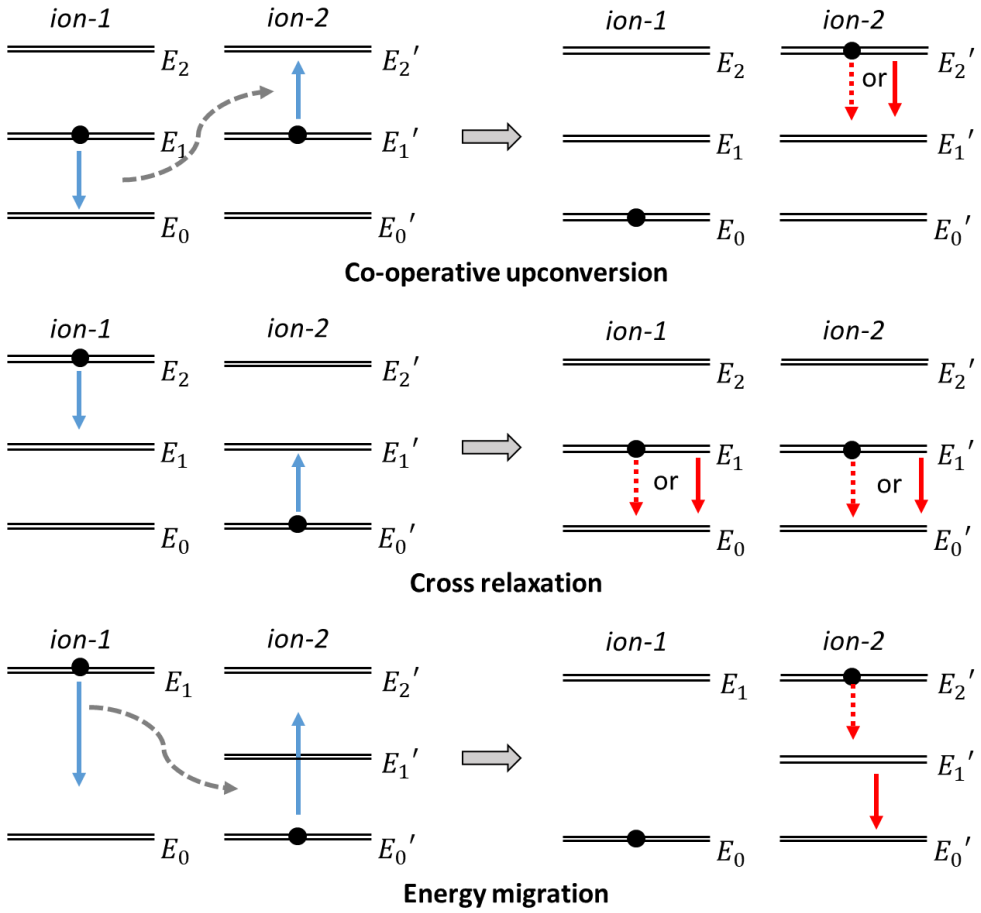

Figure 4.6 Ion-to-ion interactions existing in RE-doped fibres including co-operative upconversion, cross relaxation, and energy migration [9]. The solid-red arrow represents the radiative emission, and the dashed-red arrow indicates the fast decay of the ions.

During ion interaction, energy can be transferred to undesired levels and become wasted through non-radiative decay. Such processes can induce additional loss in the system, known as UL, and will influence the population inversion, ultimately decreasing the efficiency of the related laser systems. Research has shown that an increase in UL of BDFs typically results in poor laser and amplifier performance [10]. A concentration dependence of the UL has also observed in BDFs [11].

In this study, the UL of all the BPSFs were measured using the experimental setup illustrated in Figure 4.7. A laser diode (LD) at 1240 nm was employed to pump the fibre,

followed by an isolator (ISO) to prevent any damage due to back-reflected light. An attenuator (ATT) was connected after the isolator to achieve a small signal power level below -20 dBm. Ninety-five percent of the pump power was launched into the fibre under test (FUT), while the remaining 5% was used as a reference to monitor the incident pump power to the FUT when the attenuator was adjusted. The pump power was varied in 5 dBm steps, ranging from -35 dBm to the maximum available power provided by the laser diode, to attain the pump saturation level of the BPSF. The loss measured at low pump power should be the same as the small signal absorption measured using the cutback technique by WLS. The percentage of the loss at the saturation to the small signal absorption was used to indicate the UL in the fibre. The length of FUT for UL measurement is typical around 1-2 m to avoid any influence from the amplified spontaneous emission (ASE) generating in the fibre.

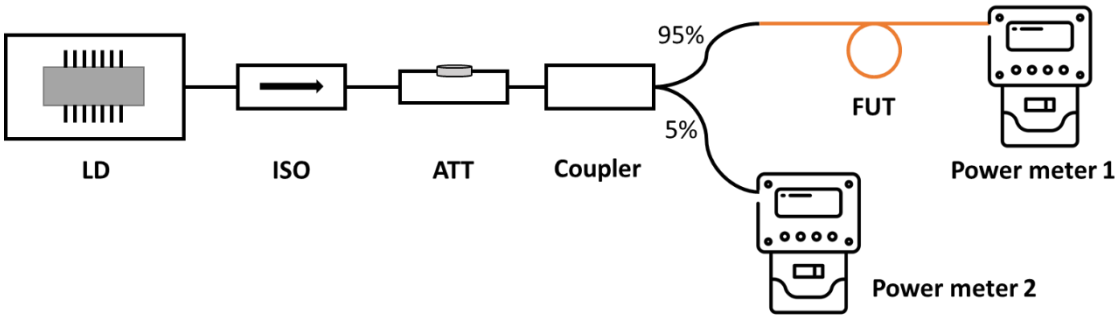

Figure 4.7 Schematic diagram for UL measurement setup. LD: laser diode; ISO: isolator; ATT: attenuator; FUT: fibre under test

4.3.4 Experimental results and discussion

Figure 4.8 shows a typical absorption of BPSFs from 400 nm to 1700 nm, as measured by an OSA with a resolution bandwidth of 10 nm. The fibre lengths were varied for different wavelength ranges: 0.5 m for 400-600 nm, 1 m for 600-900 nm, 10 m for 900-1400 nm, and 100 m for 1400-1700 nm. The inset in Figure 4.8 shows the absorption in the NIR range of 1.1-1.5 µm. Particularly, the wavelength range of 1.2-1.3 µm is commonly used for pumping of BPSFs. The small peak observed at ~1380 nm corresponds to the loss contributed by OH bond. The spectrum shows three distinct absorption bands: 420-440 nm, 700-750 nm, and 1200-1300 nm. These bands are contributed from the active centre formed by Bi and P ions (BAC-P), while small peaks sitting above the broad absorption curve at ~490 nm, ~785 nm might originate from the active centre of Bi and Si ions (BAC-Si) [12]. These peaks are

compressed by the presence of BAC-P in BPSFs. Additionally, BAC-Si also causes absorption at approximately 1420nm, although it is overshadowed by the BAC-P's broad absorption band at 1.2~1.3 μm. Figure 4.9 presents the absorption spectra for different BPSFs fabricated in this study, as listed in Table 4.1. The absorption peaks contributed by BAC-P and BAC-Si, as well as the loss coming from OH are marked at the corresponding wavelengths. The absorption at 1270nm is around 0.5 dB/m except for L10625, L10642 and L10645. The lower absorption of L10625 (0.29 dB/m) resulted from the less incorporation between the solution and soot that was deposited under a higher temperature (details in Table 4.1), while the higher absorption (0.74 and 1.26 dB/m, respectively) of L10642 and L10645 is due to higher Bi concentration in the solution.

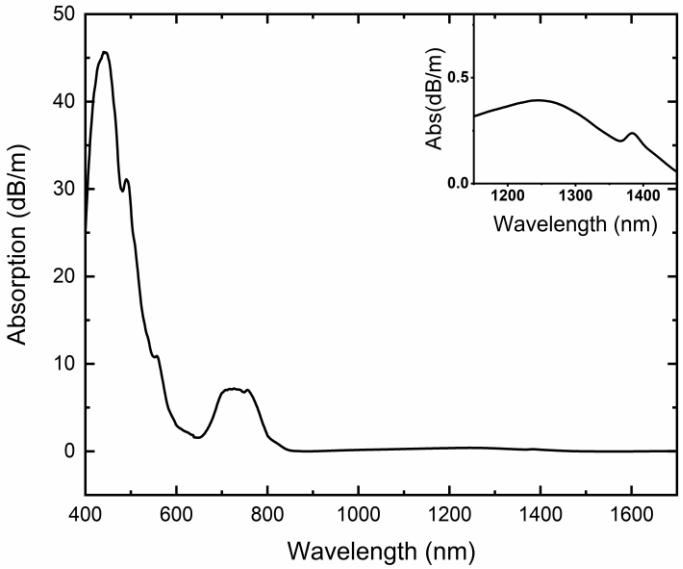

Figure 4.8 Absorption of BPSFs measured with 10nm resolution bandwidth.

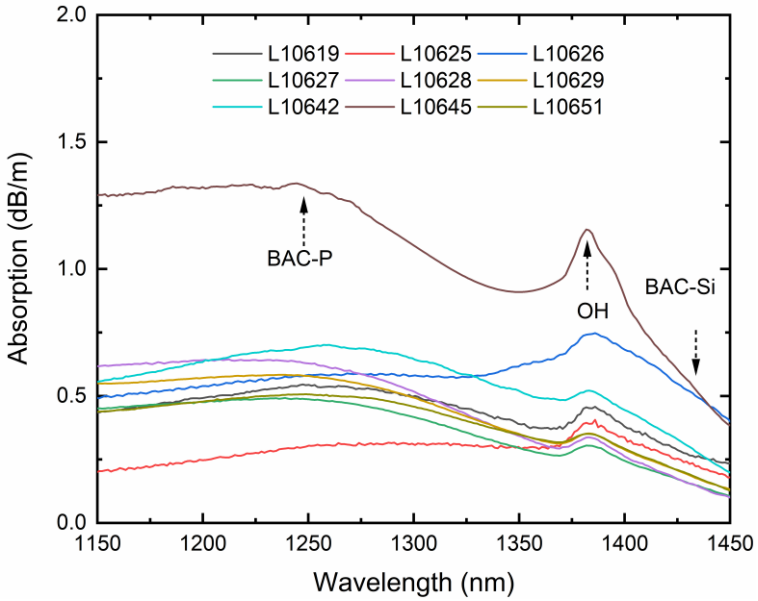

Figure 4.9 Absorption spectrum of different BPSFs within the range of 1150-1450 nm

Figure 4.10 illustrates the power-dependent behaviour of the UL in a BPSF, measured at 1240 nm. At low input powers below -20 dBm, the absorption remains relatively high, which should be the same as the small signal absorption at the same wavelength measured using the WLS. As the input power increases to 0 dBm, the absorption gradually drops and saturates at a relatively low level with an incident power above 20 dBm. In this case, the small signal and saturated absorption were measured to be ~0.38 and ~0.05 dB/m, respectively, corresponding to a UL ratio of 13%.

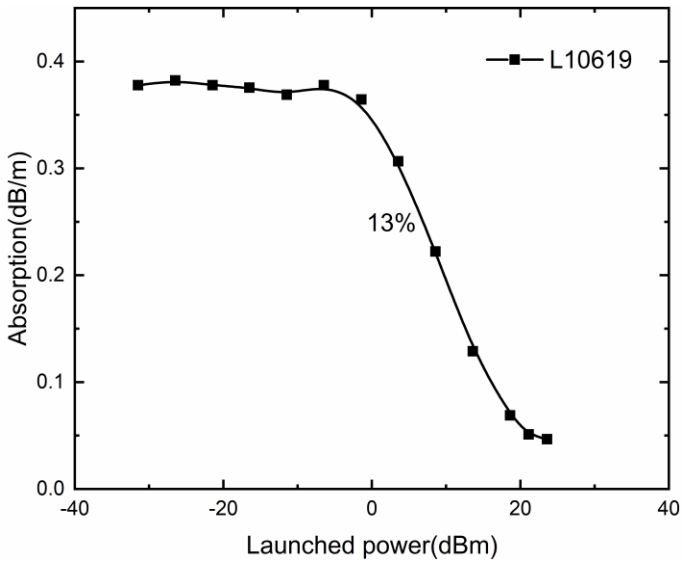

Figure 4.10 Typical BPSF absorption vs launched power at 1240nm

Table 4.3 Absorption and UL of BPSFs

Preform No.	Fibre No.	Absorption at 1270nm (dB/m)	Background loss at 1550nm (dB/m)	OH (ppm)	UL at 1240nm (%)
L10619	A1340	0.50	0.02	2~3	13
L10625	A1351	0.29	0.03	2~3	12
L10626	A1353	0.57	0.03	2~3	13
L10627	A1356	0.50	0.04	0.8	17
L10628	A1359	0.63	0.04	0.8	17
L10629	A1368	0.58	0.04	0.8	16
L10642*	A1435	0.74	0.05	0.8	21
L10645*	A1350	1.26	0.07	0.7	23

*Different solutions with high Bi concentration were used

Details of measured absorption and UL in BPSFs in this study are summarised in Table 4.3. The UL measurement was conducted at 1240nm, with results closely resembling those at 1270 nm. Figure 4.11 and Figure 4.12 show the relationship between Bi absorption and the UL and background loss, respectively, for different BPSFs. These figures clearly demonstrate that, with Bi absorption increases in the NIR wavelength band, the background loss and UL increase correspondingly. It is essential to achieve a balance between absorption and UL to ensure optimal performance and high efficiency of the Bi-doped fibre lasers.

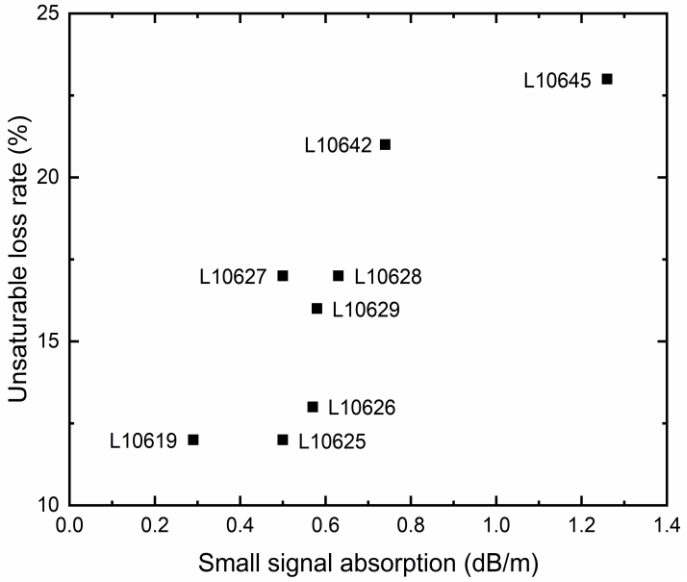

Figure 4.11 Unsaturable loss against small signal absorption of different BPSFs

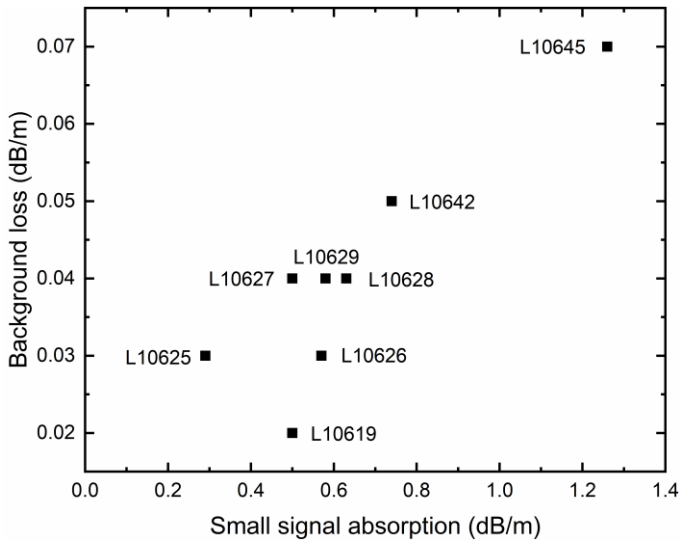

Figure 4.12 Background loss against small signal absorption of different BPSFs

4.4 Conclusion

The MCVD-solution doping technique was employed to fabricate a range of BPSFs, which were characterised by measuring their absorption and unsaturable loss. Additionally, some BPSFs underwent further analysis, such as SIMS and EPMA, to investigate their glass compositions and dopants distributions. A reproducible process has been established that yields BPSFs with excellent laser performance. Further details about the fibre performance will be discussed in the next chapter.

4.5 Reference

[1] Y. Wang, N. K. Thipparapu, S. Wang, P. Barua, D. J. Richardson, and J. K. Sahu. “Study on the temperature dependent characteristics of O-band bismuth-doped fiber amplifier.” *Optics Letters* **44**(23) 5650-5653(2019).

[2] S. Wang, Y. Wang, N. K. Thipparapu, M. Ibsen, D.J. Richardson, and J. K. Sahu, “All-fiber wavelength-tunable Bi-doped laser employing a fiber Bragg grating operating in the 1300nm band,” Conference on Lasers and Electro-Optics Europe (CLEO), OSA Technical Digest (Optical Society of America, 2020), paper STh1P.7.

[3] K.L. Walker, F.T. Geyling, and S.R. Nagel, “Thermophoretic deposition of small particles in the modified chemical vapor deposition (MCVD) process.” Journal of the American Ceramic Society, 63(9-10), 552-558 (1980).

[4] P. Atkins, and T. Overton, (2010), Shriver and Atkins' inorganic chemistry. Oxford University Press, USA.

[5] Y. Wang, S. Wang, A. Halder, and J.Sahu, “Bi-doped optical fibers and fiber amplifiers.” *Optical Materials: X*, **17**, 100219 (2023).

[6] P. Williams, “Secondary ion mass spectrometry,” Annual Review of Materials Science, **15**(1), 517-548, (1985).

[7] S. J. Reed, *Microprobe Techniques in the Earth Sciences*, ch. , Electron probe microanalysis.

The Mineralogical Society, Springer, 1995.

[8] A. Ghatak, and K. Thyagarajan, “Basic characteristics of the optical fiber,” in *An introduction to fiber optics*, Cambridge university press. 40(1998).

[9] S. Colin, E. Contesse, P. L. Boudec, G. Stephan, and F. Sanchez, "Evidence of a saturable-absorption effect in heavily erbium-doped fibers". *Optics letters* **21**(24), 1987-1989(1996)

[10] M. P. Kalita, S. Yoo, and J. K. Sahu, "Bismuth doped fiber laser and study of unsaturable loss and pump induced absorption in laser performance," *Optics Express* **16**, 21032-21038 (2008)

[11] S.V. Firstov, V.F. Khopin, F.V. Afanas'ev, A.M. Khegai, S.V. Alyshev, K.E. Riumkin, , N.N. Vechkanov, A.N. Abramov, M.A. Melkumov, , A.N. Guryanov, and E.M. Dianov, "Unsaturable absorption in various Bi-doped optical fibers," In *Proceeding of Annual International Laser Physics Workshop*. 2017.

[12] S. V. Firstov, V. F. Khopin, I. A. Bufetov, E. G. Firstova, A. N. Guryanov, and E. M. Dianov. "Combined excitation-emission spectroscopy of bismuth active centers in optical fibers." *Optics express* **19**(20) 19551-19561(2011)

Chapter 5 Bi-doped phosphosilicate fibre lasers at 1.3 µm

5.1 Introduction

This chapter presents the study of the continuous-wave (CW) Bi-doped fibre laser (BDFL) based on Bi-doped phosphosilicate fibres (BPSFs). Firstly, a free running cavity was built to observe the laser behaviour and its operating wavelength. Afterward, the laser was modified by inserting a commercial fibre Bragg grating (FBG) in the cavity to define the operating wavelength at 1340 nm (see Section 5.2). The cavity was optimised for maximum output power and slope efficiency by adjusting the fibre length and the coupling ratio. Eventually, to demonstrate the tuning capability of the laser, two tuning components an optical filter and a compression-based tunable FBG (each induced separately) were utilised in the cavity. The results of these tests are presented in Section 5.3 and 5.4, respectively. Section 5.5 presents the study of a master oscillator power amplifier (MOPA) system by connecting the tunable BDFL to a Bi-doped fibre amplifier (BDFA). At the end, Section 5.6 summarised the establishment of the BDFL. This study has been reported in [1-5].

5.2 Bi-doped phosphosilicate fibre laser at 1.3µm band

5.2.1 Experimental setup

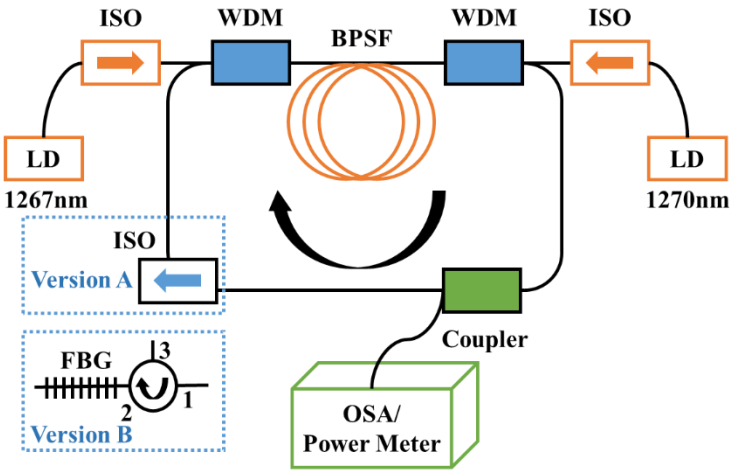

Figure 5.1 Schematic diagram of setup of the CW BDFL. LD: laser diode; ISO: isolator; WDM: wavelength division multiplexer; FBG: fibre Bragg grating (Version A: free running cavity setup; Version B: laser cavity at operating wavelength of 1340nm)

At the beginning of the study, a BDFL was constructed using a free running ring cavity configuration, illustrated in Figure 5.1 (version A). The design of the ring cavity is based on prior study where a linear cavity was unable to provide lasing for our BPSFs. Different BPSFs were pumped bi-directionally by two laser diodes (LDs) operating at 1267 nm and 1270 nm with a total incident pump power around 700 mW. The forward and backward pump power were similar, each around 350 mW. To prevent damage from back reflection within the cavity and any unabsorbed pump light passing from one pump diode to the other, two isolators (ISOs) were employed following the LDs. Two filter wavelength division multiplexers (WDMs) were used in order to combine the pump and signal beams. One port of the WDMs transmitted at 1270 nm, while the other had a flat transmission spectrum from 1300 to 1380 nm. To maintain the unidirectional operation of the ring cavity, an isolator was utilised, while a coupler was used to extract the output power from the cavity. The laser cavity was adjusted by using different fibre length and output coupling ratio. The output power and spectrum were monitored using a power meter and an OSA, respectively.

It was observed that the free running cavity exhibited two lasing peaks at 1360 and 1430 nm, which were believed to be generated from different Bi active centres with P and Si (BAC-P and BAC-Si). To select a specific lasing wavelength, a fibre Bragg grating (FBG) was introduced into the ring cavity via a circulator, as illustrated in Figure 5.1 (version B). The isolator was no longer necessary as the circulator ensured unidirectional operation. The FBG had a high reflectivity of 99% and operated at 1340 nm, which was chosen because it was at the centre of the gain profile of the BPSF pumped at 1270 nm and 1267 nm. Figure 5.2 presents the ASE spectrum of the same fibre when the pump power was increased from 200 mW at 1270 and 1267nm and increased by every 100mW. The left peak centres at 1340 nm and shifts towards 1360 nm as the pump power increased. The entire band gain spectrum ranged from 1300 to 1380 nm. Meanwhile, the right ASE peak accumulates and eventually centres at 1430 nm. With regard to the subsequent study of the tunable laser, the central wavelength (1340nm) was selected to obtain a broader tuning bandwidth. Based on this choice, the cavity was then modified.

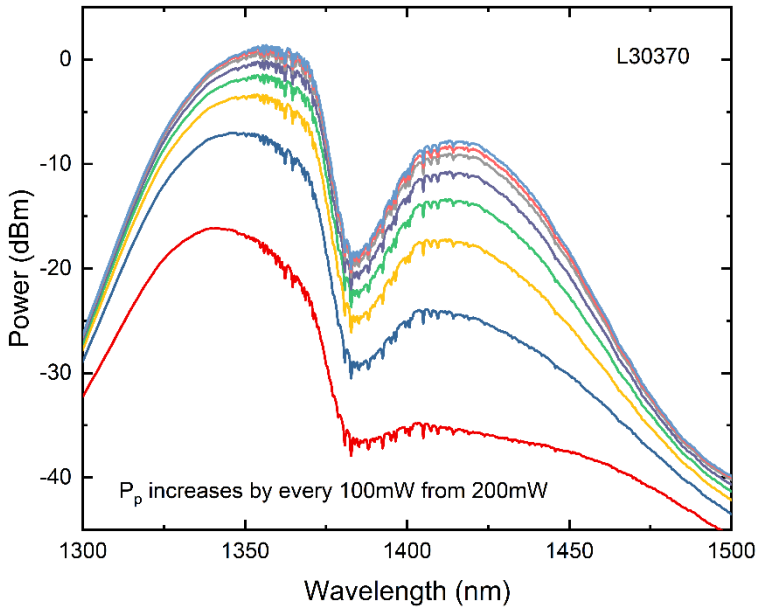

Figure 5.2 ASE spectrum of the BPSF pumped at 1270 and 1267nm with the power increased gradually by every 100mW, starting from 100mW, measured by 2nm resolution bandwidth.

5.2.2 Results and discussion

Table 5.1 Maximum power and slope efficiency in the ring laser setup

Fibre No.	Max Output power (mW)	Slope efficiency (%)	Fibre length (m)	Output ratio (%)
L30370	100	15	70	50
L10619	172	38	200	90
L10626	150	30	100	70
L10628	109	23	200	80
L10629	120	24	100	70
L10642*	118	22	90	70
L10645*	35	11	50	70

* Cavity not optimised with different fibre length and couplers

Table 5.1 summarises the laser performance of the several BPSFs tested in the ring laser cavity, including the maximum output power and slope efficiency with respect to incident pump power of approximately 700 mW. Additionally, the corresponding fibre length for each BPSF and the output coupling ratio are provided in the table. L30370 was tested using the free-running cavity (version A), while the remaining BPSFs were measured using the configuration with an FBG implemented (version B). The absorption and UL of these fibres can be found in section 4.3.4 (Table 4.3). (L30370 was fabricated before this study, with the absorption and UL of 0.59 dB/m and 16% at 1270nm). The lifetime of these BPSFs is around

740-780 μs. The absorption cross-section (σa) and the emission cross-section (σe) are approximately 2.7 and 1.8 pm^2 at 1295 and 1360 nm respectively, as mentioned in section 4.1.

For L30370, the fibre length and output coupling ratio of the cavity were modified to achieve the highest output power of 100 mW under a full pump power of approximately 770 mW. The slope efficiency was measured to be 15%. Figure 5.3 presents the output spectrum measured by an OSA with a resolution bandwidth of 0.5 nm, under full pump power. The fibre exhibited a gain spectrum ranging from 1300 to 1380 nm and from 1380 to 1480 nm. In the absence of an FBG in the cavity, lasing occurred at two wavelengths simultaneously, with slightly higher power observed at 1360 nm than at 1430 nm. The decrease in gain at 1380nm was caused by the OH absorption existing in the fibre. Once the FBG at 1340 nm was employed, lasing at 1430 nm was prevented and the lasing was forced to happen only at 1340 nm.

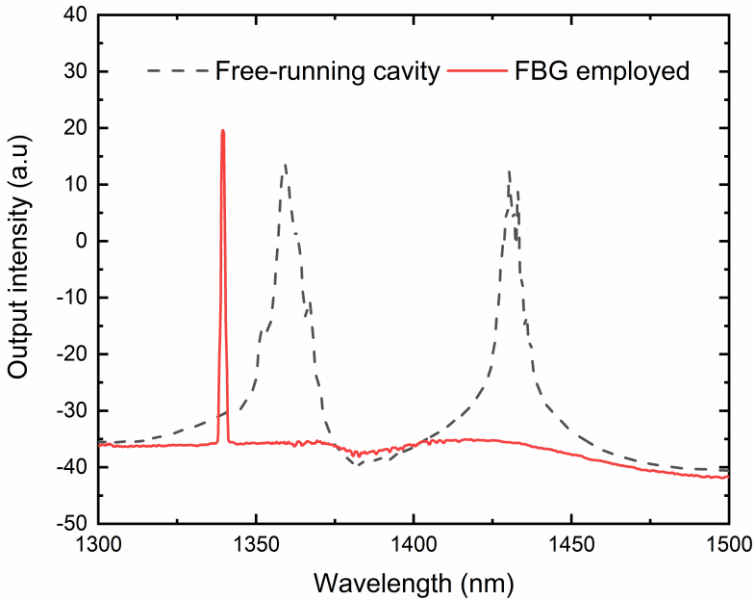

Figure 5.3 Spectrum of free running cavity with L30370 under full pump of 770 mW, measured with 0.5 nm OSA resolution bandwidth.

In the case of dual wavelength lasing, the total output power was divided between 1360 nm and 1430 nm by integrating the two peaks in the spectrum. Figure 5.4 depicts the change in output power at each wavelength as the pump power increases. The threshold for lasing at 1360 nm is below 100 mW, while it increases to 150mW for lasing at 1430nm. The maximum output power was calculated to be 70mW at 1360nm and 30mW at 1430nm,

with corresponding slope efficiencies of 9.47% and 4.8% respectively. As explained in Section 4.3, the emission at 1360nm arises from the active centre formed by Bi and P ions (BAC-P) while the 1430nm lasing is associated with the active centre of Bi and Si ions (BAC-Si). BAC-P dominates the absorption and gain in the BPSF, resulting in higher output power and slope efficiency at 1360nm than those at 1430nm.

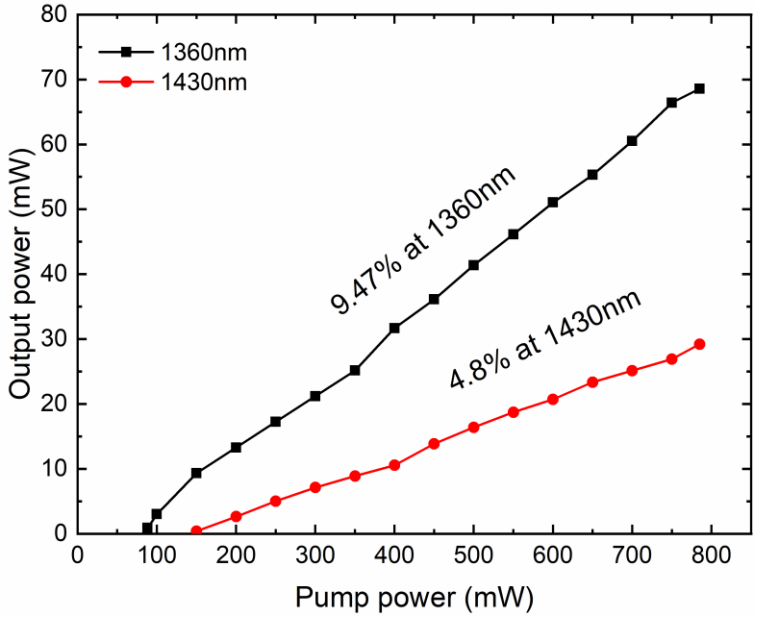

Figure 5.4 Output power of the laser with L30370 at different pump power, at different wavelength (black: signal at 1360 nm; red: signal at 1430 nm)

The presence of a second lasing peak at 1.4 μm resulted in a consumption of pump power and reduction of pump efficiency at the desired lasing wavelength of 1.3 μm. To overcome this issue, a FBG at 1340 nm was introduced in the ring cavity (version B in Figure 5.1). This configuration was used to test all the other BPSFs.

Among the fibres listed in Table 5.1, L10619 exhibited the best laser performance in terms of both the output power and slope efficiency. Fibres with lengths ranging from 100 m to 250 m were tested, and couplers with output coupling ratios between 30% to 90% were used at each length. Figure 5.5 illustrates the change in output power as the pump power at different output ratios. The four sub-figures correspond to the fibre length of 100, 150, 200 and 250 m. In each case, the BPSF was pumped with an incident power varied from 100 to 700 mW.

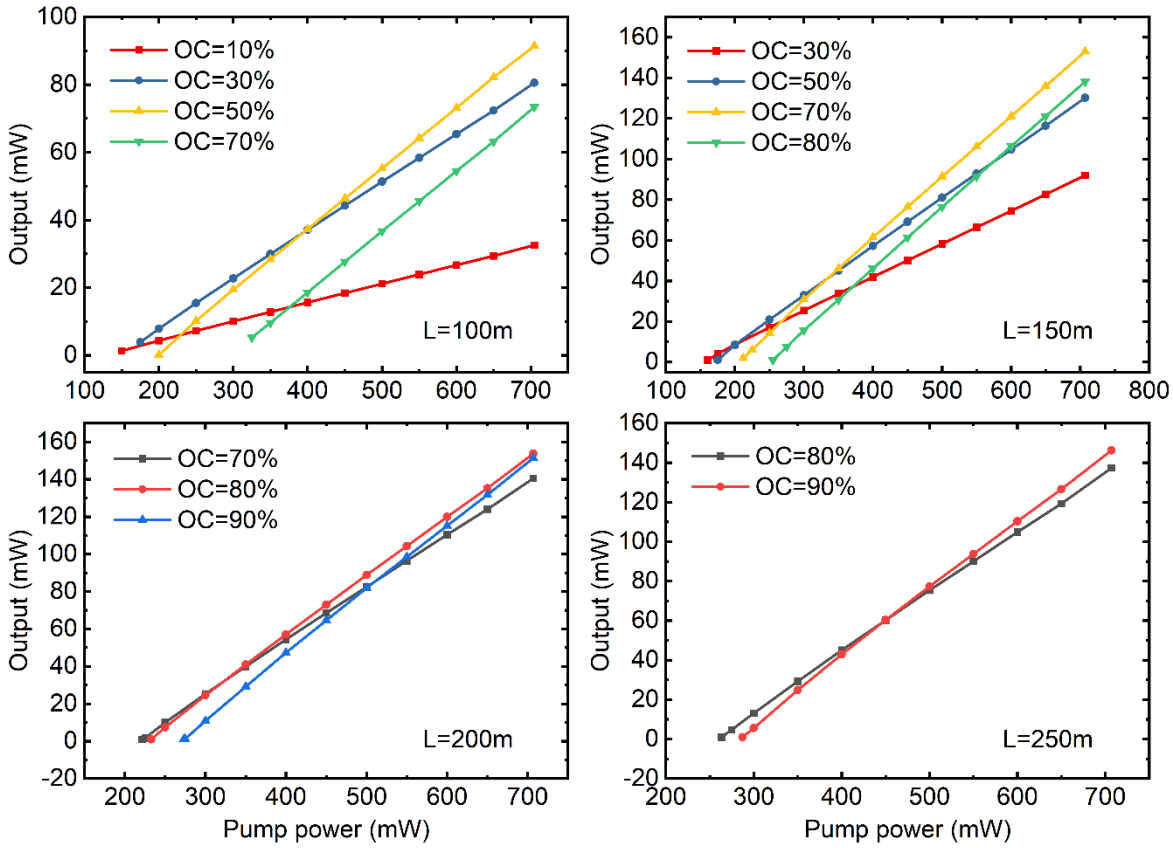

Figure 5.5 Laser output power of BPSF L10619 versus incident pump power at different output coupling ratios. The sub-figures are arranged sequentially starting from 100 m and proceeding to 150, 200, and 250 m, respectively.

From Figure 5.5, it is clear that the laser threshold power, output power under full pump, and the slope efficiency with respect to incident power are all dependent on the cavity parameters, including the active fibre length and the output coupling ratio. For a fixed length of fibre, a higher output coupling ratio leads to greater inter-cavity loss, resulting in an increase of the threshold power. The slope efficiency also increases with an increase in output coupling ratio, as output power is extracted at a higher percentage of the total power generated in the fibre. However, beyond a certain output coupling ratio, the slope efficiency starts to decrease due to a combination of gain and loss in the cavity. The similar trend is also observed in the output power at a fixed pump power. The comparison of the threshold, output power and slope efficiency with different cavity parameters is summarised in Figure 5.6.

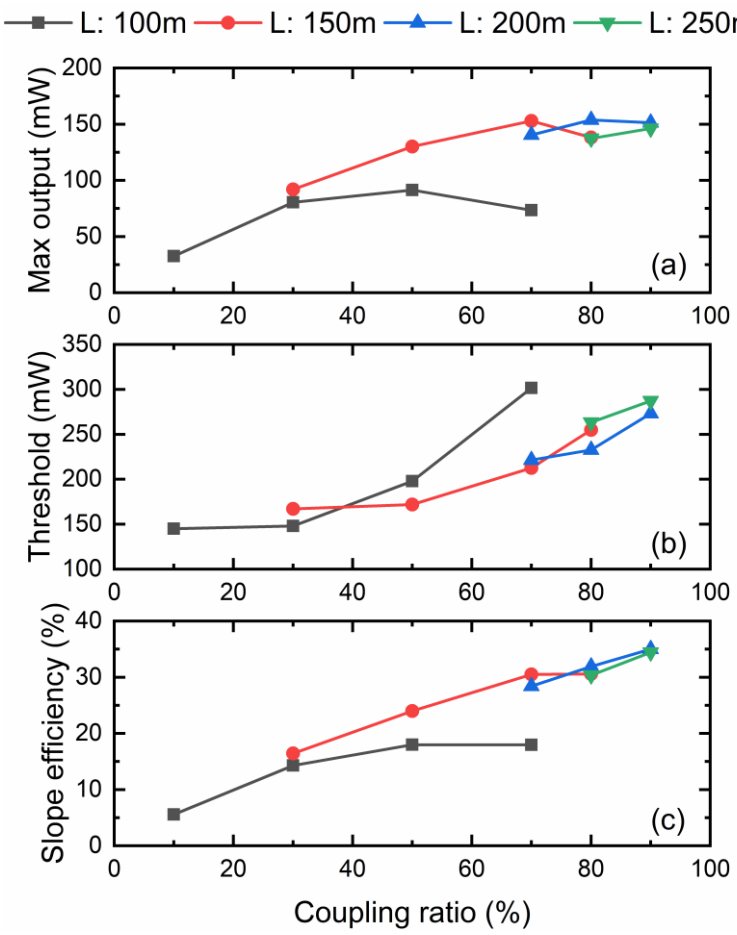

Figure 5.6 Change of laser output power under full pump power, threshold power, and slope efficiency with different output coupling ratios. Lines of different colours represent different fibre lengths.

Figure 5.6 describes the optimisation process for the laser cavity. By adjusting the coupling ratio (x axis), an optimised value of output power was reached preliminarily at a fixed fibre length. For instance, Figure 5.6 (a) shows that for a 100m fibre length, the output power curve reached its maximum value with an output ratio of 50%. Furthermore, by varying the fibre length (represented by different coloured lines), the maximum output power increased with a length of 100m to 200m and decreased with a length of 250m. The slope efficiency also varied accordingly, as shown in Figure 5.6 (c). There are three cases the output power exceeded 150mW: 150m fibre length at 70% output ratio, 200m fibre length at 80% output ratio, and 200m fibre length at 90% output ratio. Notably, the laser slope efficiency was higher with the 200m fibre than with the 150m fibre.

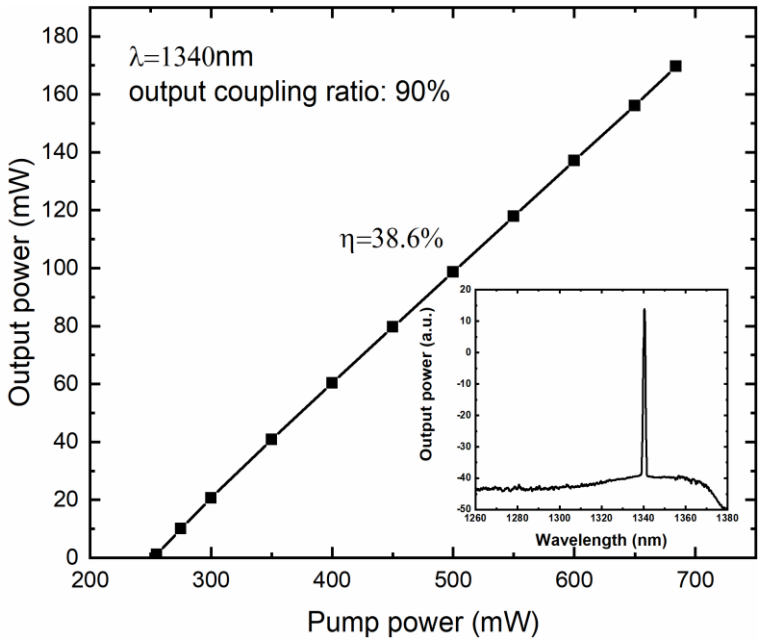

Figure 5.7 Spectrum of the laser output with 200m L10619

The optimisation process resulted in a final output power of 172mW and a slope efficiency of 38% for the laser, which is illustrated in Figure 5.7, by utilising the 200 m of L10619 and 90% output ratio. The output power is presented at different pump power and the spectrum of the output light under maximum pump power is given in the inset. The signal-to-noise ratio (OSNR) was greater than 50 dB and its linewidth was ~0.24 nm, measured with an OSA resolution bandwidth of 0.05 nm.

Previously, the maximum slope efficiency achieved with BPSFs at 1340 nm was 50% [6]. However, the result was achieved by using a pump power of over 20 W and led to serious issues of spectral broadening. At low pump power in the same work [6], the maximum slope efficiency achieved in BDFLs at 1340 nm in prior was less than 25%. In our experiment, the spectrum broadening was not observed, and the output maintained a stable linear correlation. To the best our knowledge, this is the highest slope efficiency with BPSFs at 1340 nm with low pump power.

5.3 Tunable Bi-doped fibre laser based on the optical filter

5.3.1 Experimental setup

After optimising the laser cavity at 1340 nm, two BPSFs, L30370 and L10619, were tested for the study of the tuning capability of the BPSF laser. The setup was modified as shown in Figure 5.8. Compared to the CW version at 1340 nm, the circulator and the wavelength-

fixed FBG were replaced by an isolator and a mirror optical filter (from WL Photonics Inc.). The filter had a tuning bandwidth from 1250-1375 nm and was tuned by every 5 nm. Within this tuning range, the filter had a full width at half-maximum (FWHM) of 0.45 nm, with a uniform insertion loss of 1.5 dB within the entire bandwidth. The isolator was to guarantee the unidirectional operation of the cavity. The pump diodes remained same at 1267 nm and 1270 nm. The fibre lengths here were chosen according to the optimised results when being tested in the prior BDFL study (Section 5.2), which were 70 m for L30370 and 200 m for L10619. The coupler was also changed to their corresponding optimised values. For the two fibres tested in this situation, L30370 and L10619, the couplers were 50:50 and 80:20 (80% output), respectively. Although 90% output ratio gave a higher slope efficiency, it would lead to a high pump threshold at the shorter and longer wavelength edges, thus an 80% output ratio was preferable in order to have a broader tuning bandwidth and more flat output power profile within the whole tuning range.

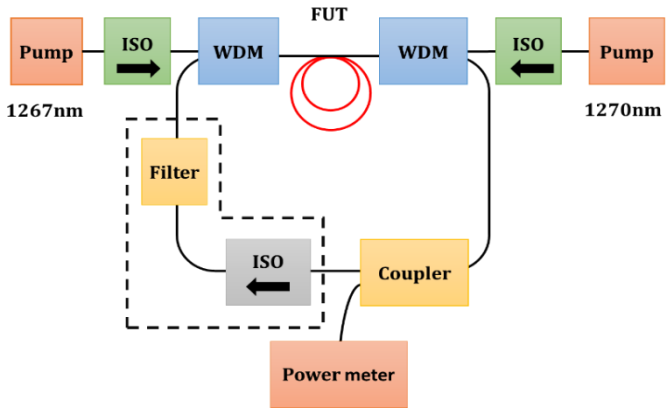

Figure 5.8 Schematic diagram of the tunable BDFL setup based on an optical filter. ISO: isolator; FUT: fibre under test.

5.3.2 Results and discussion

Table 5.2 is summarised the results of this study on tunable BDFLs using two BPSFs, L30370 and L10619. The table includes data on the maximum power, central wavelength, tuning bandwidth (FWHM of the output signal) and the OSNR.

Table 5.2 Details of the tunable BDFLs with fibre L30370 and L10619

Fibre No.	Maximum power (mW)	Max. at wavelength (nm)	Bandwidth (nm)	OSNR
L30370	60	1350	47	48
L10619	150	1340	60	40

With fibre L30370, the output power at different wavelengths of tunable BDFL is displayed in Figure 5.9. A maximum power of 60 mW was obtained at 1350 nm. The tuning bandwidth was 47 nm from 1323 nm to 1370 nm considering a 3 dB power decrease. The slope efficiency of the tunable laser at 1350 nm was measured to be 10%. Figure 5.10 presents the spectrum of the tunable laser under a full pump power of 700 mW, with an OSNR of 48 dB within the entire tuning range of 1315-1375 nm.

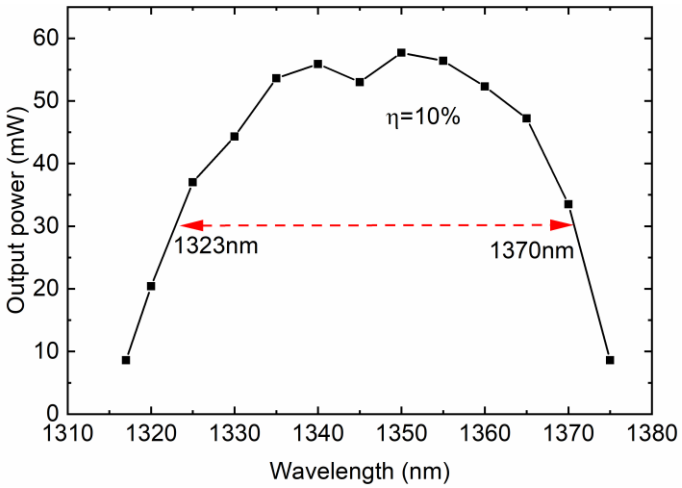

Figure 5.9 Output power of the tunable BDFL with L30370 from 1315 nm to 1375 nm (Dotted line: 30 mW power level)

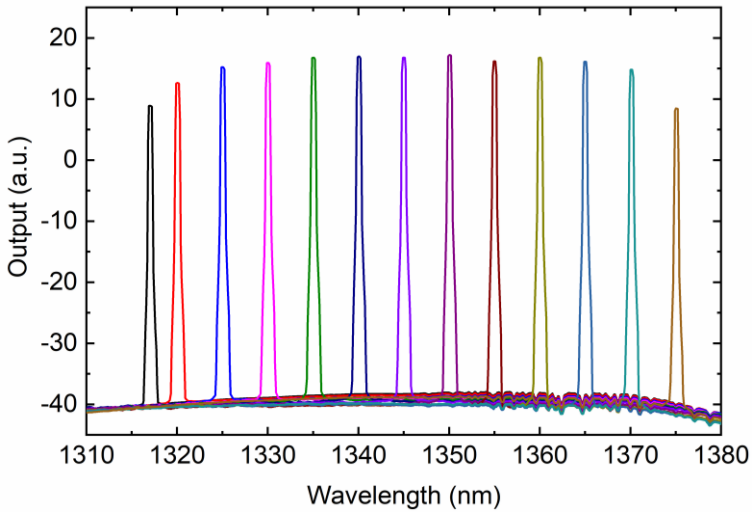

Figure 5.10 Spectra of the output light in the tunable BDFL with L30370, measured from 1317 nm to 1375 nm with 0.5 nm OSA resolution bandwidth.

Similarly, the BDFL with fibre L10619 was tuned from 1305 nm to 1375 nm by 5 nm. The output power at different wavelengths under full pump power was presented in Figure 5.11.

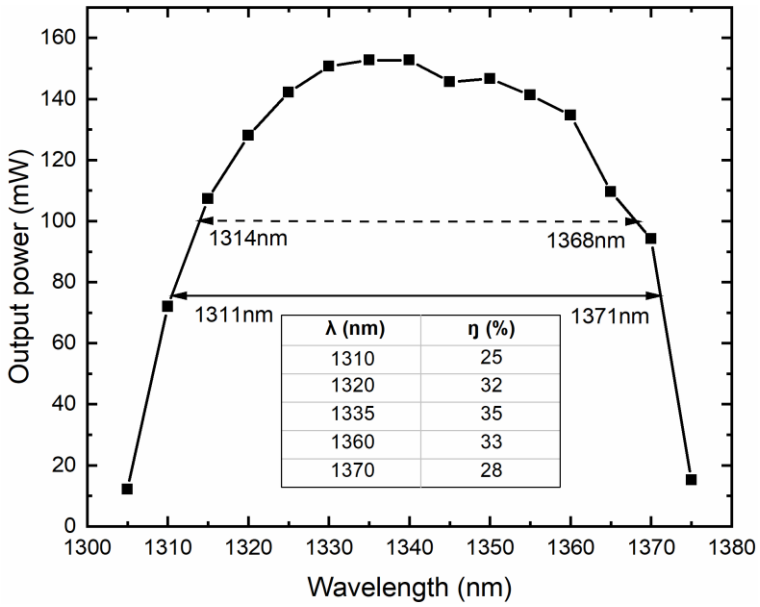

Figure 5.11 Output power at different wavelength of the tunable BDFL with L10619 (Dotted line: 100 mW power level; solid line: 75 mW power level); inset table: the optical slope efficiency at corresponding wavelengths.

As shown in Figure 5.11, the maximum output power was 150 mW at 1335 nm (±5 nm) and remained above 100 mW (dotted line) within a 54 nm range from 1314 to 1368 nm. Within the broad 60 nm bandwidth extending from 1311-1371 nm, the output power was above 75 mW (indicated as solid line), which represents a 3 dB drop compared to the maximum power. The sharp decrease at both shorter and longer wavelength edges was mainly because of the gain profile of the BPSF used. The inset of Figure 5.11 shows the slope efficiency of the tunable BDFL with respect to the incident pump power at different wavelengths. At 1335 nm, which gave the maximum output power, the efficiency was 35%. Within the 3 dB bandwidth (1311-1371 nm), the slope efficiency remained ≥25%.

Moreover, Figure 5.12 presents the spectrum of the tunable laser from 1305 to 1375 nm. The OSNR was above 40 dB across the entire tuning range, measured with an OSA resolution bandwidth of 0.5 nm, while the linewidth was around 0.07 nm, measured with an OSA resolution bandwidth of 0.02 nm.

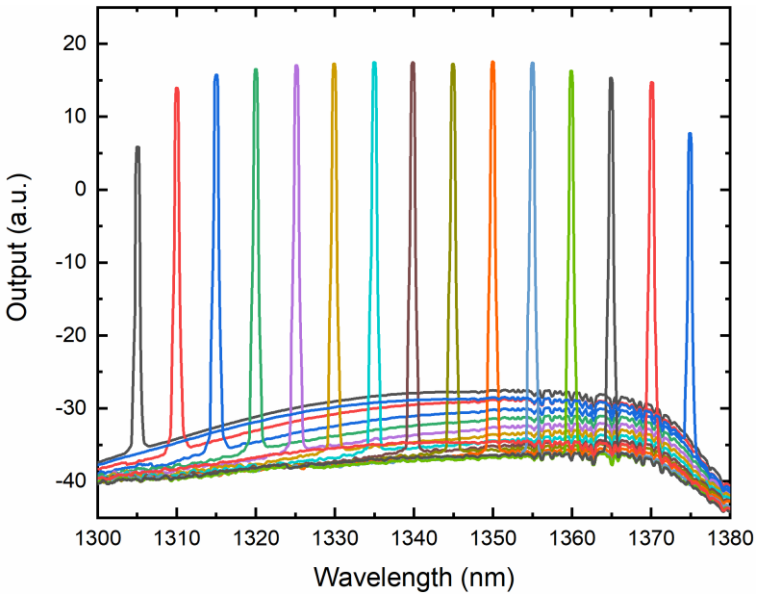

Figure 5.12 Spectrum of the tunable BDFL with L10619 from 1305 to 1375 nm, measured with 0.5 nm OSA resolution bandwidth.

In conclusion, two tunable BDFLs with BPSF L30370 and L10619 have been demonstrated. The tuning of the laser was realised by an optical filter. With L30370, the output power was maximum of 60 mW at 1350 nm. The tuning bandwidth was 47 nm from 1323 nm to 1370 nm, with over 48 dB OSNR within the range. With L10619, a maximum power of 150 mW was achieved from 1330 nm to 1340 nm, which was more than twice of BPSF L30370. This improvement was attributed to the development of the fibre with a slight reduction in the UL and lower ASE at 1.4 µm, originating from the BAC-Si. Additionally, the components in the cavity were also modified and optimised to reach a higher possible output power. The slope efficiency at 1335 nm was 35% and remained ≥25% across the full 3 dB tuning range, which was 60 nm from 1311 nm to 1371 nm.

5.4 Tunable Bi-doped fibre laser based on the fibre Bragg grating

In addition to optical filters, FBGs are also being used in tunable fibre lasers recently due to a range of advantages [7]. FBGs can serve as cheaper and cost-effective tuning elements than conventional optical filters, as well as with their lower component loss and more compact size. Compared to an optical filter, a FBG can be made with a smaller linewidth, which enables the production of narrower output light in the tunable laser. Furthermore, FBGs can accept higher power levels than optical filters, which opens up opportunities for power scaling in the future.

5.4.1 Principle of tunable fibre Bragg grating

The central wavelength of a FBG can be described as the formula below:

$$m\lambda = 2n_{eff} \cdot \Lambda \quad 5\text{-}1$$

Where m is an integer (usually is 1), n_{eff} is the effective refractive index of the FBG, and Λ is the period of the grating. By changing the n_{eff} or the grating period Λ, the tuning of the FBG operating wavelength can be achieved, which forms the fundamental principle of the entire theory.

The operating wavelength of the FBG is sensitive to both thermal and mechanical situations because both the refractive index and the period of the FBG can be influenced by the two conditions. Particularly, the refractive index change caused by the strain is typically disregarded since it is deemed to be negligible. In this study, the primary factor contributing to the wavelength shift of the FBG is the grating period. (The temperature was maintained at room temperature of ~25 ℃)

When a FBG experiences any temperature change or strain, the wavelength shift will follow the equation [8]:

$$\Delta\lambda/\lambda_B = \varepsilon_{ax} - \frac{n^2}{2} \cdot [\varepsilon_r \cdot (p_{11} + p_{12}) + p_{12} \cdot \varepsilon_{ax}] + (\alpha_s + \zeta_s) \cdot \Delta T \quad 5\text{-}2$$

Here, $\Delta\lambda$ and ΔT represent the wavelength and temperature shift. ε_{ax} is the axial strain (positive for axial tension, negative for axial compression); ε_r is the radial strain; p_{11} and p_{12} are photoelastic coefficients; α_s and ζ_s are thermal expansion coefficients and thermos-optic coefficient respectively.

Assuming that the FBG is stretched or compressed along the axial direction, the strain on the axial and radial directions have the relation as:

$$\varepsilon_{ax} = \Delta L/L \quad 5\text{-}3$$

$$\varepsilon_r = -v_s \cdot \varepsilon_{ax} \quad 5\text{-}4$$

Where L is the length of the FBG; ΔL is the change of length due to the stretch or compression; v_s is a constant named as Poisson's ratio.

By substitute Equation 5-3 and Equation 5-4 to Equation 5-5 , we obtain:

$$\frac{\Delta\lambda}{\lambda_B} = (1 - p_e) \cdot \varepsilon_{ax} + (\alpha_s + \zeta_s) \cdot \Delta T \quad 5\text{-}6$$

$$p_e = \frac{n^2}{2} \cdot [p_{12} - v_s \cdot (p_{11} + p_{12})] \quad 5\text{-}7$$

By substituting the values of the constants p_{11}, p_{12}, v_s, α_s and ζ_s in optical silica fibres, an approximate equation is derived as:

$$\Delta\lambda/\lambda_B \cong 0.78 \cdot \varepsilon_{ax} + 7.5 \times 10^{-6} \cdot \Delta T \quad 5\text{-}8$$

Many designs of tuning setups have been reported based on these equations including those utilising thermal effect [9] and mechanical stress [10-13]. However, the design based on thermal effect shows practical drawbacks, as it can only achieve a small tuning band due to the relatively low influence of temperature [7]. Alternatively, methods based on strain can provide a more significant change in the grating period and thus offer a broader tuning range.

If the temperature maintains constant and the FBG is only subjected to stretching or compression, the resulting wavelength shift $\Delta\lambda$ can be described by the following equation:

$$\Delta\lambda \cong 0.78 \cdot \varepsilon_{ax} \cdot \lambda_B = 0.78 \cdot \frac{\Delta L}{L} \cdot \lambda_B \quad (5\text{-}9)$$

Note that ΔL is positive for tension and negative for compression.

It is important to limit the bending radius or strain applied to the fibre as there is a risk of breakage, which varies depending on the quality of the fibre and its coating materials. It should be noted that silica fibre is generally more robust under compression than tension. As a result, within the damage limit of the FBG, a broader wavelength shift towards the shorter edge can usually be achieved compared to the longer edge.

5.4.2 Experimental setup

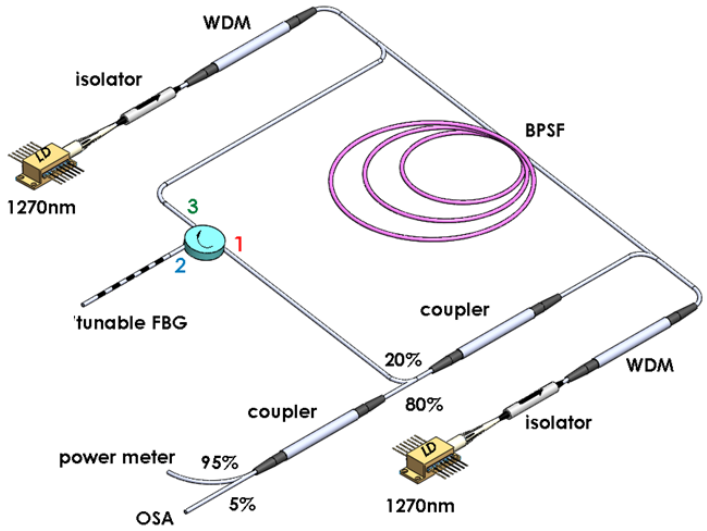

Figure 5.13 Schematic of the tunable BDFL setup based on an FBG.

Figure 5.13 shows a schematic diagram of the tunable laser setup that uses a FBG for tuning. The setup is similar to the wavelength-fixed BDFL depicted in Figure 5.1 (version B), with the only difference being the replacement of the conventional FBG with a mechanically tunable FBG to achieve a wavelength-tunable BDFL. The setup also includes another 95/5 coupler that is used to monitor both the power and spectrum simultaneously.

The FBG was made by Pro. Morten Ibsen in the Optoelectronics Research Centre (ORC), University of Southampton. It was embedded in a 10 cm long relatively soft flexible slab, and then adhered to an elastic beam. This tuning apparatus used a pure arc bending technique to apply a compressive or tensile force to the grating [13], as shown in Figure 5.14. The metal base was manufactured in the workshop of the ORC. As the movable block was translated inwards, a bending of the FBG occurred, resulting in a tunable shift of the Bragg wavelength towards either shorter or longer wavelengths. The bending radius or distance was controlled by a micrometre-screw. In our experiments, only compression was applied to the FBG to prevent any potential damage via stretching.

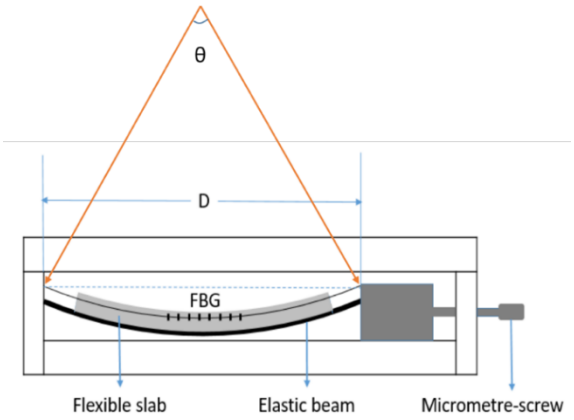

Figure 5.14 The mechanism-based tuning package configuration. This tuning package involves a conventional FBG embedded in a flexible slab and an elastic beam which is held by a metal bracket. The micrometre screw is used to apply the force to the movable metal block and to bend the FBG.

The wavelength shifting of the FBG depends on the strain induced in the fibre, which is a function of the bending radius (R) and the distance of the FBG from the neutral axis of the bending substrate (d). The stain ε_{ax} can be described as:

$$\varepsilon_{ax} = \pm d/R \tag{5-10}$$

When a FBG with length L is bend with a radius of R, the stain it experiences can be described as:

$$R = L/\theta \tag{5-11}$$

Where θ is the central angle of the bending arc which can be calculated from the length of the elastic beam and the displacement of the movable metal block. The arc can be formed either upwards or downwards, responding to tension and compression respectively.

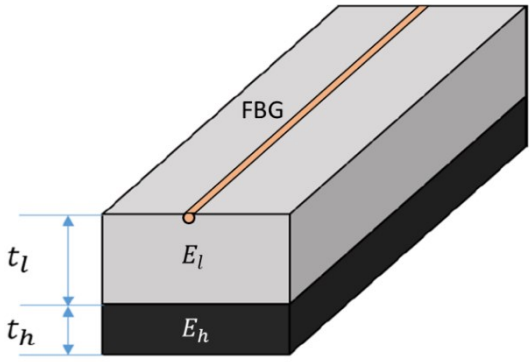

Figure 5.15 Structure of a bending beam with a two-layer material

In this experiment, a soft flexible slab was employed and adhered to an elastic beam, as the effective distance from the FBG to the neutral axis can be enhanced by using a hybrid of layered materials [10], resulting in an increase of the stain ε_{ax} at a limited bending radius. Figure 5.15 provides an example of a two-layer material structure, where the top layer is a soft material with lower Young's modulus E_l and thickness t_l, and the bottom layer is a hard steel with higher Young's modulus E_h and thickness t_h. The effective distance d_{eff} is described by the follow equation:

$$d_{eff} = t_l + \frac{E_h \cdot {t_h}^2 - E_l \cdot {t_l}^2}{2 \cdot (E_h \cdot t_h + E_l \cdot t_l)} \tag{5-12}$$

When bonding two materials, it is important to consider two factors. Firstly, the FBG and the two materials must be firmly and strongly bonded to ensure a complete transfer of the strain from the substrate to the grating. Secondly, the chosen of the soft material is crucial. If the Young's modulus of selected materials is too low, the FBG might suffer from inelastic deformation or axial shear force when a high strain is applied.

Several FBGs were tested with BPSF L10619 and the result is discussed below.

5.4.3 Results and discussion

To begin with, a FBG with a central wavelength of 1340 nm and a reflectivity of 96% was securely bonded to the tuning package, with tuning carried out solely through compression to prevent any potential damage to the FBG. The resulting output power and slope efficiency were measured under a total incident pump power of 720 mW, with measurements taken at various wavelengths. A 25 nm bandwidth from 1340 to 1315 nm was achieved, with a decrement of 5nm from 1340nm. Figure 5.16(a) shows the output power and slope efficiency, while Figure 5.16(b) presents the spectrum at different wavelength, measured with a OSA resolution bandwidth of 0.5 nm.

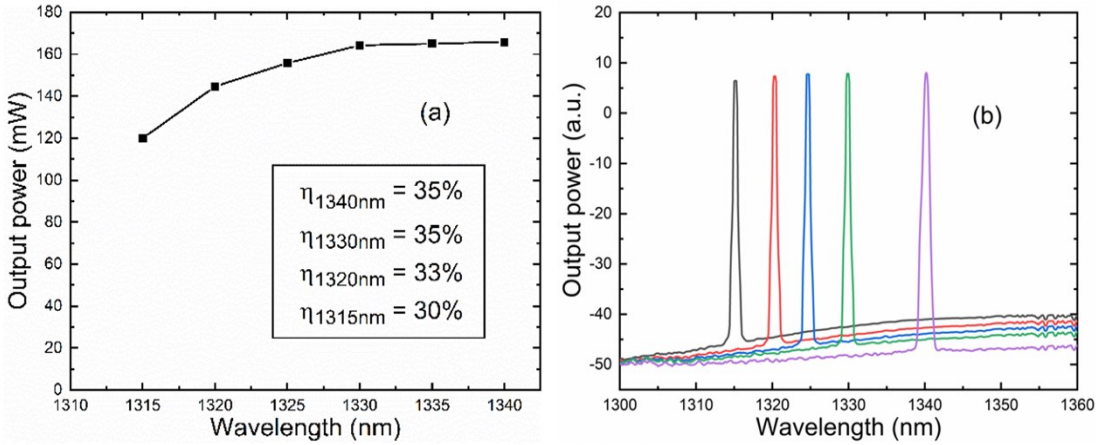

Figure 5.16 (a) Output power of the tunable BDFL at different wavelengths; inset: laser efficiency at different wavelengths (b) Spectrum of the tunable BDFL from 1315-1340 nm measured with 0.5 nm OSA resolution bandwidth.

As shown in Figure 5.16(a), for the wavelength band investigated here, the output power was above 120 mW across the entire 25 nm band with a maximum power of approximately 165 mW at the longest wavelength of 1340 nm. In addition, the laser efficiency was above 30% throughout the 1315-1340 nm operating band. The tuning spectra of the laser shown in Figure 5.16(b) demonstrates an OSNR of ≥50 dB across the full tuning range.

In this demonstration, the tuning range was limited because the original operating wavelength of the FBG was 1340 nm and the FBG was only tuned to shorter wavelengths. However, a wavelength tuning from 1315 nm up to 1375 nm should be expected based on the BPSF gain profile. Therefore, a second FBG with a central wavelength at 1370 nm was used to cover the longer wavelength side of the BPSF gain spectrum. The reflectivity and FWHM of the second FBG was 97% and 0.14 nm, respectively.

Figure 5.17 illustrates the output power of the tunable BDFL with the second FBG, with the maximum power maintained around 165 mW at 1335 nm within a 10 nm bandwidth. The output power exceeded 100 mW in a 50 nm range from 1320-1370 nm, and the laser efficiency was ≥ 25% in this range. The laser efficiency also remained ≥ 30% throughout the 1325-1365 nm operating band, as shown in the inset of Figure 5.17 .

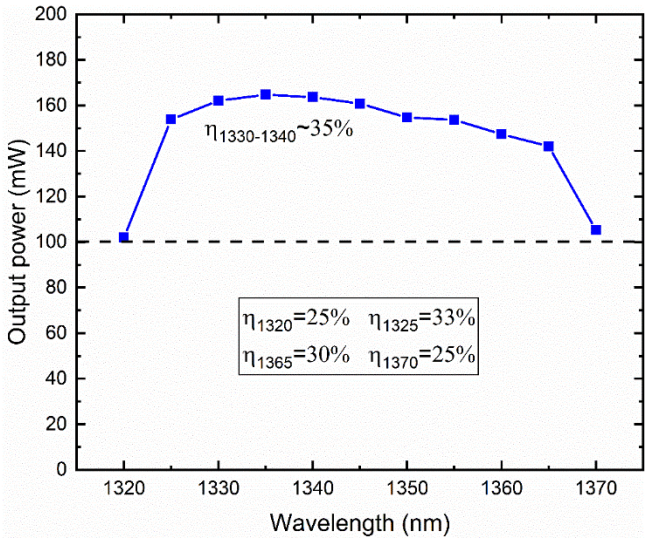

Figure 5.17 Output power of the tunable BDFL under full pump power (720 mW) at different wavelengths from 1320-1370 nm. Dotted line: 100 mW. Inset: laser slope efficiency at different wavelengths

The power drop at the longer wavelength edge was due to the limited gain profile of the BPSF used, while at the shorter wavelength edge it was due to the increased component loss caused by the compressed FBG. If a more widely tuned FBG is applied, the output power at 1320 nm is expected to reach a higher level of 140 mW compared to the case with the first FBG.

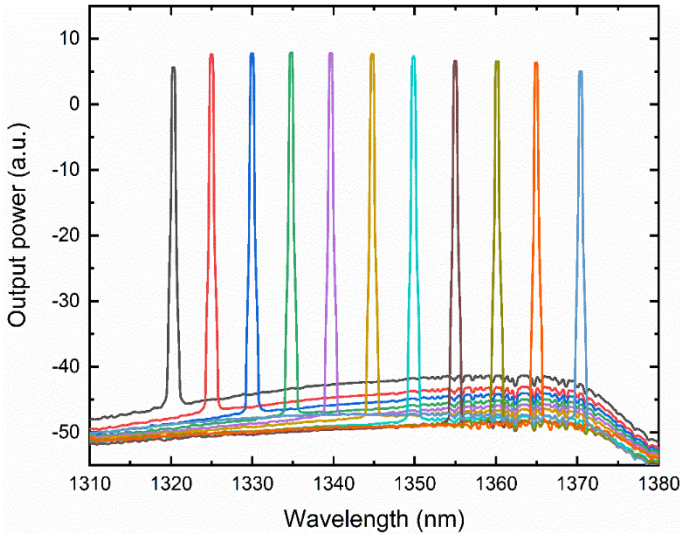

Figure 5.18 Spectrum of the tunable BDFL at different wavelengths from 1320- 1375 nm, measured with 0.5 nm OSA resolution.

The spectrum of the tunable BDFL with the second FBG from 1320-1370 nm is shown in Figure 5.18, measured with an OSA resolution bandwidth of 0.5 nm. The OSNR is ≥50 dB

across the whole 50 nm tuning range. The linewidth of the output signal at 1340 nm was measured to be ~0.04 nm, as presented in Figure 5.19, with an OSA resolution bandwidth of 0.02 nm.

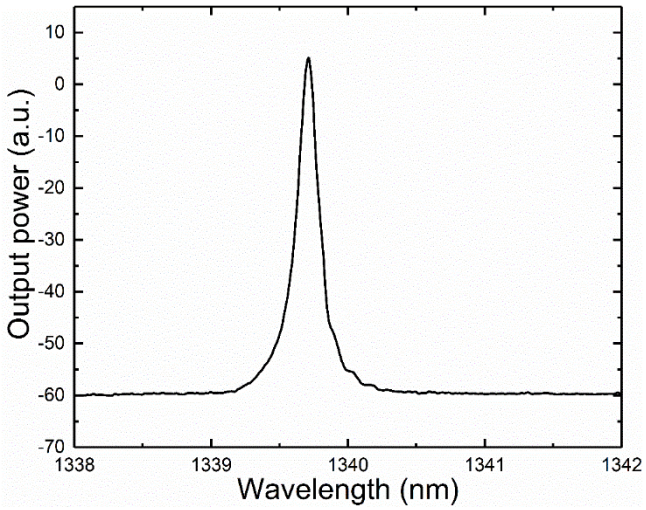

Figure 5.19 Linewidth of the tunable BDFL at 1340 nm, measured with 0.02 nm OSA resolution bandwidth.

In conclusion, by employing two tunable FBGs, a total tuning bandwidth of 55 nm has been demonstrated. With the first FBG at 1340 nm, the BDFL was tuned in a 25 nm range from 1340 nm to 1315 nm with a maximum output power of 165 mW and an OSNR of ≥50 dB. By using a second FBG with an operating wavelength at 1370 nm, the BDFL tuning bandwidth was extended to 50 nm from 1370 nm to 1320 nm, with the same maximum pump power. The output power remained > 100 mW over the whole 50 nm bandwidth. At the wavelength which gave the maximum output power, the slope efficiency of the BDFL was 35%, and maintained ≥30% from 1325 to 1365 nm. To the best of our knowledge, this is the first demonstration of a 50 nm wideband continuously tunable Bi-doped all-fibre laser operating in the 1.3 μm wavelength region by employing wavelength-tunable FBGs.

5.5 MOPA system of the tunable BPSF laser

In a previous publication, a tunable laser source was presented with a MOPA configuration [4]. The system utilised a BDFL as the seed of a BDFA, resulting in an increase in maximum output power from 60 mW to 144 mW at a wavelength of 1350 nm. In this study, we investigated the performance of a similar MOPA system utilizing the tunable BDFL described in Section 5.3.

5.5.1 Experimental setup

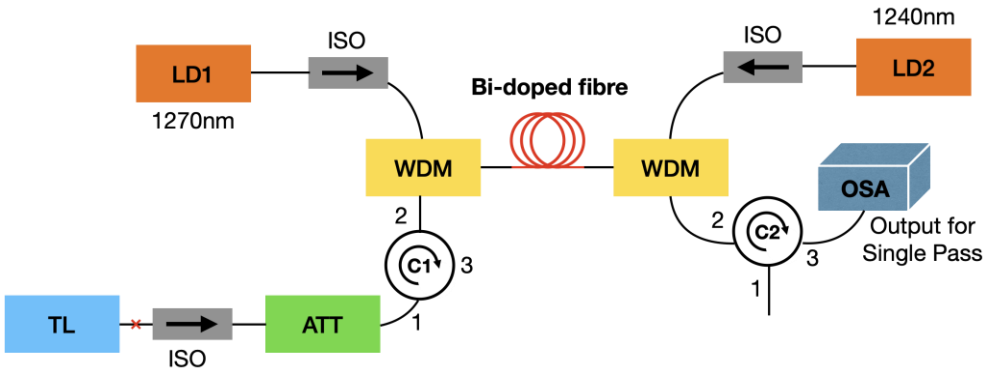

Figure 5.20 Schematic of experimental setup of Bi-doped MOPA laser source. TL: tunable laser; LD: laser diode; ATT: attenuator. C1 and C2: circulators.

The schematic of the Bi-doped MOPA system is depicted in Figure 5.20. The tunable laser (TL) was connected to a BDFA with an isolator to prevent back reflection of the signal. The BDFA included two pump diodes operating at 1270 nm and 1240 nm with a combined power of 800 mW (400 mW from each), each followed by an isolator. Two WDMs were employed to combine the pump light into the BDF and separate the signal. Two circulators (C1 and C2) were used to control the path of the signal in the BDFA. In this study, a single-pass operation of the amplifier was employed, where the signal from the TL was directed from port 1 to port 2 of C1, and the output was monitored at port 3 of C2. In the case of a double-pass operation, the signal would be directed back to the BDF and further amplified by splicing port 3 and port 1 of C2 together. In this configuration the signal should be monitored at port 3 of C1. The length of the BPSF used in this BDFA is 150m.

5.5.2 Results and discussion

The MOPA was initially tested by launching a signal from the TL at 1335 nm with different seed powers of 0, 10, and 20 dBm. The output power from MOPA was then measured by increasing the pump power of the amplifier. Figure 5.21 illustrates a linear increasing trend in the output power in all three cases. The forward pump at 1270nm was first increased to the maximum of 400mW, followed by another 400mW power from the backwards pump at 1240nm. As a result, a slightly different of the slope efficiency was observed at the switch point. When the BDFA operated under full pump power, the maximum output power was

72, 129, and 166 mW (~19, 21, and 22 dBm) for input powers of 0, 10, and 20 dBm, respectively, with a corresponding gain of 19, 11, and 2 dB.

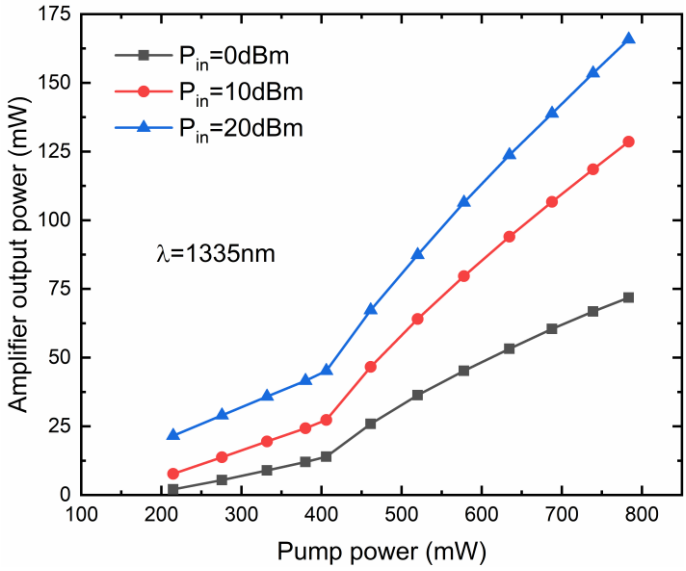

Figure 5.21 Output power of the Bi-doped MOPA under different pump power of the amplifier. The seed power was 0, 10, 20 dBm at 1335nm.

Furthermore, the seed was tuned to five different wavelengths of 1310, 1320, 1335, 1360, and 1370 nm with the power increased from 0 mW to the available maximum value. The BDFA was fully pumped (800 mW). Figure 5.22 shows the variation of the output power from the MOPA with different input power. The curve exhibited a sharp increase at low input power but gradually reached saturation with the seed power over 40 mW. The gain of the BDFA was calculated and presented in Figure 5.23. With the increase of the seed power, the gain decreased significantly until the amplifier was saturated. The output power was higher between 1320-1360 nm and decreased at shorter (1310 nm) and longer (1370 nm) wavelengths, as can be seen from Figure 5.22. Correspondingly, the gain was higher at the central wavelengths than it at the edges, shown in the inset of Figure 5.23.

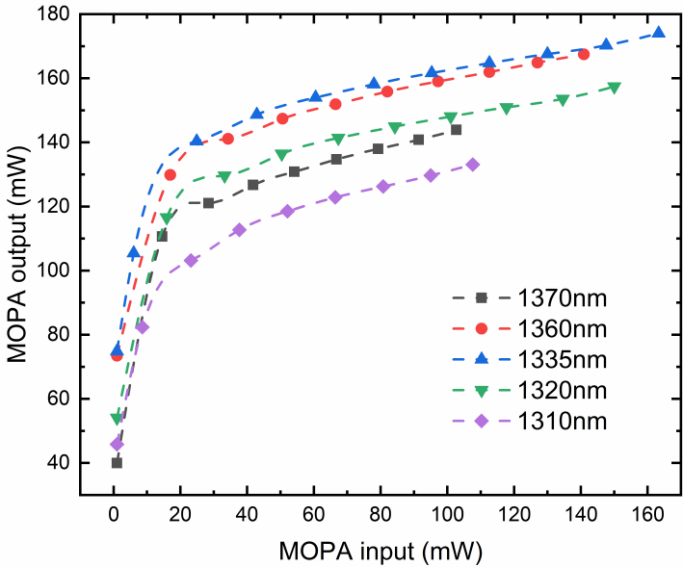

Figure 5.22 Output power of the Bi-doped MOPA with varied seed power at different wavelengths

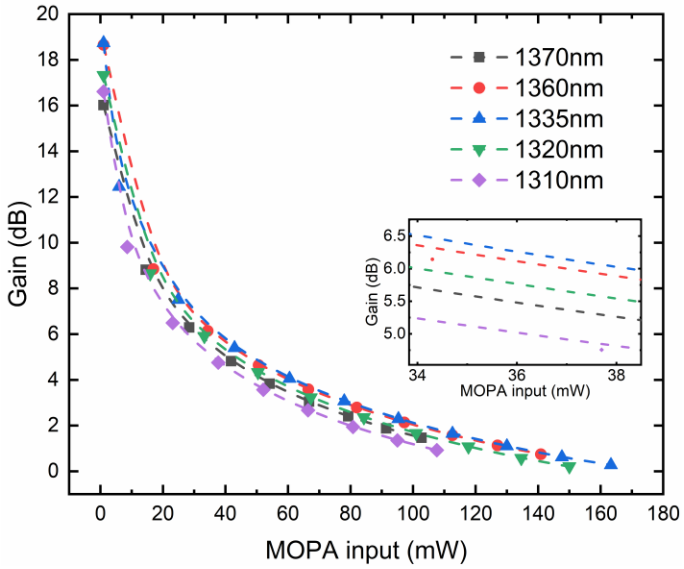

Figure 5.23 Variation of the MOPA gain with the increased seed power at different wavelengths; inset: a zoomed-in view of the point at approximately 36 mW input as an example.

Figure 5.24 compares the maximum output power of the TL and the MOPA system. The output power was also calibrated as the output WDM in the BDFA had a wavelength-dependent loss in the wavelength range of 1300-1375nm. A uniform insertion loss of 0.5dB was considered for the WDM impact. It can be found that the MOPA configuration did not significantly improve the output power when compared to the output power from the TL itself as the input power was already high enough to saturate the amplifier. Even by attenuating the seed power, the MOPA output power remained similar to the maximum

available power from the TL. However, the output power was increased at both shorter and longer wavelength edges with a slightly flatter output profile by considering a flat loss of the WDM in the amplifier. The 3 dB power-drop bandwidth was increased to 72 nm from 1303 to 1375 nm, which was 10 nm broader compared to that without amplification from 1308 to 1370 nm. The output power of the MOPA system exceeded 150 mW in the range of 1315-1365 nm, while it could only be reached within 1320-1355 nm in the TL itself.

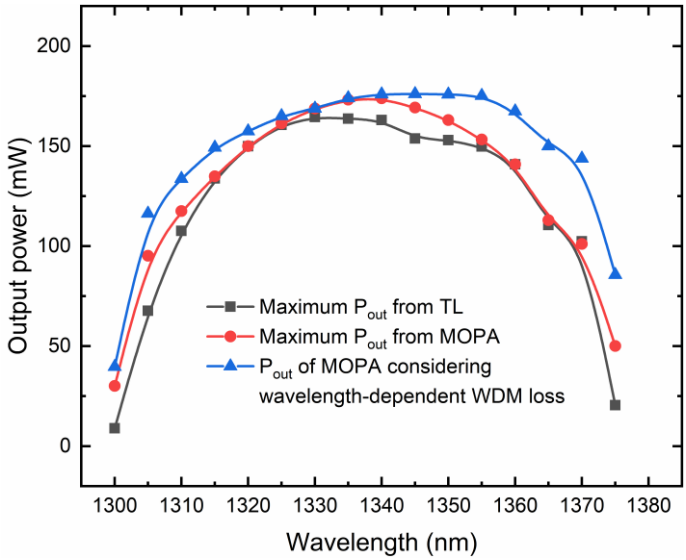

Figure 5.24 Maximum output power of the Bi-doped MOPA laser, compared to the maximum power from the tunable BDFL.

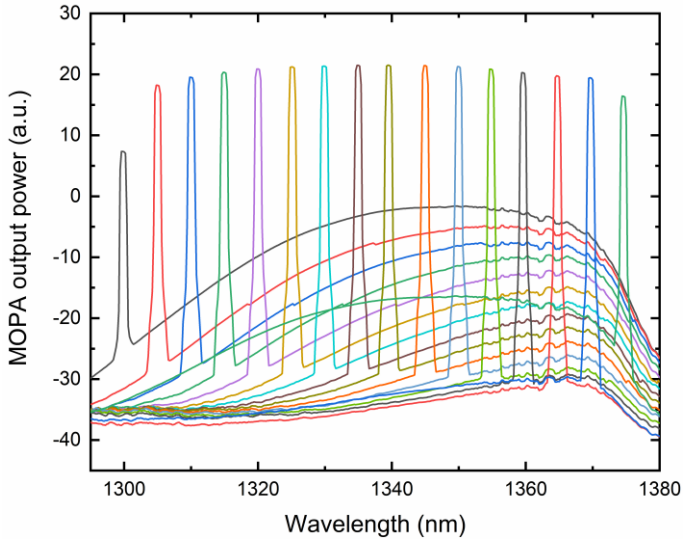

Figure 5.25 Spectrum of the Bi-doped MOPA laser from 1300 to 1375 nm, measured by 0.5 nm OSA resolution bandwidth.

The spectrum of the MOPA output light from 1300 to 1375nm is shown in Figure 5.25, measured with an OSA resolution bandwidth of 0.5 nm. The in-band OSNR remained above

45 dB except at 1300 nm (31 dB) and 1375 nm (40 dB), but the out-of-band OSNR was above 23 dB from 1305 to 1375 nm and only 9 dB at 1300 nm. The OSNR degrade was due to the noise and amplified spontaneous emission (ASE) accumulated in the BDFA.

5.6 Summary

Overall, the study demonstrated the feasibility and potential of BDFLs for various applications. The establishment of CW BDFLs was discussed, including the cavity optimisation of the laser at 1340 nm, and the demonstration of the tunable version with the help of the optical filter and two FBGs. The homemade BPSFs showed their ability to provide a 38% slope efficiency of the laser and more than 160 mW output power at 1340 nm, which is only limited by the pump powers. Lasing at this wavelength is believed to benefit many fields, such as telecommunications, sensing, and biomedical applications. By employing an optical filter in the ring cavity, the laser was tuned from 1315 to 1375 nm, with the slope efficiency remaining above 25% within a 3 dB bandwidth from 1311 to 1371 nm. Moreover, the tunable BDFL with FBGs also showed promising results. By using a hybrid of layered materials to make a compressed-based tunable FBG and carefully selecting the operation wavelength, a 50 nm tuning bandwidth was achieved from 1320 to 1370 nm with output power above 100 mW. A MOPA configuration was utilised to enhance the output of the tunable source. However, the improvement achieved was limited as the BPSFs used in the amplifier were found to be saturated. It was believed that replacing the output WDM in the BDFA with a component that has wavelength-independent loss could potentially result in a broader and flatter output profile. Such an improvement would yield a >70nm bandwidth with a 3dB power drop. The subsequent stage in the development of this MOPA system involves carefully selecting the relevant components. It is crucial to highlight that, a long length of fibre (200m in the tunable BDFL and 150m in the BDFA) was employed in this current system. Therefore, reducing the fibre length in such systems becomes imperative for future advancements.

5.7 Reference

[1] S. Wang, Y. Wang, N. K. Thipparapu, M. Ibsen, D.J. Richardson, and J. K. Sahu, “All-fiber wavelength-tunable Bi-doped laser employing a fiber Bragg grating operating in the

1300nm band," *Conference on Lasers and Electro-Optics Europe (CLEO), OSA Technical Digest (Optical Society of America, 2020)*, paper STh1P.7.

[2] S. Wang, N. K. Thipparapu, Y. Wang, M. Ibsen, D.J. Richardson, and J. K. Sahu, "Widely-tunable Bismuth-doped fiber laser for the 1305-1375nm wavelength range," *OSA Advanced Photonic Congress, Specialty Optical Fibers*, 2020, paper SoM4H.6.

[3] S. Wang, Y. Wang, N. K. Thipparapu, M. Ibsen, D. J. Richardson, and J. K. Sahu, "Tunable CW Bi-doped fiber laser system from 1320 to 1370 nm using a fiber Bragg grating," IEEE Photonics Technology Letters, 32(22), 1443-1446 (2020).

[4] N. K. Thipparapu, S. Wang, A. A. Umnikov, P. Barua, and J. K. Sahu, "All-fiber Bi-doped laser continuously tunable from 1317-1375nm," in *Conference on Lasers and Electro-Optics Europe and European Quantum Electronics Conference, OSA Technical Digest (Optical Society of America, 2019)*, paper cj_12_6.

[5] N. K. Thipparapu, Y. Wang, S. Wang, A. A. Umnikov, P. Barua, and J. K. Sahu, "Bi-doped fiber amplifiers and lasers," *Optical Materials Express*, 9(6), 2446-2465 (2019).

[6] I. A. Bufetov, M. A. Melkumov, V. F. Khopin, S. V. Firstov, A. V. Shubin, O. I. Medvedkov, A. N. Guryanov, and E. M. Dianov, "Efficient Bi-doped fiber lasers and amplifiers for the spectral region 1300-1500 nm," *Proceeding of SPIE* 7580, 758014 (2010)

[7] M.L. Rocha, F. Borin, H.C. Monteiro, M.R. Horiuchi, M.R. de Barros, M.A.D. Santos, F.L. Oliveira, and F.D. Simões, "Mechanical tuning of a fiber Bragg grating for optical networking applications," *Journal of Microwaves*, *Optoelectronics and Electromagnetic Applications*, **4**(1), 1-11 (2005).

[8] S. W. James, M. L. Dockney, and R. P. Tatam, "Simultaneous independent temperature and strain measurement using in-fibre Bragg grating sensors." *Electronics Letters*, **32**(12), 1133-1134 (1996).

[9] L. Li, J. Geng, L. Zhao, G. Chen, G. Chen, Z. Fang, and C. F. Lam, "Response Characteristics of Thin-Film-Heated Tunable Fiber Bragg Gratings," *IEEE Photonics Technology Letters,* **15**(4), 545-547 (2003).

[10] S. G. Chee, Y. S. Sze and K. Kazuro, "Widely Tunable Optical Filters Based on Fiber Bragg Gratings," *IEEE Photonics Technology Letters,* **14**(9), 1306 - 1308 (2002).

[11] C. Goh, S. Set, K. Kikuchi, M. Mokhtar, S. Butler, and M. Ibsen, "Greater than 90nm continuously wavelength-tunable fibre Bragg gratings," In *Optical Fiber Communication Conference*, Optical Society of America, 2003. paper. FC5.

[12] G. Bharathan, R.I. Woodward, M. Ams, D.D. Hudson, S.D. Jackson, and A. Fuerbach, "Direct inscription of Bragg gratings into coated fluoride fibers for widely tunable and robust mid-infrared lasers," *Optics Express*, **25**(24), 30013-30019 (2017).

[13] C. S. Goh, M. R. Mokhtar, S. A. Butler, S. Y. Set, K. Kikuchi and M. Ibsen, "Wavelength tuning of fiber Bragg gratings over 90nm using a simple tuning package," *IEEE Photonics Technology Letters*, **15**(4), 557-559 (2003).

Chapter 6 Development and characterisation of Bi-doped aluminosilicate fibres

6.1 Introduction

In this chapter, the fabrication and characterisation of Bi-doped aluminosilicate fibres (BASFs) is introduced. The spectroscopic characteristics of Bi-doped fibres (BDFs) strongly depend on the surrounding environment of the Bi ion. When the co-doped phosphorous (P) is replaced by aluminium (Al), the fluorescence wavelength shifts from 1.3 μm to 1.1 μm. BASF has potential benefits in both amplifier and laser systems. Although 1.1 μm is not within the low-loss window of traditional optical silicate fibres, there is a growing interest in amplifiers in this wavelength range due to the lower loss achieved in hollow-core fibres [1-3]. With a comparable attenuation of 0.5dB/km in recently developed hollow-core fibres, the 1.1 μm wavelength has potential for use in future optical telecom systems. Additionally, fibre lasers operating at 1.1 μm can be utilised for visible-light generation (by frequency-doubling technique), which is in demand in fields such as astronomy, ophthalmology, and dermatology [4-6].

In Section 6.2 of the chapter, modifications made to the BASF fabrication process are introduced, including the solution content, gas condition, and fibre drawing speed. Refractive index and chemical distribution of the manufactured BASFs were measured and discussed in Section 6.3; absorption spectrum and unsaturable loss measurements were carried out and summarised in Section 6.4. Finally, Section 6.5 concludes the impact of fabrication parameters on BASFs' performance by comparing the characterisation results among different fibres. Other characteristics including fluorescence spectrum, lifetime, and absorption/emission cross-section will be discussed in the next chapter (Chapter 7).

6.2 Fabrication of Bi-doped aluminosilicate fibres

Using the MCVD-solution doping technique described in Chapter 3, a series of BASFs were fabricated. Specifically, a pure Si soot was deposited to an F300 tube under a fixed temperature of 1340 °C, which had been previously optimised during the fabrication of BPSFs. Bi and Al ions were both doped into the glass through the solution. The fabrication

of BASFs was focused on adjusting three factors: solution content, inner atmosphere during tube collapsing and fibre drawing speed.

6.2.1 Effect of solution content and collapse atmosphere

In this work, we used $BiCl_3$ and Al_2O_3 dissolved together in the solution by using either methanol (MetOH) and ethanol (EtOH) as solvents. The two different kinds of solution were both studied in this work.

Table 6.1 and Table 6.2 summarise the BASFs fabricated under different conditions in this study. These tables outline the solution content and concentration, as well as the gas species used during the glass collapse pass. Details on the resulting colour of the preform core and the refractive index difference are also provided for reference.

The first four preforms, L10613-L10616, were prepared using MetOH as the solvent. It should be noted that these preforms were fabricated prior to optimising the soot temperature, meaning the soot was deposited at a temperature higher than 1340 °C. The successful doping of Al ions in the glass was confirmed by the refractive index difference (Δn) of the preforms, leading to the expectation of incorporation of Bi in the core and correspondingly, the absorption in the NIR spectral region. However, when observed through the axis direction, both L10613 and L10614 exhibited a transparent core in the preform, suggesting negligible Bi incorporation. (The relationship between the preform core colour and the deposition concentration is discussed in Section 4.2). The absence of Bi was later confirmed after drawing the fibre from the two preforms, as the NIR absorption was found to be <0.1 dB/m (as presented in Section 6.4). This result suggested that Bi ions may not have been deposited along with Al ions, despite being dissolved in the same MetOH solution, possibly due to the evaporation of Bi during oxidation and collapsing passes. Therefore, it is necessary to modify the fabrication conditions to enhance the absorption at 1.1 μm. A preliminary experiment was carried out by replace oxygen (O_2) with helium (He) during the tube collapsing pass of L10615 and L10616, completely or partially, respectively. The preform core began to exhibit pink/red colours, indicating an increase in the Bi incorporation or change of Bi state when He was used.

Table 6.1 List of fabricated BASFs using methanol solution.

Dopants /Host	Preform No.	Fibre No.	Solution			Gas during collapsing pass	Colour of the preform core	Core/Cladding diameter(μm)	Refractive index difference (Δn)
			$BiCl_3$ concentration (gm/100mL)	Al_2O_3 concentration (gm/100mL)	Solvent				
Bi+Al/Si	L10613	A1306	0.04	20	MetOH	O_2	Clear	14/100	0.004
	L10614	A1318	0.08	20		O_2	Clear	14/100	0.007
	L10615	A1322	0.6	20		He	Dark red	15/100	0.007
	L10616	A1324	0.6	20		50%He:50%O_2	Light pink	14/100	0.007

Table 6.2 List of fabricated BASFs using ethanol solution.

Dopants /Host	Preform No.	Fibre No.	Solution			Gas during collapsing pass	Colour of the preform core	Core/Cladding diameter(μm)	Refractive index difference (Δn)
			$BiCl_3$ concentration (gm/100mL)	Al_2O_3 concentration (gm/100mL)	Solvent				
Bi+Al/Si	L10718	A1668	0.08	20	EtOH	O_2	Clear	14/100	0.013
	L10723	A1672	0.08	20		He	Pink	14/100	0.013
	L10730	A1680	0.08	10		He	Pink	13/100	0.006
	L10732	A1689	0.08	10		75%He 25%O_2	Clear	13/100	0.006
	L10734	A1692	0.08	10		90%He 10%O_2	Light yellow	13.5/100	0.006

The subsequent set of preforms, L10718-L10734, were fabricated using ethanol as the solvent. The decision to use a Bi concentration of 0.04 g/100 mL in the solution was based on the successful performance of BPSFs prepared by a solution with the same Bi concentration. However, similar to preforms L10613 and L10614, a transparent core was observed in the preform L10715. In an attempt to increase the Bi incorporation, the Bi concentration in the solution was doubled to 0.08 g/100 mL for the subsequent preform L10718. However, no colour change was observed. Comparison of preforms L10613, L10614, and L10718, along with the absorption of the corresponding fibres, revealed no noticeable difference between the use of MetOH and EtOH solvents.

Similar to L10615 and L10616, experiments were conducted on preforms L10730, L10732 and L10734 to substitute different He/O_2 ratios during the collapse pass. The gas flow during fabrication can influence the fibre performance in many cases. In our previous work on BPSFs, a significant impact on the absorption spectrum was found when He was completely replaced with O_2, with the absorption peak shifted and eventually disappeared [7]. In some Ge-doped fibres (no Bi-doped), a reducing atmosphere enhanced the photosensitivity of the fibre and increased the fibre absorption [8, 9]. Thus, it is crucial to study the impact of the gas atmosphere during the collapse pass to increase the incorporation of Bi ions in the glass and to improve the fibre absorption at the desired wavelength.

Table 6.3 presents typical preform collapse parameters used in our fabrication process (not for BASFs fabrication). The burner was set at a temperature of approximately 1900 °C and moved in a forward direction on the MCVD lathe at a speed of 40-90 m/min depending on the inner diameter of the tube. This pass could be repeated for two or three times if the diameter was not small enough for the final sealing pass. Throughout the experiment in this study, the burner speed and the temperature remained constant, while the gas flows were varied by adjusting the ratio of He to O_2 in the total gas volume. Specifically, L10615 was prepared using 100% He, while L10616 was fabricated using a mixture of 50% He and 50% O_2, both using the same MetOH solution. Similarly, L10718, L10730, L10732, and L10734, were made with varying ratios of He gas (0%, 100%, 75% and 90% separately).

The absorption spectra of these fibres are presented in Figure 6.1, which reveal a significant decrease in absorption at 1.1 µm with an increase in the O_2 ratio (or the decrease in the He

ratio). The lengths of the fibres used in the absorption measurements were determined based on the absorption values at 1-1.1 µm. The absorption values of L10616 at 0.8 µm and 1.4 µm were not resolved in Figure 6.1 because a 200 m fibre was used. In addition, Figure 6.2 provides a comparison for the absorption at 1120 nm for fibres L10718, L10730, L10732, and L10734. The results clearly indicate that replacing O_2 completely with He gas enhanced the absorption by over ten-fold, from 0.06 to 0.67 dB/m, and from 0.04 to 0.4 dB/m in Figure 6.1, measured at 1120 nm (details in Section 6.4). However, even with as little as 10% O_2 during the collapsing pass, Bi incorporation in the glass was ineffective, and no absorption at 1.1 µm was observed.

Table 6.3 Typical collapse log

The log is for general MCVD fabrication but was not used in this study. In case of BASFs fabrication, the He flow was applied and the O_2 flow was adjusted correspondingly.

Collapse pass number	Flow(cm^3/min)		Burner speed(mm/min)	Temperature(°C)
	O_2	He		
1	500	/	90	1850
2	400	/	60	1900
3	300	/	40	1900

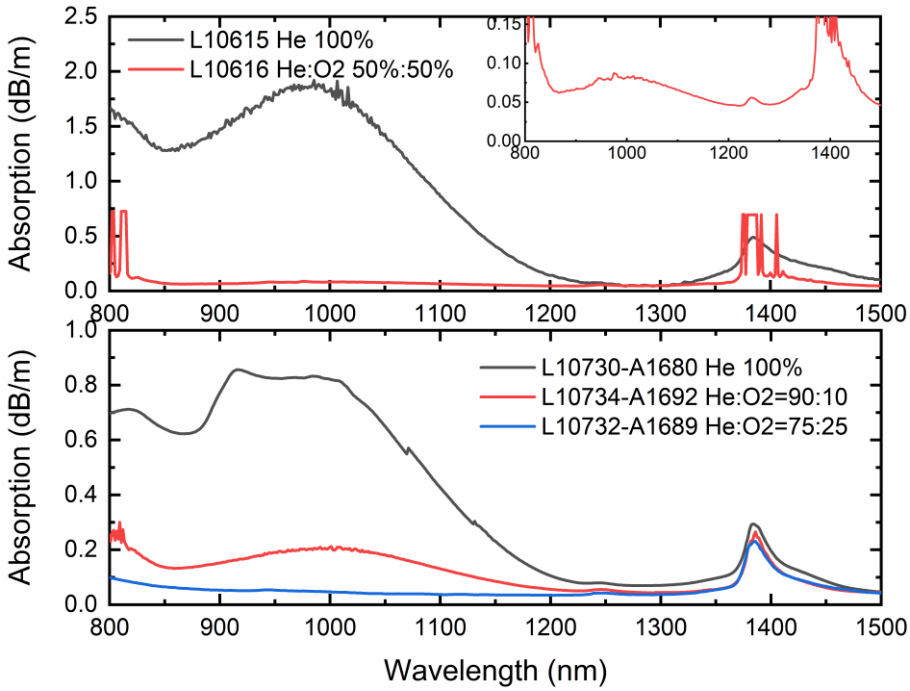

Figure 6.1 Absorption of BASFs fabricated under different gas conditions. Up: L10615 and L10616; Down: L10730, L10732 and

L10734. Inset: Magnified view of the absorption spectrum of L10615.

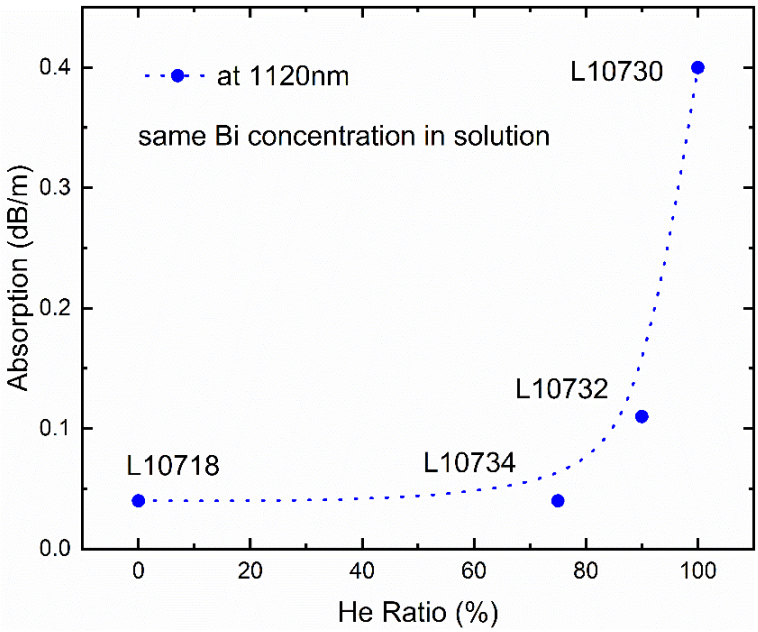

Figure 6.2 Comparison of the absorption of BASF L10718, L10730, L10734, and L10732, which were fabricated with different ratio of He gas at the collapsing stage. A dotted line is given for guidance purpose.

The underlying cause of the distinctions observed among these BASFs is under investigation. Two primary hypotheses are: 1) The utilisation of either O2 or He gas is conjectured to yield different degrees of Bi evaporation during the heating and subsequent processes; 2) O2 and He gases might have an influence on the oxidation state of the incorporated Bi within the glass matrix, consequently engendering variable concentrations of the 'right' Bi ions that contribute to NIR absorption.

The quantification of the overall Bi concentration within the fibre would considerably benefit from techniques such as SIMS and EPMA. However, the concentration in our current fibres is proximate to the analysis threshold and cannot indicate the difference accurately. It is recommended that some reference preforms can be fabricated, for instance, using of a high-Al-concentration solution (as well as varying the gas ratio). It could ensure that chemical analysis methods yield relatively accurate results, no matter the performance of the fibre is desired or not.

6.2.2 Effect of fibre drawing speed

The fabrication of BDFs is significantly affected by the fibre drawing speed, which has a notable impact on various aspects such as temperature distribution and cooling rate of the fibre. Alongside the preform manufacturing parameters discussed above including soot deposition temperature, solution composition and gas atmosphere, further investigation into the impact of fibre drawing on the properties of BDFs is crucial. Previous studies have demonstrated that an increase in drawing speed (from 10m/min to 70m/min) resulted in a decrease of unsaturable loss (UL) in BPSFs [10]. In this study, the corresponding effect in BASFs was also investigated.

In this investigation, a series of preforms were utilised to draw fibres at different speeds, ranging from 10m/min to 40m/min. The drawing speed in this experiment was limited by the size and uniformity of the preforms (refractive index variation along the preform length), as well as the height of the drawing tower. The absorption and UL values of the resulting fibres at 1047 nm and 1120 nm are documented in Table 6.4, with the fibres being identified by their unique fibre numbers. In addition, the core and cladding diameters and the refractive index difference are provided for reference purposes.

Table 6.4 List of BASFs drawn at different speeds.

Preform No.	Fibre No.	Draw speed (m/min)	D_{Core}/D_{Clad} (μm)	dn (Δn)	Absorption(dB/m)		UL(%)	
					1047nm	1120nm	1047nm	1120nm
L10615	A1322	10	15/100	0.007	1.44	0.67	68	50
	A1534	40			1.39	0.67	55	40
L10723	A1672	10	14/100	0.013	0.42	0.26	72	59
	A1676-1	30			1.2	0.64	68	55
	A1676-2	40			0.91	0.45	65	51
L10730	A1680	10	13/100	0.006	0.66	0.33	61	43
	A1681	30			0.76	0.33	61	44
L10732	A1689	10	13/100	0.006	0.040	0.038	*	
	A1690	40			0.053	0.055	*	

*UL not measured due to the low absorption within the error range

Figure 6.3(a) depicts the UL variation of BASFs drawn from preforms L10615 and L10723. It is observed that, in these fibres, an increase in the drawing speed leads to a decrease in UL

at both wavelengths of 1047nm and 1120nm. However, for fibres A1680 and A1681 drawn from L10730, there was no variation in UL with the change in drawing speed. It should be noted that the absorption of L10732-A1689/A1690 at the saturated state was too low to be accurately measured using our UL setup; therefore, the UL values for these fibres were not reported.

The absorption spectrum of fibres drawn from L10723, L10615, and L10732 is plotted in Figure 6.3 (b, c, d). Fibres L10730-A1680 and L10730-A1681 exhibited no significant differences in their absorption spectra, and hence were not included in the figure. Notably, no consistent trends were observed across the measured spectra. For instance, the absorption of fibres L10615-A1322/1534 decreased at around 1.1 μm when the drawing speed increased, whereas the trend was reverse for fibres L10732-A1689/A1690. Additionally, when the fibre drawing speed was increased at smaller intervals (10 m/min to 30 m/min, and then to 40 m/min), the absorption exhibited an initial increase followed by a subsequent decrease as the drawing speed was increased, which can be found among L10723-A1672, A1676-1 and A1676-2.

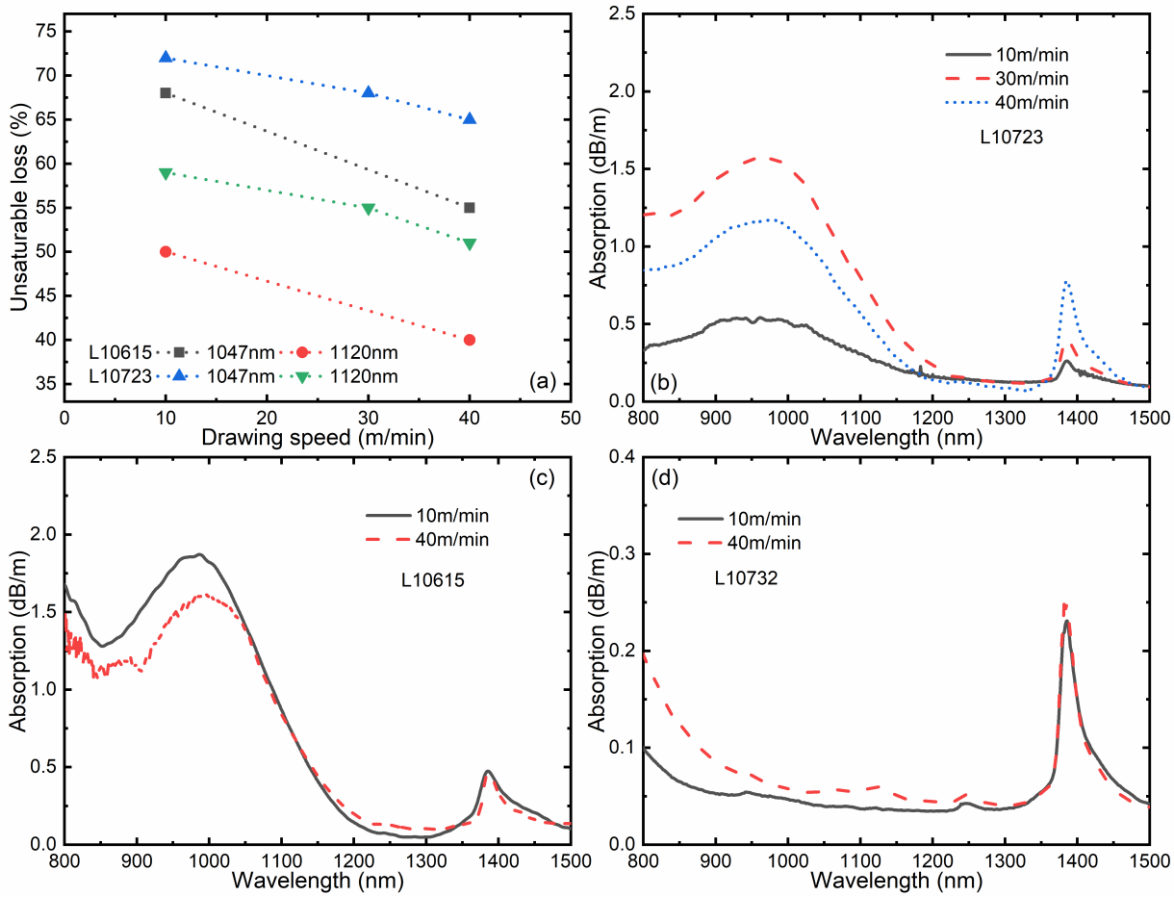

Figure 6.3 UL and absorption of BASFs drawn at different speeds.

According to the findings of BPSFs reported in [10], an increase in the drawing speed resulted in a reduction in the UL, while the absorption decreased to a minimum value before increasing again. Khegai et al. suggested that a certain time was required to form Bi centres that were responsible for UL and NIR absorption and this duration of time when the fibre stayed in the furnace can impact the formation of such centres. As the drawing speed increased, the time that the Bi-doped preform spent in the heating zone of the furnace was effectively reduced. However, this explanation fails to account for the results obtained in our case of BPSFs discussed in [12], where one BPSF sample exhibited a reverse trend and both the UL and absorption increased with a higher drawing speed. In this study of BASF, a similar trend in [10] of increased speed leading to decreased UL was observed in two series samples, L10615-A1322/A1534 and L10723-A1672/1676-1/1676-2, but with fibres L10730-A1680/1681, the absorption of the three fibres did not exhibit a consistent pattern. The reason for this exception is still unclear and requires further investigation.

Given the limited number of samples, it is conjectured that the cooling rate of the glass may play a crucial role in determining the performance of BASFs instead of the duration of the fibre in the hot zone of the furnace. An optimum drawing speed may balance the formation of different species of Bi centres. As preforms L10615 and L10732 were only drawn at two drawing speeds, a comprehensive trend could not be established and explained. To achieve this, it is necessary to draw fibres at more finely spaced speeds.

The optimisation of fibre drawing speed represents a promising method for improving BDFs' performance, but the underlying physical mechanisms remain under investigation. The current study could not provide a convincing conclusion due to the limit of time and samples. More studies are needed to fully understand the relationship between the fibre drawing speed and the fibre performance.

6.3 EPMA in Bi-doped aluminosilicate fibres

Electron probe microanalysis (EPMA) analysis was carried out to measure the concentration of Bi and Al in the fibre core. Figure 6.4. shows the ion distribution of fibres L10718-A1668 and L10734-A1692, with Bi concentration magnified by a factor of 100 for clarity. The distribution of Al ions follows the shape of the refractive index profile of the preform and the fibres (as shown in section3.3, Figure 3.6). In contrast, the disposition of

measured Bi ions appears less clearly defined due to their relatively low concentration. Nevertheless, a discernible central depression can be observed, which is similar to the EPMA result of BPSF (Figure 4.3), as the Bi evaporation during the collapse and sintering process. In the case of L10734, which has a lower Bi concentration than other fibres, the measured distribution of Bi ions is mainly due to the noise of the equipment rather than the real deposition in the core or the cladding. Table 6.5 summarised the measured concentration of Bi_2O_3 and Al_2O_3, and the refractive index difference (Δn) for BASFs. However, the concentration of Bi in these fibres was closed to the sensitivity limit, thus the variation among different BASFs could not be distinguished. The Bi ion concentration is approximately 0.002 mol%.

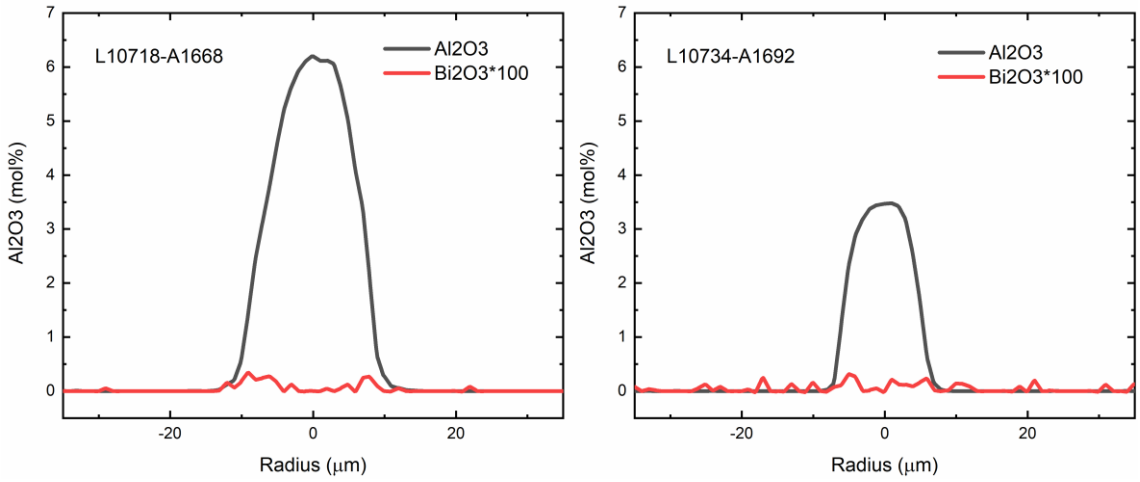

Figure 6.4 Radial distribution in mol% of Al and B determined by EPMA. (Bi concentration is magnified by a factor of 100)

Table 6.5 EPMA results for BASFs

(The concentration of Bi presented here represents an average across the core area, whereas the Al results in the table correspond to peak values)

Analysis	Preform No.	Fibre No.	Bi_2O_3 (mol%)	Al_2O_3 (mol%)	Δn
EPMA	L10718	A1668	~0.002	6.20	0.013
	L10723	A1672		6.49	0.013
		A1676-1		5.98	
	L10730	A1680		2.80	0.006
	L10734	A1692		3.47	0.006

6.4 Absorption and unsaturable loss of BASFs

A detailed analysis of the absorption and UL characteristics of the BASF has been carried out. Figure 6.5 presents the absorption of a typical BASF measured with a OSA resolution bandwidth of 10 nm. To ensure accurate results at different wavelength regions, various fibre lengths were utilised and marked with different colours in the corresponding plot. Inset of the figure is a magnified view of the spectrum in the range of 800-1000 nm. The results demonstrate that the BASF exhibits high absorption at approximately 500 nm and 700 nm, and broad absorption at approximately 1 µm with a bandwidth of 300 mm. The three peaks are believed to come from Bi-Al active centres (BAC-Al), while the peak around 830 nm is the result of Bi-Si active centres (BAC-Si).

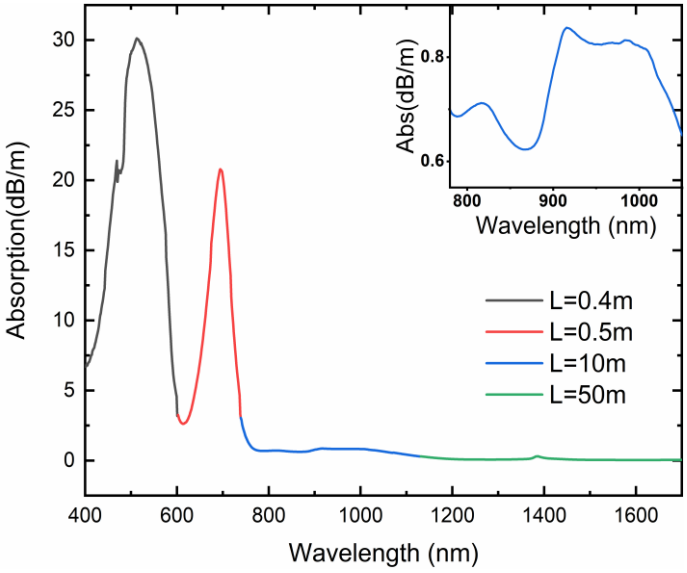

Figure 6.5 Typical absorption of the BASF, measured with 10 nm resolution bandwidth. Inset: magnified view of the absorption spectrum from 800-1000 nm.

The unsaturable loss was measured at 1047 nm and 1120 nm as the fibres were pumped at the two wavelengths in the subsequent study of the BASF laser. Figure 6.6 shows an example of the UL result for a BASF with a relatively short length of approximately 1-2 m, and a pump power ranging from -25 dBm to over 25 dBm. Notably, the results demonstrate a higher UL at 1047 nm compared to that at 1120 nm, which can be attributed to the higher absorption observed at 1047 nm. The detailed absorption and UL results for the BASFs are provided in Table 6.6.

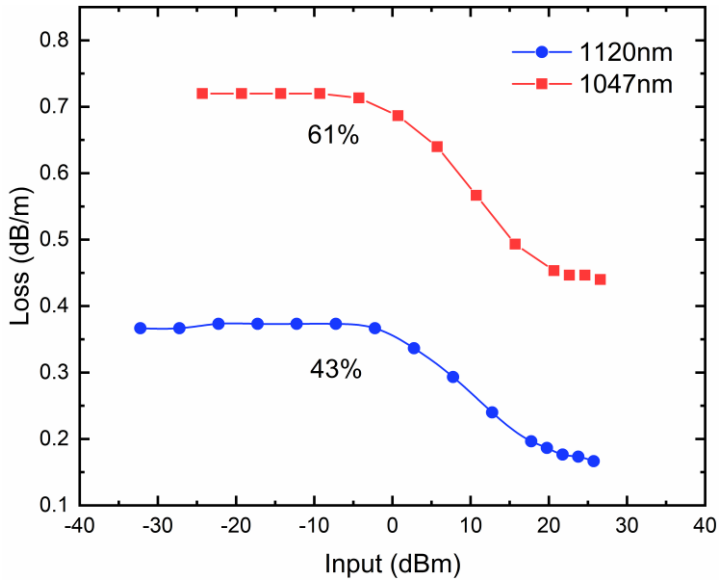

Figure 6.6 UL of a typical BASF, measured at 1047nm and 1120nm, respectively.

Table 6.6 Absorption and UL of different BASFs

'Flat' is used when the low fibre absorption prevents distinguishing between unsaturable and saturable states.

Preform No.	Fibre No.	Absorption(dB/m)		Background loss at 1550nm(dB/m)	OH (ppm)	Unsturable loss (%)	
		1047nm	1120nm			1047nm	1120nm
L10613	A1306	0.06	0.04	0.03	3	Flat	Flat
L10614	A1318	0.05	0.04	0.04	3	Flat	Flat
L10615	A1322	1.44	0.67	0.04	9	68	55
	A1534	1.39	0.67	0.04	7	50	41
L10616	A1324	0.08	0.06	0.04	3.4	Flat	Flat
L10718	A1668	0.06	0.06	0.06	7	Flat	Flat
L10723	A1672	0.42	0.26	0.09	4.5	72	59
	A1676-1	1.20	0.6	0.08	5.5	68	55
	A1676-2	0.91	0.44	0.06	11	65	51
L10730	A1680	0.70	0.33	0.07	4	61	43
	A1681	0.76	0.33	0.04	4.4	62	44
L10732	A1689	0.04	0.04	0.04	3.8	Flat	Flat
	A1690	0.05	0.05	0.04	4	Flat	Flat
L10734	A1692	0.18	0.11	0.04	4.4	47	44

6.5 Conclusion

This chapter discusses the impact of various fabrication parameters on the performance of BASFs. The incorporation of ions is found to be dependent on the gas types and ratio utilised during the collapsing pass. In particular, when He is the dominant gas at a level of >90%, the NIR absorption attributed to the Bi ion see a dramatic increase. Conversely, when O_2 is the primary gas, a reduction of the absorption is noticed, indicating lower Bi ion incorporation, and suggesting either differing oxidation states of Bi ions in the glass or Bi evaporation during the hot passes. Furthermore, during the fibre drawing process, an increase in drawing speed from 10m/min to 40m/min was observed to reduce the UL of BASFs by approximately 10%, though this effect is not universal. Further investigation is required to develop a more comprehensive understanding of the underlying physical mechanisms. The chapter concludes with a comprehensive assessment of the fibre performance through the provision of detailed data on the absorption and UL characteristics of home-made BASFs.

6.6 Reference

[1] H. Sakr, G.T. Jasion, T.D. Bradley, Y. Chen, J.R. Hayes, I.A. Davidson, H.C. Mulvad, L. Xu, D.J. Richardson, and F. Poletti, 2019, June. “Record low loss hollow core fiber for the 1µm region”. In *The European Conference on Lasers and Electro-Optics* (p. ce_5_5). Optical Society of America.

[2] H. Sakr, Y. Chen, T.D. Bradley, G.T. Jasion, J.R. Hayes, I.A. Davidson, E.N. Fokoua, N.V. Wheeler, D.J. Richardson and F. Poletti, 2020, July. “Advances in hollow core fiber for the 1µm and visible wavelength regions”. In *Specialty Optical Fibers* (pp. SoW1H-5). Optica Publishing Group.

[3] H. Sakr, Y. Chen, G.T. Jasion, T.D. Bradley, J.R. Hayes, H.C.H. Mulvad, I.A. Davidson, E. Numkam Fokoua, and F. Poletti, “Hollow core optical fibres with comparable attenuation to silica fibres between 600 and 1100 nm”. *Nature communications*, 11(1), pp.1-10(2020).

[4] C. E. Max, S. S. Olivier, H. W. Friedman, J. An, K. Avicola, B. V. Beeman, H. D. Bissinger, J. M. Brase, G. V. Erbert, D. T. Gavel et al., “Image improvement from a sodium-layer laser guide star adaptive optics system,” Science, 277(5332),1649-1652 (1997).

[5] C. F. Blodi, S. R. Russell, J. S. Pulido, and J. C. Folk, “Direct and feeder vessel photocoagulation of retinal angiomas with dye yellow laser," *Ophthalmology*, 97(6), 791-797 (1990).

[6] N. S. Sadick and R. Weiss, “The utilization of a new yellow light laser (578nm) for the treatment of class I red telangiectasia of the lower extremities,” *Dermatologic surgery*, 28(1), 21-25 (2002).

[7] N. K. Thipparapu, 2017, “Development of Bi-doped Fibre Amplifiers and Lasers & Broadband Er-doped Multi-Element Fibre Amplifiers”, PhD thesis, University Of Southampton, Southampton

[8] D. L. Williams, B. J. Ainslie, J. R. Armitage, and R. Kashyap. “Enhanced photosensitivity in germania doped silica fibres for future optical network.” In 18th European Conference on Optical Communication, Berlin. 1992.

[9] L. Dong, J. Pinkstone, P. St J. Russell, and David N. Payne. “Ultraviolet absorption in modified chemical vapor deposition preforms.” JOSA B 11, no. 10 (1994): 2106-2111.

[10] A. Khegai, F. Afanasiev, Y. Ososkov, K. Riumkin, V. Khopin, A. Lobanov, M. Yashkov, E. Firstova, A. Abramov, M. Melkumov, and A. Guryanov. “The influence of the MCVD process parameters on the optical properties of bismuth-doped phosphosilicate fibers”. *Journal of Lightwave Technology*, **38**(21), 6114-6120 (2020)

[11] S. Firstov, A. Levchenko, A. Kharakhordin, A. Khegai, S. Alyshev, M. Melkumov, V. Khopin, A. Lobanov, and A. Guryanov, “Effect of Drawing Conditions on Optical Properties of Bismuth-Doped High-GeO_2–SiO_2 Fibers.” *IEEE Photonics Technology Letters*, **32**(15), 913-916 (2020).

[12] Y. Wang, “The study of bismuth doped fibres and the development of broadband bismuth doped fibre amplifiers”, PhD thesis, 2023, University of Southampton, UK

Chapter 7 Spectroscopic study and analysis of Bi-doped aluminosilicate fibres

7.1 Introduction

This chapter presents a detailed spectroscopic investigation of Bi-doped aluminosilicate fibres (BASFs), including fluorescence spectrum, lifetime, and cross-sections. This study is of vital importance as the underlying physics of the Bi-doped active centres (BACs) responsible for the near-infrared (NIR) emission remains ambiguous. Section 7.2 and Section 7.3 describe the measurements of the fluorescence spectrum and the lifetime of BASFs, respectively. Section 7.4 analyses the absorption and emission cross-sections of BASFs. Section 7.5 presents an important observation of a distinctive visible emission in the BASF, which is believed to significantly impact the fibre efficiency. Finally, a conclusion of the entire spectroscopic study is provided in Section 7.6.

7.2 Fluorescence spectrum of Bi-doped aluminosilicate fibres

The fluorescence spectrum of the BASFs was measured using the setup shown in Figure 7.1. The fibres were pumped at 1047 and 1120 nm, in preparation for future laser performance studies. An isolator was applied to prevent any damage due to light back-reflection. To collect the fluorescence output from the BASFs, the coatings of the BASFs were removed, and a double-cladded fibre with high numerical aperture (NA) was utilised for capturing of fluorescence light. The length of BASFs was maintained at approximately 2m to prevent any generation of amplified spontaneous emission (ASE). To increase the intensity of the collected light, each tested fibre was coiled in loops, while ensuring that the circle was not too small in order to avoid any pump source leakage from the fibre.

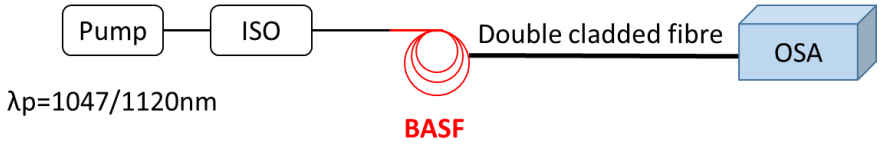

Figure 7.1 Experimental setup of BASFs fluorescence spectrum measurement. ISO: isolator.

Figure 7.2 displays the spectrum of three tested BASFs measured with an OSA resolution bandwidth of 2 nm. The black dotted line corresponds to the 1047 nm pump, while the red dotted line corresponds to the 1120 nm pump. The central wavelength and full-width-at-half-maximum (FWHM) values for each spectrum are provided in Table 7.1.

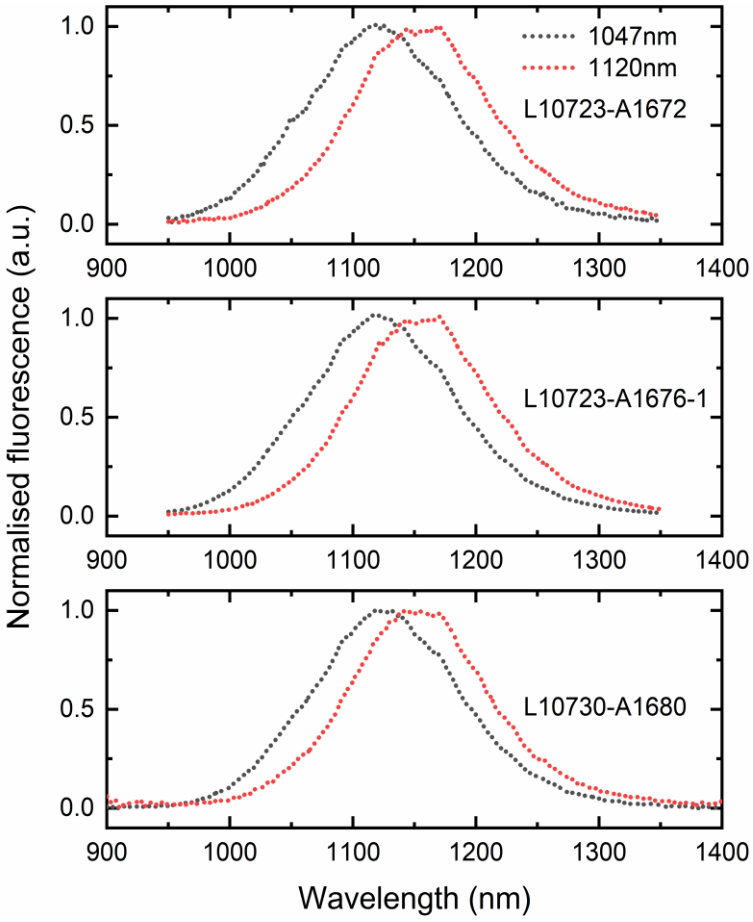

Figure 7.2 Fluorescence spectrum of different BASFs pumped at 1047 and 1120 nm. Black dotted line: 1047 nm pump; red dotted line: 1120 nm pump

Table 7.1 Fluorescence spectrum details of BASFs

Preform No.	Fibre No.	Pump at 1047nm		Pump at 1120nm	
		central λ (nm)	FWHM (nm)	central λ (nm)	FWHM (nm)
L10723	A1672	1120	145	1156	133
L10723	A1676-1	1121	142	1156	133
L10730	A1680	1126	140	1152	129

One notable observation is the dependence of the BASFs fluorescence spectrum on the pump wavelength. When pumped at 1047 nm, the fluorescence peaks were observed at 1120-1126 nm with a FWHM of 140-145 nm, while by pumping at 1120 nm, the peaks shifted to at 1152-1156 nm with an FWHM bandwidth of approximately 130 nm. A 70 nm

difference in the pump wavelength resulted in a 30 nm shift in the fluorescence spectrum. The broad fluorescence bandwidth and the pump-wavelength dependence are the two distinguishing features of BASFs. A similar characteristic was also observed in Bi-doped phosphosilicate fibres (BPSFs) [1, 2].

7.3 Fluorescence lifetime measurement

7.3.1 Principle and review of the lifetime in Bi-doped glass and optical fibres

Fluorescence lifetime is a fundamental parameter in spectroscopy and refers to the characteristic time associated with the decay of the population of ions at excited states in a gain medium. In a typical laser or amplifier gain medium, excited ions at the upper level of the energy transition relax to the lower level through spontaneous emission, stimulated emission, or additional quenching effects. The population of the excited ions decays exponentially with a particular decay time, known as fluorescence lifetime or the upper-level lifetime. Mathematically, the lifetime corresponds to the period required for the population of the metastable ions to reduce to 1/e of its original value, which can be expressed as:

$$\frac{n(t)}{n(0)} = e^{-t/\tau} \qquad 7\text{-}1$$

If non-radiative effects are negligible, the fluorescence lifetime is equivalent to the radiative lifetime. Under the ideal assumption that stimulated emission does not occur, the decay time is determined by spontaneous emission and can be expressed as follows:

$$\frac{1}{\tau} = \frac{8\pi n^2}{c^2} \int v^2 \sigma_{em}(v)\, dv = 8\pi n^2 c \int \frac{\sigma_{em}(\lambda)}{\lambda} d\lambda \qquad 7\text{-}2$$

It is worth noting that the application of the lifetime assumption makes the equations comparatively less precise for a majority of fibres except for Er-doped fibres.

Table 7.2 summarises the previously reported lifetime measurement related to Bi in glass or fibres. The fluorescence lifetime of Bi-doped glasses ranges from 200-500 μs [3-7], while in optical fibres, it is mainly measured to be between 600-1000 μs in the NIR region [8-14]. However, a BDF co-doped with Al and Ge exhibited a shorter lifetime of 360 μs at NIR fluorescence with two distinct peaks at 1250 and 1650 nm, pumped at 976 nm. In the same

study, the lifetime in the visible red region was reported with 3.6 μs for both Bi fibres co-doped with Ge and Ge/Al, pumped at 510 nm [13]. The lifetime is significantly influenced by the doping concentration of both Bi ions, with a shorter lifetime observed at higher Bi concentrations due to quenching effects [15]. Additionally, the lifetime is pump-wavelength-dependent, with a lifetime of 680μs at 1120nm when pumped at 975 nm, and a lifetime of 750 μs at 1160 nm when pumped at 1090 nm [11]. Notably, a previous study reported a lifetime in BASFs of 1 ms [9].

Table 7.2 Lifetime of Bi-doped glass and optical fibres

Fabrication method	Fibre composition	Fluorescence λ_f (nm)	Lifetime at λ_f (μs)	Ref
Melting glass	SiO_2-Li_2O-Al_2O_3-Bi_2O_3	1100	549	[3]
		1350	270	
	Bi_2O_3-Al_2O_3-P_2O_5	1300	500	[4]
	Bi_2O_3-Al_2O_3-GeO_2	1300	255	
	Bi_2O_3-Al_2O_3-GeO_2	1280	273	[5]
	SiO_2-Li_2O -Al_2O_3-Bi_2O_3	1265	456	[6]
	SiO_2-Li_2O -Ta_2O_5-Bi_2O_3	1300	420	
	SiO_2-Na_2O-Al_2O_3-Bi_2O_3	1310	489	
	Bi_2O_3-Al_2O_3-GeO_2	1310	230	
	Bi_2O_3-Ta_2O_5-GeO_2	1310	222	[7]
MCVD & solution	SiO_2-Al_2O_3-GeO_2-P_2O_5-Bi_2O_3	1140	750	[8]
	SiO_2-Al_2O_3-Bi_2O_3	1150	1000	[9]
	SiO_2-P_2O_5-Bi_2O_3	1230	720	[10]
	SiO_2-Al_2O_3-GeO_2-Bi_2O_3	1100	680	[11]
		1130	750	
	SiO_2-P_2O_5-GeO_2-Bi_2O_3	1300	600	[12]
	SiO_2-GeO_2-Al_2O_3-Bi_2O_3	1250	750	[13]
		1250+1650	360	
		Visible red	3.6	
ALD & MCVD	SiO_2-Bi_2O_3-Al_2O_3-GeO_2	1131	701	[14]
		1145	721	

λ_f: peak of the fluorescence spectrum; ALD: Atomic layer deposition

In general, the lifetime of Bi ions within the NIR region tends to be shorter in glass compared to optical fibres. This discrepancy can be attributed to material purity and the ion's immediate environment. However, a definitive range cannot be universally defined for Bi-doped glass and BDFs, as fibre performance is profoundly influenced by fabrication conditions and glass composition. The lifetime analysis is crucial as it can reveal the rate of energy transfer or excited state reactions, as well as indicate the unsaturable process such as quenching occurring in the BDFs. From this perspective, when comparing BDFs of the same type, a longer lifetime may be considered preferable.

7.3.2 Experiment setup

In this study, the lifetime measurement was conducted on the BASFs. Traditionally, the fluorescence intensity can be measured by collecting scattering light from the side of the fibre. However, in the case of BASFs, the light collected from the side was found to be weak, posing difficulty in distinguishing it from system noise. To overcome this, the fluorescence light was monitored by analysing the back-reflected light of BASFs.

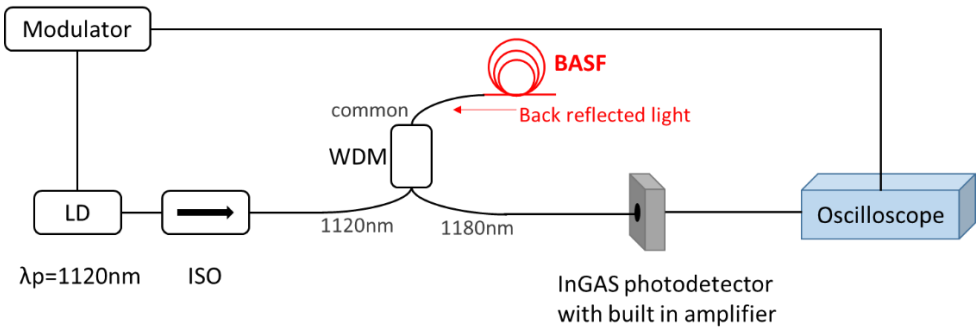

Figure 7.3 Experimental setup of BASFs fluorescence lifetime measurement based on the back-reflected light. (LD: laser diode; ISO: isolator; WDM: wavelength-division-multiplier)

Figure 7.3 presents the schematic diagram of the setup used for measuring the lifetime of BASFs. The setup consisted of a laser diode operating at 1120 nm connected to a modulator (TTI TG550) for square pulse generation. In this study, the pulse frequency was set to 100 Hz, and the duty cycle was either 2:8 or 1:9. The pump diode had a short lifetime of approximately 6 µs and had negligible impact on the fibres' lifetime at 100's of µs scale. The pump light was launched to the BASF through an isolator and an 1120/1180 nm WDM. An additional advantage of employing WDMs is their ability to selectively target specific wavelengths rather than exhibiting transparency across a wide range of different

wavelength bands. The common port of the WDM was spliced with the BASF under test, while the 1180 nm port was connected to an indium-gallium-arsenide (InGAS) photodetector (Thorlabs PDA10CS-EC) with a detectable wavelength from 900 nm to 1700 nm and a built-in amplifier capable of maximum 70 dB amplification. The signal was analysed using an oscilloscope (Tektronix DPO7254) with a 2.5 GHz bandwidth and a 40 GS/s sampling rate. The modulator was also connected to the oscilloscope. To reduce the back-reflection of unabsorbed pump at the end surface, the free end of the BASF was angle-cleaved. The measured result was averaged 10000 times automatically by the oscilloscope to reduce the noise influence and increase the accuracy.

The lifetime was analysed from the fluorescence decay curve using a single exponential fitting, expressed as follow:

$$I(t) = I_0 e^{(-t/\tau)} + y_0 \qquad 7\text{-}3$$

Here, $I(t)$ represents the fluorescence intensity measured at time t, I_0 is the initial light intensity before the decay of ions, τ is the characteristic lifetime to be calculated, and y_0 is a constant offset that accounts for any noise contribution.

To ensure accurate measurement of the fluorescence lifetime, the test BASF should be of a short length to minimise the impact of ASE and re-absorption of the fluorescence light. The pump power should be optimised to achieve sufficient excitation of ions while avoiding any potential stimulated emission or ASE caused by excessive pump power.

7.3.3 Results and discussion

Table 7.3 summarise the lifetime of BASF L10730-A1680 when pumped at 1120 nm, with three lengths used to evaluate the impact on the measured results. The amplification of the detector was adjusted to different values of 50 or 70 dB, depending on the signal intensity and noise level.

Table 7.3 Fluorescence decay time of the BPSF with different fibre lengths

L10730-A1680		λp=1120nm
Fibre length (m)	Signal amplification (dB)	Lifetime (μs)
1.8	70	825
10	50	758
25	50	666

The variation of the measured lifetime with different fibre lengths at a fixed pump power is displayed in Figure 7.4(a). The fluorescence decay time was observed to decrease as the fibre length increased from 1.8 m to 25 m, which is attributed to the impact of the ASE generated in the fibre. Thus, a shorter fibre length was preferred in the lifetime measurement of BASFs to avoid ASE-induced lifetime shortening and the actual lifetime of L10730-A1680 was believed to be ~825 μs. Figure 7.4(b) presents the decay curve of the fluorescence light intensity at three lengths, indicating clear evidence of the lifetime variation. The lifetime in Table 7.3 was calculated by fitting the decay curve with a single exponential function (Equation 7-3). The background loss is eliminated by measuring multiple cycles and considering the baseline across the entire duration.

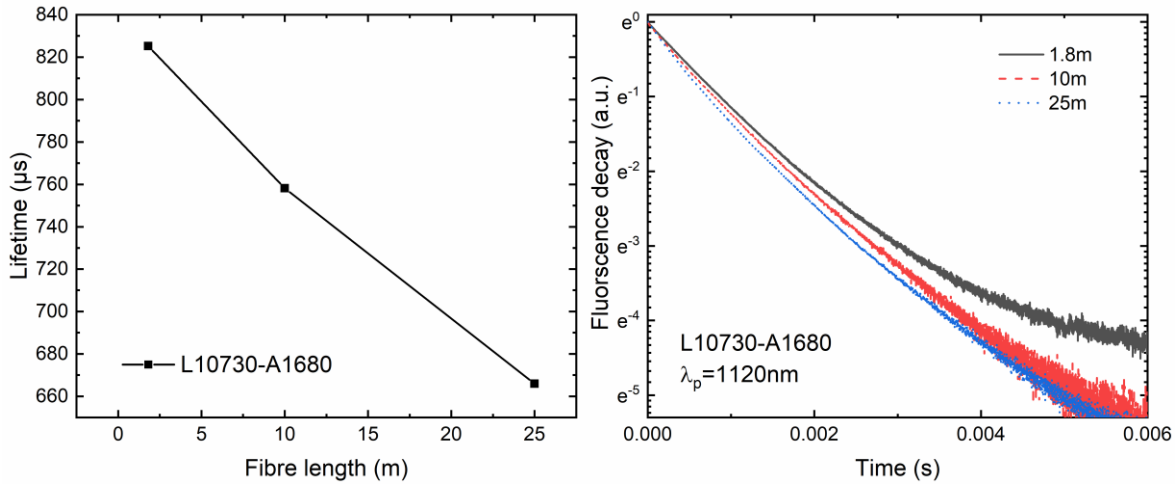

Figure 7.4 (a) Lifetime values of L10730-A1680 at different fibre lengths; (b) Fluorescence intensity decay curve with different lengths excited at 1120 nm.

A second BASF, L10723-A1676-1, was measured with a fixed length of 2 m. To confirm the accuracy of the measurement, various instrument parameters including the modulation amplitude and duty cycle of the pulse, as well as the amplification to the signal, were studied. Specifically, different levels of the modulation amplitude (5,10,20) were selected, which corresponded to increasing levels of modulation current of the pump diode and subsequently, an increase in input pump power. The pump power at the three modulation levels were approximately 50, 100, 200mW. The results are summarised in Table 7.4.

Table 7.4 Fluorescence decay time of the BASF with different measurement parameters

L10723-A1676-1	λp=1120nm	L=2m

Duty cycle (on : off)	Modulation amplitude	Signal gain mode (dB)	Lifetime (μs)
2:8	10	70	814
	20		810
	10	50	841
	20		837
1:9	5	70	840
	10		845
	20		846
	5	50	840
	10		840
	20		836

It can be found that, the variation in the input pump power has a negligible impact on the measured lifetime with a difference of less than 5 μs, which falls within the range of measurement error. However, with a combination of a 2:8 cycle duty and a 70 dB amplification, the measured lifetime values were shorter due to the increased impact of system noise. In contrast, the results from the other three series of measurement settings were consistent with each other, yielding a value of approximately 840 μs for the lifetime of L10723-A1676-1.

The lifetime of other BASF samples was measured using a similar procedure with 1-2m fibre length and 1:9 duty cycle. Different pump power and gain were employed depending on the signal and noise levels. The results are summarised in Table 7.5, along with their corresponding absorption and UL values. The lifetime variation with the absorption or the UL of the fibres is depicted in Figure 7.5.

Table 7.5 Lifetime of different BASFs (absorption and UL used as a reference)

Preform No.	Fibre No.	Lifetime(μs)	Error(±μs)	Absorption(dB/m) @1120nm	UL(%) @1120nm
L10615	A1322	836	10	0.67	55
	A1534	827	9	0.67	41
L10723	A1672	852	12	0.26	59
	A1676-1	844	11	0.6	55
	A1676-2	836	10	0.44	51
L10730	A1680	825	11	0.33	43
	A1681	842	13	0.33	44
L10734	A1692	839	12	0.11	44

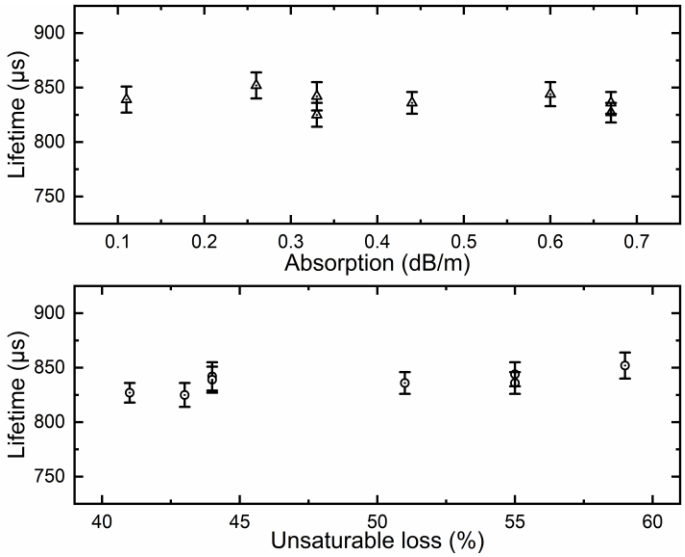

Figure 7.5 Lifetime of different fibres versus the corresponding absorption (up) and unsaturable loss (down)

From Figure 7.5, no significant relation was observed between the lifetime and these factors. The concentration difference of Bi ions in the samples was not significant enough to cause an obvious variation in the lifetime. In comparison to a previous study that demonstrated a concentration-dependent lifetime variation with an absorption range of 0.2 to 20 dB/m [15], our BASFs exhibited a smaller absorption difference of only 0.1 to 0.7 dB/m. Overall, the lifetime of these BASFs remained within the range of 820~860 μs.

7.4 Absorption and emission Cross-section measurement

7.4.1 Principle of transition cross sections measurements

Transition cross sections are used to quantify the rate or the likelihood of optical transition, such as absorption and stimulated emission, and are dependent on the measured wavelength. In a laser system, a higher transition cross-section represents a stronger ability to absorb or emit photons, resulting in a higher transition rate, which is a critical parameter for achieving high laser output power.

The cross sections are obtained from experiments that yield the spectral absorption and emission strength for a particular ion's transition at a specific temperature. Various methodologies have been established to accurately extract cross-section values from the measured absorption and fluorescence spectra, including: (1) Fuchtbauer-Ladenberg (FL) equation; (2) McCumber Theory; (3) Net gain-loss method; (4) Saturated fluorescence

method; and (5) Direct absorption cross section measurement method. These methods have been extensively studied in RE-doped optical fibres, such as Er-doped fibres (EDFs), and have been described and compared in many reports [16-18].

Specifically, the direct measurement method requires full knowledge of the active ions' concentration and radial distribution to derive accurate cross-section values. While this method provides good accuracy for EDFs with a significant absorption over 10 dB/m, its precision diminishes when the absorption is below 2 dB/m [16]. Therefore, this approach is not feasible for BDFs, which have a lower concentration of less than 0.004mol% and a preferable NIR absorption of approximately 0.5 dB/m. McCumber theory is widely used for EDFs cross section analysis and has demonstrated excellent agreement with experimental data, but it has limitation for broad laser transitions in the fibre or glass [19]. As a result, this technique may not be accurate enough for BDFs, which have broad absorption and fluorescence bandwidths spanning several hundred nanometres. The remaining three methods, FL method, gain-loss measurement and saturated fluorescence measurement have shown promising results for various laser gain media such as EDFs and Tm-doped fibres with similar broad linewidths in the emission spectrum [18, 20].

In this study, the transition cross-sections of BASFs were estimated using the FL equation and the McCumber theory modified for broadband gain medium. The principles of these two methods are provided below.

The Fuchtbauer-Ladenberg analysis

The FL theory relates the emission cross-section and the radiative lifetime through the following equation:

$$\frac{1}{\tau_{rad}} = \frac{8\pi n^2}{c^2}\int v^2\sigma_{em}(v)dv = 8\pi n^2 c\int \frac{\sigma_{em}(\lambda)}{\lambda^4}d(\lambda) \qquad 7\text{-}4$$

Here, v and λ are the optical frequency and wavelength, n is the refractive index, c is the vacuum velocity of light, σ_{em} and τ_{rad} denote the wavelength-dependent emission cross-section and radiative lifetime, respectively.

If the emission bandwidth is not large, an average wavelength $\bar{\lambda}$ of the transition can be assumed, and the equation can be written as:

$$\frac{1}{\tau_{rad}} = \frac{8\pi n^2 c}{\bar{\lambda}^4} \int \sigma_{em}(\lambda) d(\lambda) \quad 7\text{-}5$$

Within a narrow frequency interval, the fluorescence intensity $I(\lambda)$ is propotional to the emission cross-section, leading to the following equation:

$$\sigma_{em}(\lambda) = \frac{\bar{\lambda}^4}{8\pi n^2 c \tau_{rad}} \frac{I(\lambda)}{\int I(\lambda) d(\lambda)} \quad 7\text{-}6$$

For gain media with broader emission bandwidths, the equation can be modified for higher accuracy:

$$\sigma_{em}(\lambda) = \frac{\lambda^5}{8\pi n^2 c \tau_{rad}} \frac{I(\lambda)}{\int \lambda\, I(\lambda) d(\lambda)} \quad 7\text{-}7$$

It is worth noting that the FL equation is based on several assumptions, including the absence of inhomogeneous broadening in the gain medium and equal population of all stark components in both the upper and lower energy levels. These assumptions may lead to less accurate cross-section values measured in BDFs.

Modified McCumber theory

The widely used McCumber theory provides a simple relationship between the absorption and emission cross-sections using the following equations:

$$\sigma_{abs}(v) = \sigma_{em}(v) \exp\left(\frac{hv - E_{zl}}{k_B T}\right) \quad 7\text{-}8$$

$$\sigma_{abs}(\lambda) = \sigma_{em}(\lambda) \exp\left(\frac{hc(\frac{1}{\lambda} - \frac{1}{\lambda_{zl}})}{k_B T}\right) \quad 7\text{-}9$$

Here, $h$and $k_B$are the Plank constant and Boltzmann constant, T is the thermodynamic temperature in Kelvin, and E_{zl} and λ_{zl} represent the zero-phonon-line energy and zero-line wavelength corresponding to the lowest components of the upper and lower levels.

However, for gain media with broad emission bandwidths, this equation needs to be modified, as was done in a recent study on Tm-doped fibre [21]. The modified equation is as follows:

$$\sigma_{abs}(\lambda) = \sigma_{em}(\lambda)\frac{Z_u}{Z_l}\exp\left(\frac{hc(\frac{1}{\lambda}-\frac{1}{\lambda_{zl}})}{k_B T}\right) \quad 7\text{-}10$$

Here, the partition function Z_u/Z_l represents the partition function of lower and upper levels and can be considered as the ratio of the energy width for the upper and lower energy levels if equally spaced Stark levels are assumed. The value of Z_u and Z_l can be determined by identifying the intersection point of the 5% intensity level with the normalised absorption and fluorescence spectrum, respectively [21].

7.4.2 Review of the cross-section in Bi-doped glass and optical fibres

Accurate cross-section values are crucial for improving the gain medium and achieving a quantitative understanding of the device in the laser or amplifier systems. In addition to the lifetime described in the previous section, precise cross-section measurements are also necessary for simulating and designing the fibre system. Despite the indispensable role of the transition cross-section, there is limited research available on BDFs, especially regarding a comprehensive cross-sections spectrum. Table 7.6 summarises the published results for Bi-doped optical fibres manufactured using different compositions and fabrication methods, along with some examples of Bi-doped glass. The table indicates whether the data corresponds to absorption or emission cross-section at a specific wavelength (λ_{peak}), and whether a complete spectrum is provided. The Bi-doped glass exhibits emission cross-sections in the range of 9-20×10^{-21} cm^2, while the values of BDFs ranges from 4-20×10^{-21} cm^2.

Table 7.6 Cross-section of Bi ions in glass and optical fibres

Fab. method	Fibre composition	Note	λ_{peak} (nm)	$\sigma(\lambda_{peak})$ ($10^{-21}cm^2$)	Ref
Melting glass	P_2O_5-Al_2O_3-Bi_2O_3	σ_{em}	1300	10.0	[4]
	GeO_2-Al_2O_3-Bi_2O_3	σ_{em}	1300	16.8	
	GeO_2-Al_2O_3-Bi_2O_3	σ_{em}	808	16.1	[5]
		σ_{em}	1280	15.5	
	SiO_2-Al_2O_3-Li_2O-Bi_2O_3	σ_{em}	1265	9.6	[6]
	SiO_2-Ta_2O_5-Li_2O-Bi_2O_3	σ_{em}	1300	11.3	
	GeO_2-Al_2O_3-Bi_2O_3	σ_{em}	1300	19.9	

	Bi_2O_3-Ta_2O_5-GeO_2	σ_{em}	1310	15.9	[7]
MCVD & solution	SiO_2-Al_2O_3-Bi_2O_3	σ_{abs}	925	5	[22]
	SiO_2-Al_2O_3-GeO_2-Bi_2O_3			15	
	SiO_2-Al_2O_3-F-Bi_2O_3	σ_{abs} *Spectrum*	980	4.3	[23]
		σ_{em} *Spectrum*	1140	6.0	
	SiO_2 -Al_2O_3-GeO_2-P_2O_5-Bi_2O_3	σ_{em}	1140	6.0	[8]
	SiO_2-Al_2O_3-Bi_2O_3	σ_{em}	1150	6.0	[9]
	SiO_2-P_2O_5-Bi_2O_3 SiO_2-P_2O_5-F-Bi_2O_3	σ_{abs} *Spectrum*	1240	21	[10]
		σ_{em} *Spectrum*	1310	16	
	SiO_2 -Al_2O_3-GeO_2-Bi_2O_3	σ_{em} *Spectrum*	1100-1160	6~8	[24]
	SiO_2-Al_2O_3-Bi_2O_3	σ_{em} *Spectrum*	1160	7.5(T=300K) 10.5(T=77K)	[25]
ALD & MCVD	SiO_2-Al_2O_3-GeO_2-Bi_2O_3	σ_{em}	1131	8.0	[14]
		σ_{em}	1145	9.6	

7.4.3 Results and discussion

Figure 7.6 shows the emission cross sections calculated using the FL equation for three different BASFs. The results indicate a significant dependence of the emission cross section on the excitation wavelength. As the pump wavelength varied from 1047 nm to 1120 nm, the peaks of the emission cross sections of the three BASFs shifted to the longer wavelength side, from approximately 1130 nm to 1170 nm. Furthermore, an increase in the peak emission cross section was observed in all three fibres, with values of 0.75-0.8 pm^2 (7.5-8×$10^{-21}cm^2$) at 1130 nm and 0.91-0.97 pm^2 at 1170 nm. Similar properties were also observed in our previous studies on BPSFs and Bi-doped aluminogermanosilicate fibres (BAGSF) [1, 2, 24]. The measured emission cross section results are similar to previously reported values [8,9,24].

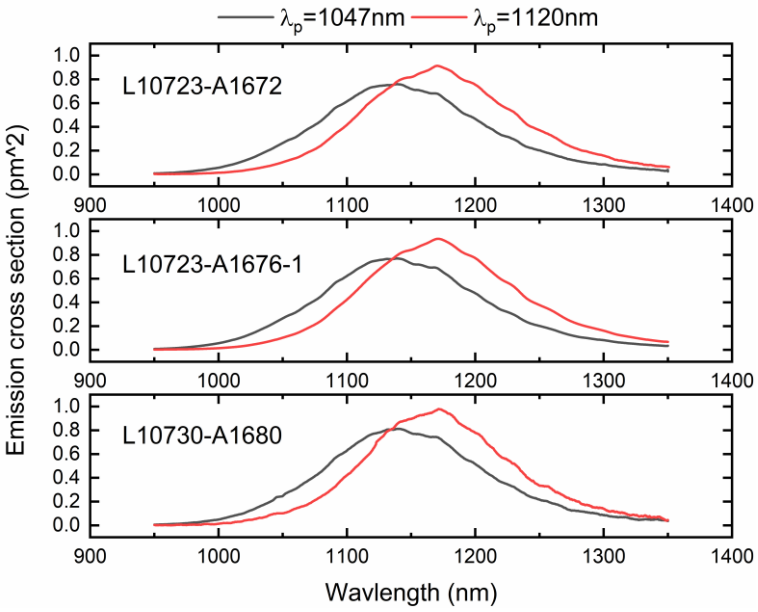

Figure 7.6 Emission cross-sections of BASFs calculated using the Fuchtbauer-Ladenberg analysis.

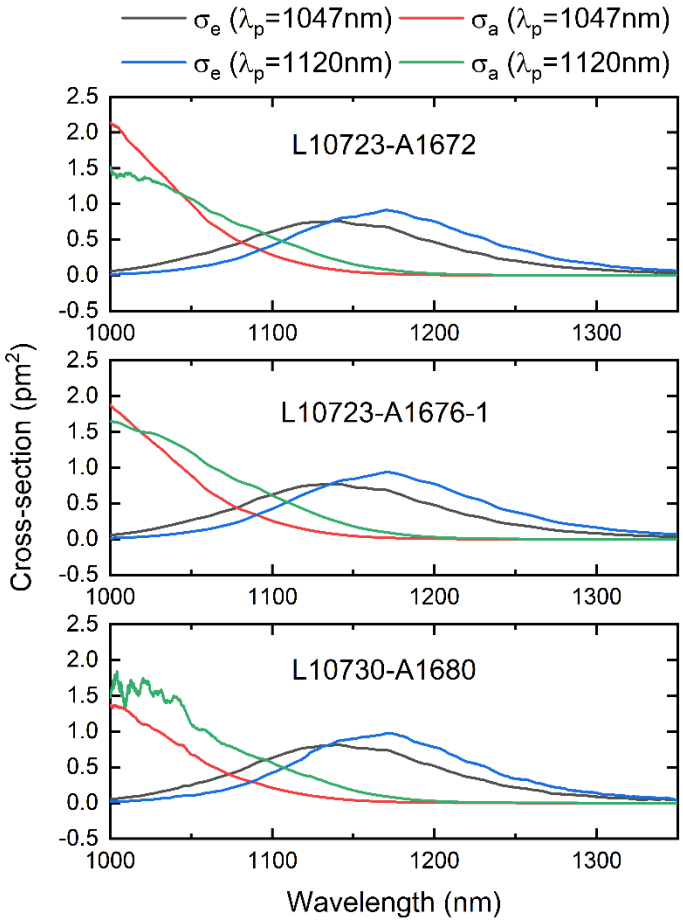

Figure 7.7 Absorption cross-sections of BASFs calculated using the McCumber relation.

Figure 7.7 displays the absorption cross-section spectrum obtained using the modified McCumber relation (Equation 7-10). As the emission cross-section spectrum is dependent on the pump wavelength, the derived absorption cross-sections also vary. This phenomenon requires further investigation and a deeper understanding of the physics behind BDFs. Nonetheless, looking at the general trend of the two series of curves under different pump, the absorption cross-section values increase as the measured wavelength shifts towards shorter side from 1200nm to 1000nm, which agree with the trend of small signal absorption of the BASFs.

An alternative method for obtaining absorption cross-section values is through saturated fluorescence measurement [16-18]. This method provides a specific absolute value at a particular pump wavelength instead of showing different curves by calculating from different fluorescence spectrums. It is worth considering this method in future studies to further compare the results obtained through different analysis methods.

7.5 Anti-stoke luminescence in Bi-doped aluminosilcate fibres

7.5.1 Review of anti-stoke luminescence in BASFs

Anti-stokes luminescence refers to the emission from an energy state higher than the state of the pump energy level, resulting in emitted light with a shorter wavelength than the pump wavelength. This phenomenon has been addressed in Bi-doped aluminosilicate, phosphosilicate and germanosilicate fibres in a number of studies [22, 26-30]. Different visible luminescence has been observed in BDFs with infrared (IR) excitation, depending on the glass composition, the concentration of each dopant, and the temperature (room and liquid nitrogen temperature ~77 K). Table 7.7 provides a summary of reported anti-stokes luminescence at different bands and corresponding excitation wavelengths. In particular, anti-stokes luminescence at 530 nm and 730~780 nm has been observed in BASFs.

Table 7.7 Anti-stokes luminescence in BDFS with different compositions.

Fibre composition	Excitation wavelength(nm)	Luminescence wavelength(nm)	Reference
SiO_2-GeO_2-Bi_2O_3	940	482(T=77K) 655(T=77K)	[26]
SiO_2-Bi_2O_3	803	420(T=77K)	

		480 580(T=77K)	
SiO_2-Al_2O_3-Bi_2O_3	1058	530 730	[22]
SiO_2-Al_2O_3-GeO_2-Bi_2O_3	925	475(T=77K) 730	
SiO_2-Bi_2O_3	1900+1400	830	[27]
	808	420 580	
SiO_2-GeO_2-Bi_2O_3	2000+1650	950	
	925	480(T=77K) 655(T=77K)	
	657+1568	480	
SiO_2-GeO_2(>50%)-Bi_2O_3	925	485 660	[28]
SiO_2-P_2O_5-Bi_2O_3	1300+1840	780	[29]
SiO_2-Al_2O_3-Bi_2O_3	1300+1840	740	
	1150	780	
	1150+1880	750~780(T=77K)	
SiO_2-GeO_2-Bi_2O_3	1515~1575	837 945	[30]

Studying anti-stoke luminescence in different BDFs is beneficial to understanding the energy levels of Bi active centres (BACs) and the mechanisms of various processes in the fibres. The observation of anti-stoke luminescence in BASFs, together with the broadband luminescence spectrum measurement has led to a prediction of the energy levels of the BAC associated with Si (BAC-Si) and Al (BAC-Al), as shown in Figure 7.8 [31]. The 730-780 nm emission corresponds to the energy gap between E_2 and E_0 in BAC-Al, while the 530 nm emission may result from the transition from E_3 to E_0 in BAC-Al, considering the typical broad emission bandwidth in BDFs.

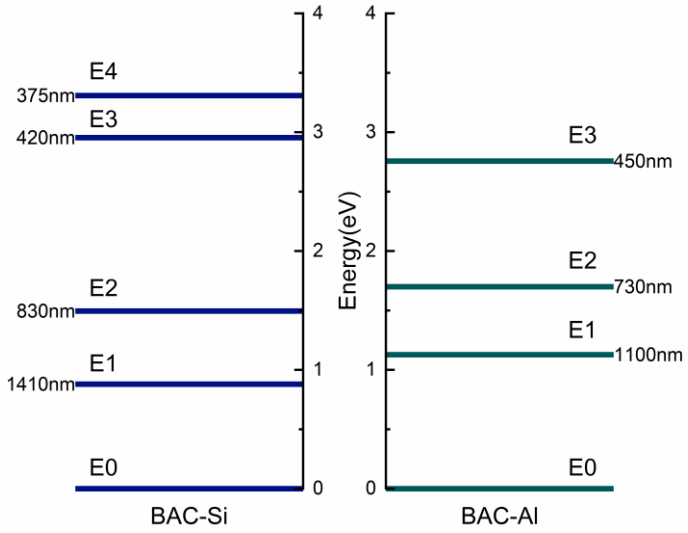

Figure 7.8 Predicted energy level of BAC-Si (left) and BAC-Al (right)

There are several excitation mechanisms that can cause the anti-stokes luminescence, such as excited state absorption (ESA) of a single BAC or energy transfer upconversion (ETU) between neighbouring BACs. Figure 7.9 shows a schematic of the two mechanisms. Both excitation and emission wavelengths are dependent on the energy gaps of different BACs in the fibres. These processes can result in a large UL in the BDFs, reducing the fibre efficiency of the desired process (E_1 to E_0), and eventually degrading the performance of devices based on such fibres.

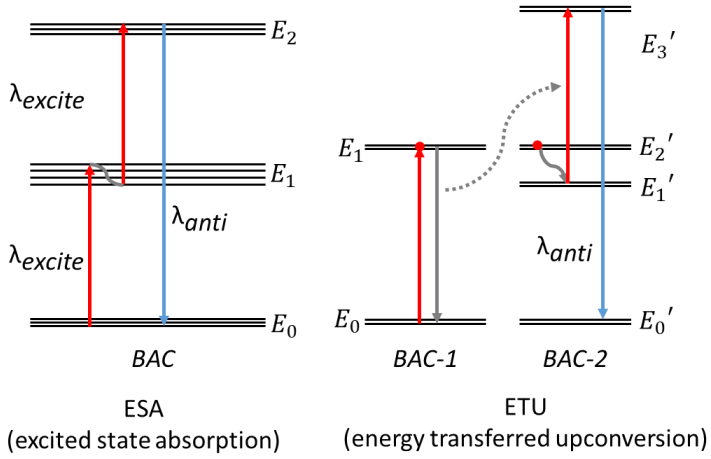

Figure 7.9 Schematic of potential ESA and ETU process in BASFs

7.5.2 Experimental study of anti-stoke luminescence in BASFs

In this study, BASFs (L=5 m) was excited under room temperature (~25 °C) using two pump wavelengths, 1047 nm and 1120 nm. The selection of these two wavelengths was based on the future development of lasers at 1.1 μm. The pumps were combined using a wavelength-

division multiplier (WDM) to monitor the luminescence under single or dual pumps. Our BASFs exhibited visible emission at 480 nm and 570 nm, resulting in a green luminescence as a combination of light at the two wavelengths [32]. Figure 7.10 presents the green light observed in a dark room under different pump wavelengths. The luminescence intensity was stronger when pumped at 1047 nm than at 1120 nm, suggesting that the energy levels of this anti-stokes process can be better matched with the former than the latter.

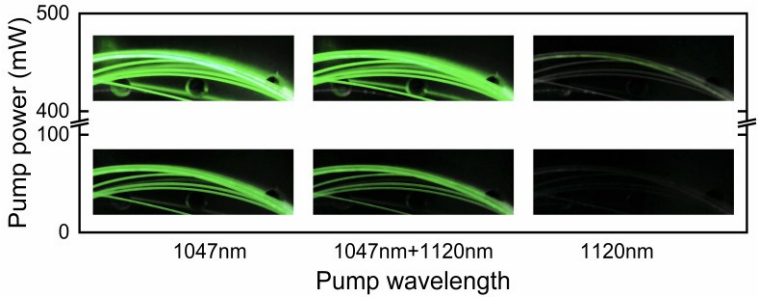

Figure 7.10 Visible luminescence observed in BASFs under different pump configurations.

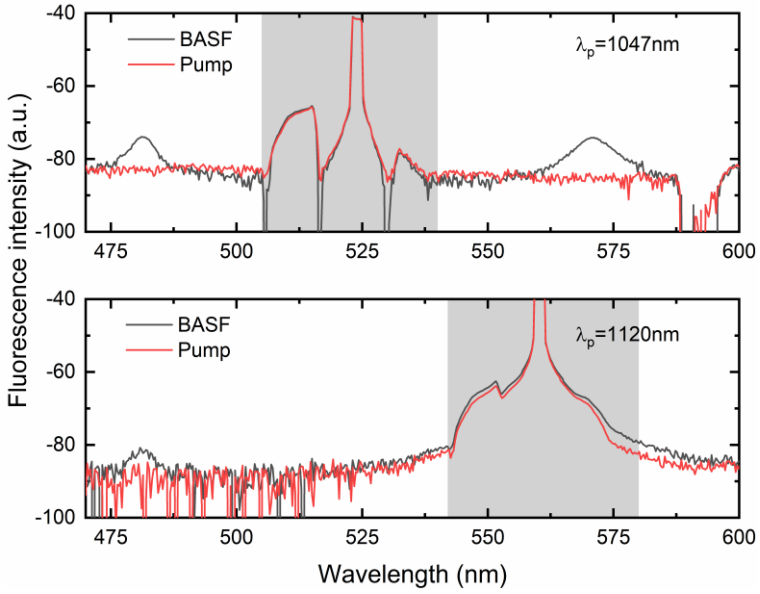

Figure 7.11 Spectrum of the BASF in visible region with the pump wavelengths of 1047 nm (up) and 1120 nm (down). (Red line: monitored from pump; black line: monitored from 5m BASF; shadow: ghost peak from the OSA)

The spectrum of the visible luminescence is shown in Figure 7.11, measured from 450 nm to 600 nm with an OSA resolution of 2 nm. The shadowed regions around 523 nm and 560 nm in the two plots are ghost peaks of the pump wavelength due to the OSA itself. The spectrum clearly shows two peaks at 480 nm and 570 nm when the fibre was pumped with

1047 nm. However, when the 1120 nm pump was used, the 570 nm peak was covered by the ghost signal. To confirm the origin of the two visible peaks in the luminescence spectrum, the pump spectrum was measured without connecting BASFs. Comparing the spectra before and after connecting BASFs confirms that the peaks originate from the fibre. Figure 7.13 provides a detailed view of the two peaks at 480 nm and 570 nm under the 1047 nm pump with increased power.

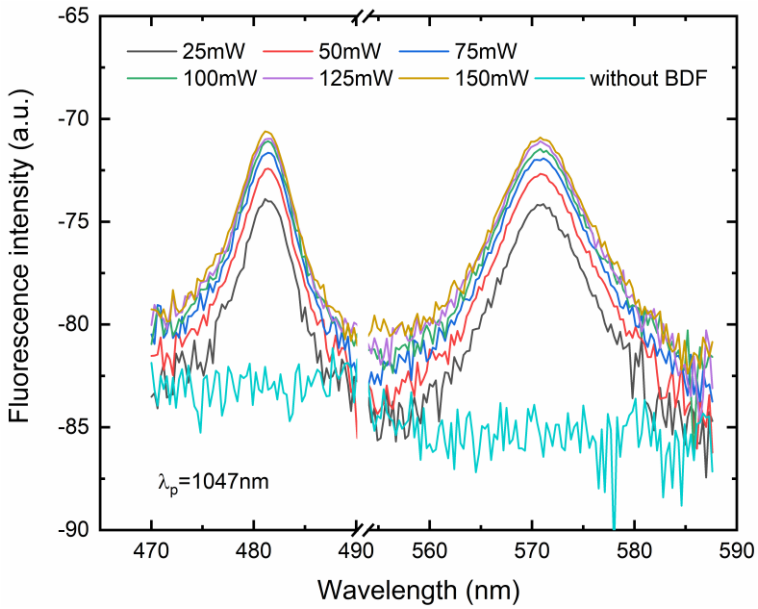

Figure 7.12 Spectrum of anti-stokes luminescence peaks pumped with increased pump power at 1047 nm.

In Figure 7.13, the integrated emission intensity at 480 nm is shown as a function of the input power (up to 100 mW) for single-wavelength pumping and dual-wavelength pumping. The intensities are normalised to the maximum value among all these cases. The results are consistent with Figure 7.10, with stronger luminescence observed under the 1047 nm pump and weaker luminescence under the 1120 nm pump. The combined intensity for dual pumping falls in between. The intensity of the 570 nm luminescence is not calculated due to the overlap between the signal and the ghost peak of the OSA.

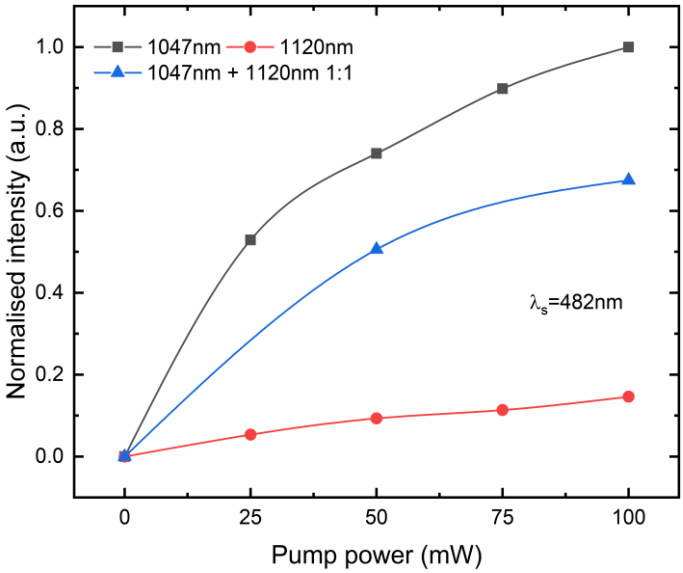

Figure 7.13 Integrated emission intensity of the 480 nm luminescence with single-wavelength pump (black and red lines) and dual-wavelength pump (blue line)

7.5.3 Discussion of the anti-stokes luminescence mechanism

As discussed in Section 7.5.1, several mechanisms can lead to the anti-stokes process. However, the contribution of Bi to our observation is still unclear, as the nature of the material and the energy levels involved are not fully understood. Additionally, different valence states of Bi ions can coexist in the host glass, making the process even more complex. These various ions have distinct energy levels, which are also predicted in [33].

Figure 7.14 shows the normalised intensity of both stokes and anti-stoke luminescence plotted on a log-log scale against the launched pump power. Solid lines with slope of 0.5 are included for guidance. Both stokes and anti-stokes signals exhibited a dependence on the square root of the pump power ($P^{1/2}$). The stokes luminescence trend at 1130 nm is consistent with previous results on BASFs reported in [29], which also showed the same 0.5 slope when pumped at 1240 nm with a power of 10-300 mW. As the pump power increases, the slopes of the two anti-stoke signals become slightly lower than 0.5, which can be attributed to the increased competition between stokes and anti-stokes processes and the insufficient BACs due to the relative low concentration of Bi ions in the fibre [30].

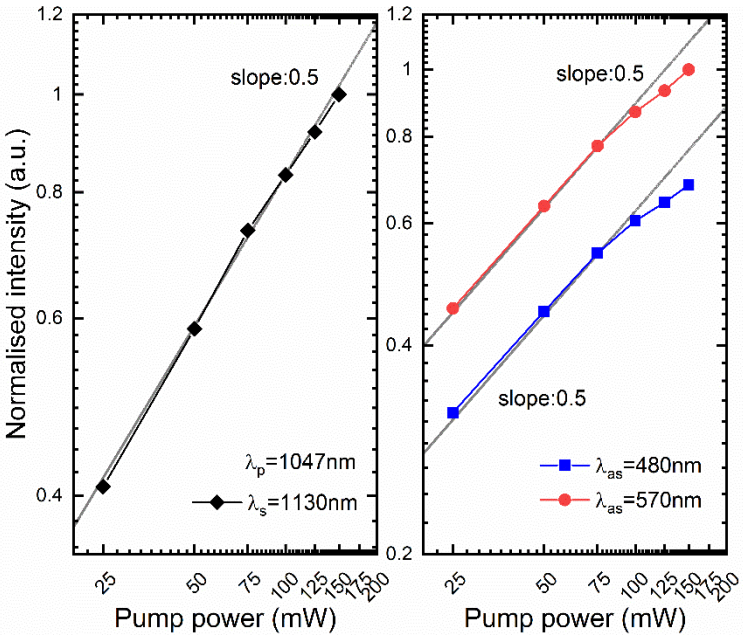

Figure 7.14 Normalised stokes and anti-stoke luminescence intensity of the BASF as a function of launched pump power at 1047 nm, plotted in a log-log scale.

In theory, the power dependence of excited ions population densities ($N_i, i = 1,2,\dots,n$) varies in cases of ETU and ESA. The correlation between these densities and the launched pump power can be expressed according to the model established in [34]. When the fibre undergoes the ETU or ESA process, the power-dependence can be different depending on the impact (small or large) and the decay route of the ions, as described in Table 7.8:

Table 7.8 Correlation between the excited ions population densities N and launched pump power P in various cases.

Upconversion mechanism	Influence of upconversion	Decay Route		Power dependence
		From level	Decay to	
(1)ETU	(a)Small	I=1,2,…,n	Ground state	$N_i \sim P^i$
	(b)Large	(i) I=1,2,…,n-1		$N_i \sim P^{1/2}$
		(ii) I=n		$N_i \sim P^1$
(2)ESA	(a)Small	I=1,2,…,n		$N_i \sim P^i$
	(b)Large	(i) I=1,2,…,n-1		$N_i \sim P^0$
		(ii) I=n		$N_i \sim P^1$

The model predicts a higher possibility for ETU to occur in our BASFs as the 0.5 slope fits the case (1)(b)(i). However, further investigation is necessary before reaching a definitive conclusion. Although the model provides a general equation for power dependence in

different anti-stokes processes, special cases need to be considered, particularly the involvement of different active centres (BAC-Si and BAC-Al), various valence states, and energy levels of the Bi ions, which further complicates the situation.

7.6 Conclusion

In this chapter, several spectroscopic studies related to the fluorescence spectrum, lifetime and cross-section have been introduced to the homemade BASFs, which exhibited a broad gain bandwidth of over 100nm centring at 1120~1160nm, depending on the pump wavelength. The fluorescence decay lifetime of the BASFs was measured, and the general value was found to be approximately 820-840μs. The emission and absorption cross-sections were measured based on the Fuchtbauer-Ladenberg relation and the modified McCumber theory. The spectrum showed a pump-wavelength dependence, which corresponded to the same dependence shown in the fluorescence spectrum. The physical theory behind this is under further investigation.

Moreover, an observation of visible light from anti-stokes luminescence has been studied. Two peaks at 480nm and 570nm were observed when the BASF was pumped under 1047nm and 1120nm. The intensities of stokes and anti-stokes luminescence was calculated and compared and ETU is predicted as the involved process in the fibre. However, further investigation is required for a precise description of this process due to the complicated composition of different BACs. This anti-stokes process can be a reason for the low efficiency of our BASFs.

7.7 Reference

[1] Y. Wang, “The study of bismuth doped fibres and the development of broadband bismuth doped fibre amplifiers”, PhD thesis, 2023, University of Southampton, UK

[2] Y. Wang, S. Wang, A. Halder, and J. Sahu, “Bi-doped optical fibers and fiber amplifiers”. *Optical Materials: X*, **17**, 100219 (2023).

[3] E.M. Dianov, “Bismuth-doped optical fibers: a challenging active medium for near-IR lasers and optical amplifiers.” *Light: Science & Applications*, **1**(5), e12-e12 (2012).

[4] X.G. Meng, J.R. Qiu, M.Y. Peng, D.P. Chen, Q.Z. Zhao, X.W. Jiang, C.S. Zhu, "Near infrared broadband emission of bismuth-doped aluminophosphate glass", *Optical Express*, **13**, 1628-1634(2005).

[5] M.Y. Peng, C. Wang, D.P. Chen, J.R. Qiu, X.W. Jiang, C.S. Zhu, "Investigations on bismuth and aluminum co-doped germanium oxide glasses for ultra-broadband optical amplification", *Journal of Non-Crystalline Solids*, **351**, 2388-2393(2005).

[6] M.Y. Peng, B.T. Wu, N. Da, C. Wang, D.P. Chen, C.S. Zhua, J.R. Qiu, "Bismuth-activated luminescent materials for broadband optical amplifier in WDM system" *Journal of Non-Crystalline Solids*, **354**, 1221-1225(2008).

[7] M.Y. Peng, J.R. Qiu, D.P. Chen, X.G. Meng, C.S. Zhu, "Superbroadband 1310 nm emission from bismuth and tantalum codoped germanium oxide Glasses", *Optical Letters*, **30**, 2433-2435(2005).

[8] I. Razdobreev, L. Bigot, V. Pureur, A. Favre, G. Bouwmans, and M. Douay, "Efficient all-fiber bismuth-doped laser". *Applied physics letters*, **90**(3), 031103 (2007).

[9] E.M. Dianov, V.V. Dvoyrin, V.M. Mashinsky, A.A. Umnikov, M.V. Yashkov, A.N. Gur'yanov, "CW bismuth fibre laser", *Quantum Electronics*, **35**, 1083-1084(2005).

[10] A. Khegai, S. Firstov, K. Riumkin, S. Alyshev, F. Afanasiev, A. Lobanov, A. Guryanov, and M. Melkumov, "Radial distribution and absorption cross section of active centers in bismuth-doped phosphosilicate fibers". *Optics Express*, **28**(20), 29335-29344 (2020).

[11] M.P. Kalita, S. Yoo, and J.K. Sahu, "Bismuth doped fiber laser and study of unsaturable loss and pump induced absorption in laser performance." *Optics express*, **16**(25), 21032-21038. 2008

[12] N. K. Thipparapu, Y. Wang, S. Wang, , A. A. Umnikov, P. Barua, and J. K. Sahu, "Bi-doped fiber amplifiers and lasers [Invited]". *Optical Materials Express*, **9**(6), 2446-2465(2019)

[13] Y. Qiu, and Y. Shen, "Investigation on the spectral characteristics of bismuth doped silica fibers." *Optical Materials*, **31**(2), 223-228 (2008).

[14] J. Wen, J. Wang, Y. Dong, N. Chen, Y. Luo, G.D. Peng, F. Pang, Z. Chen, and T. Wang, "Photoluminescence properties of Bi/Al-codoped silica optical fiber based on atomic layer deposition method". *Applied Surface Science*, **349**, 287-291 (2015).

[15] A.V. Kir'yanov, V.V. Dvoyrin, V.M. Mashinsky, Y.O. Barmenkov, and E.M. Dianov, "Nonsaturable absorption in alumino-silicate bismuth-doped fibers." *Journal of Applied Physics*, **109**(2), 023113 (2011).

[16] E. Desurvire, *Erbium-doped fiber amplifiers: principles and applications*, ch. 4, Characteristics of erbium-doped fibers. Wiley, 2002.

[17] P. M. Becker, A. A. Olsson, and J. R. Simpson, *Erbium-doped fiber amplifiers: fundamentals and technology*. Ch. 4 Rare Earth Ions—Introductory Survey. Elsevier. 1999.

[18] W. L. Barnes, R. I. Laming, E. J. Tarbox, and P. R. Morkel, "Absorption and emission cross section of Er^{3+} doped silica fibers". *IEEE Journal of Quantum Electronics*, **27**(4), pp.1004-1010(1991).

[19] M.J. Digonnet, E. Murphy-Chutorian and D.G. Falquier, "Fundamental limitations of the McCumber relation applied to Er-doped silica and other amorphous-host lasers". *IEEE journal of quantum electronics*, **38**(12), 1629-1637(2002).

[20] S.D. Agger, and J.H. Povlsen, "Emission and absorption cross section of thulium doped silica fibers". *Optics Express*, **14**(1), 50-57(2006).

[21] L. Zhang, J. Zhang, C. Yu, and L. Hu, "A method for emission cross section determination of Tm 3+ at 2.0 μ m emission." *Journal of Applied Physics*, **108**(10), 103117 (2010).

[22] I. A. Bufetov, S. V. Firstov, V. F. Khopin, A. N. Guryanov, and E. M. Dianov. "Visible luminescence and upconversion processes in Bi-doped silicabased fibers pumped by IR radiation." In 2008 *34th European Conference on Optical Communication*, 1-2. IEEE, 2008.

[23] V.V. Dvoyrin, V.M. Mashinsky, E.M. Dianov, A.A. Umnikov, M.V. Yashkov, and A.N. Guryanov, 2006. "Bi-doped silica fibers-a new active medium for tunable fiber lasers and broadband fiber amplifiers". In *2006 Optical Fiber Communication Conference and the National Fiber Optic Engineers Conference*. IEEE.

[24] S. Yoo, M. P. Kalita, J. Nilsson, and J. Sahu, "Excited state absorption measurement in the 900-1250 nm wavelength range for bismuth-doped silicate fibers," *Optical Letters*, **34**, 530-532 (2009)

[25] V.V. Dvoyrin, , V.M. Mashinsky, and E.M. Dianov, "Efficient bismuth-doped fiber lasers. *IEEE journal of quantum electronics*", **44**(9), 834-840 (2008).

[26] S. V. Firstov, V. F. Khopin, I. A. Bufetov, E. G. Firstova, A. N. Guryanov, and E. M. Dianov, "Combined excitation-emission spectroscopy of bismuth active centers in optical fibers," *Optical Express* **19**, 19551-19561 (2011)

[27] S.V. Firstov, V.F. Khopin, V.V. Velmiskin, E.G. Firstova, I.A. Bufetov, A.N. Guryanov, and E.M. Dianov, "Anti-Stokes luminescence in Bismuth-doped silica and germania-based fibers". *Optics express*, **21**(15), 18408-18413(2013).

[28] S.V. Firstov, E.G. Firstova, A.V.E. Kharakhordin, K.E.E. Riumkin, S.V. Alyshev, M.A. Melkumov, and E.M. Dianov, "Anti-Stokes luminescence in bismuth-doped high-germania core fibres". *Quantum Electronics*, **49**(3), 237 (2019).

[29] S.V. Firstov, K.E.E. Riumkin, V.F. Khopin, S.V. Alyshev, E.G. Firstova, M.A. Mel'kumov, A.N. Gur'yanov, and E.M. Dianov, "Anti-Stokes luminescence in bismuth-doped alumino- and phosphosilicate fibres under two-step IR excitation". *Quantum Electronics*, **46**(7), 612 (2016).

[30] W. Fan, L. Htein, B.H. Kim, P.R. Watekar, and W.T. Han, "Upconversion luminescence in bismuth-doped germano-silicate glass optical fiber". *Optics & Laser Technology*, **54**, 376-379(2013).

[31] A. M. Khegai, S. V. Alyshev, A. S. Vakhrushev, K. E. Riumkin, A. A. Umnikov, and S. V. Firstov. "Recent advances in Bi-doped silica-based optical fibers: A short review." *Journal of Non-Crystalline Solids: X* 100126(2022).

[32] Fairchild, M.D., 2013. Color appearance models. John Wiley & Sons.

[33] A. Halder, A. Kir'yanov, , E. H. Sekiya, and K. Saito, "Fabrication and characterization of bismuth-doped germano-silicate and phospho-silicate fibers for VIS/NIR applications". *Optical Materials Express*, **9**(4), 1815-1825(2019).

[34] M. Pollnau, D. R. Gamelin, S. R. Lüthi, H. U. Güdel, and M. P. Hehlen, “Power dependence of upconversion luminescence in lanthanide and transition-metal-ion systems”. Physical Review B, **61**(5), 3337(2000).

Chapter 8 Study of Bi-doped aluminosilicate fibre lasers

8.1 Introduction

After the fabrication and characterisation of Bi-doped aluminosilicate fibres (BASFs), as discussed in detail in the preceding sections, this chapter presents further experimental results obtained when the fibres were tested in a laser setup and pumped at wavelengths of 1047nm and 1120nm.

This chapter focuses on evaluating the laser performance of BASFs, through modifications to the cavity design, active fibre length, and output coupling ratio. By adopting a linear configuration for the laser cavity, the required fibre length was significantly reduced to 50~75 m, compared to over a 200 m Bi-doped phosphosilicate fibre (BPSF) for lasers at 1.3 μm (as discussed in Chapter 5). This study includes a detailed investigation of single and dual pumping techniques. However, poor output power and slope efficiency were observed due to the high unsaturable loss (UL) in BASFs (60%), in contrast to BPSFs, which have lower UL of approximately 20%.

8.2 Bi-doped aluminosilicate fibre laser by 1047nm pump

8.2.1 Experiment setup

In this study, BASF L10730-A1680 was employed in a linear laser cavity. The absorption and UL are 0.66 dB/m and 61% at 1047 nm, and 0.33 dB/m and 43% at 1120 nm, respectively. The refractive index difference is 0.006, primarily from the Al_2O_3 content of approximately 2.80 mol%, measured by the electron probe microanalysis (EPMA). The concentration of Bi ions is around 0.002 mol% estimated by EPMA, with the accuracy limited by the measurement technique (Table 6.5). The fibre has a cladding diameter of 100 μm and an inner core diameter of 13 μm. These characterisation details are available in Section 6.3 and 6.4. This particular fibre was chosen due to its relatively low UL compared to other BASFs, as previous studies have shown that lower UL results in higher output and efficiency. Additionally, BPSFs with an absorption of 0.5dB/m performed well in a laser setup in our previous study [1], leading us to select a similar absorption level for the preliminary testing of BASFs.

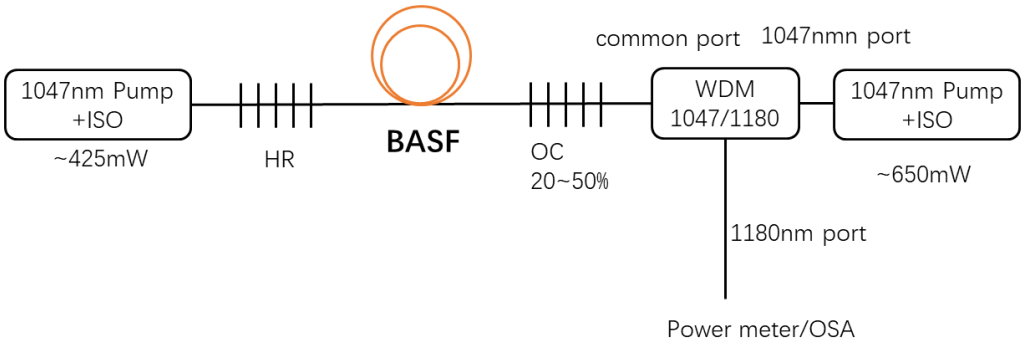

Figure 8.1 Schematic of the laser setup operating at 1178nm.

Figure 8.1 illustrates the schematic diagram of the laser setup designed for operation at 1178 nm. Two diode pumped neodymium-doped yttrium lithium fluoride (Nd:YLF) lasers operating at 1047 nm were employed to pump the BASF bi-directionally under a total power of approximately 1 W. Two isolators (ISOs) were spliced to the diodes in order to prevent any damage due to the back-reflected and unabsorbed light. A linear cavity was formed by two fibre Bragg gratings (FBGs) at 1178 nm. One FBG has a high reflectivity (HR) of 99%, while the other was used at an output coupler (OC) with a reflectivity of 20%, 30%, 50% for comparative purposes. The output signal was obtained using a 1047/1180 nm WDM and connected to a power meter or an OSA. The BASF was tested in the cavity using two different lengths, 53 and 78 m. The fibre length used was not further reduced to avoid exhausting the available fibres for other study. Nonetheless, it should be noted that due to the relative low absorption at the pump wavelength, there is a low probability of further reducing the fibre length being beneficial.

8.2.2 Results and discussion

Table 8.1 provides an overall summary of the laser performance. Three output coupling ratios (OC ratios) of 80%, 70%, 50% were tested for two specific fibre lengths (53 m or 78 m) by inserting FBGs with different reflectivity values (20%, 30%, 50%). Both output power and optical spectrum were measured for each configuration. The maximum output power achieved was approximately 8 mW at 1178 nm, with a slope efficiency of 2.26%. The low slope efficiency and output power can be attributed to the high UL of the BASF (60%). Additional, at high pump power, there was increased competition between the unsaturable process, including the anti-stoke luminescence, and the desired radiative process at 1.1 µm, resulting in instability of the laser and fluctuation of the output power.

Table 8.1 Laser output power and slope efficiency under different cavity configuration

Output Power (mW) (Pump power~1W)			
OC ratio (%) / Length (m)	80	70	50
53	8.20	7.28	6.40
78	6.28	5.18	4.02
Slope efficiency (%) (measured before reaching saturation)			
OC ratio (%) / Length (m)	80	70	50
53	2.26	1.74	1.2
78	1.79	1.53	1.1

Figure 8.2 presents the laser output power and the slope efficiency versus the coupling ratio for each specific length, 53 and 78m. As previously mentioned, the fibre length was not further reduced due to the fibre's low absorption and to prevent unnecessary wastage. The output power increased with the output ratio but was expected to reach a peak and then decrease. This behaviour can be assumed as a larger output ratio results in higher cavity loss, which increases the threshold of the laser and reduces the total power generated in the cavity. The slope efficiency also increased with the coupling ratio for each fibre length, but it was limited to a maximum of 2.3% across all the cases.

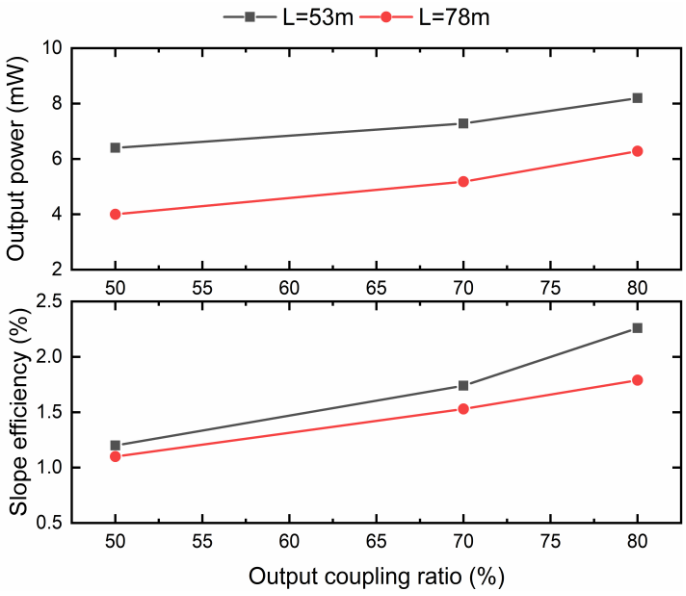

Figure 8.2 Laser output power and slope efficiency versus cavity output coupling ratio

Figure 8.3 shows the variation in output power with the pump power operating at 1047 nm up to a maximum of 1.1 W. The result shows the increase of the threshold when the output

coupling ratio was raised from 50% to 80% (FBG reflectivity 50% to 20%, respectively), as well as when the fibre length was increased from 53 m to 78 m. Correspondingly, the slope efficiency increased at higher output ratios. However, the BASF showed saturation when the pump power reached the range of 700-800mW. These results indicate the consumption of a large fraction of Bi ions in the fibre by the UL related energy transmission including upconversion. Reducing the UL would reduce the proportion of Bi ions involved in such detrimental energy transfer processes, thus potentially improving the output power.

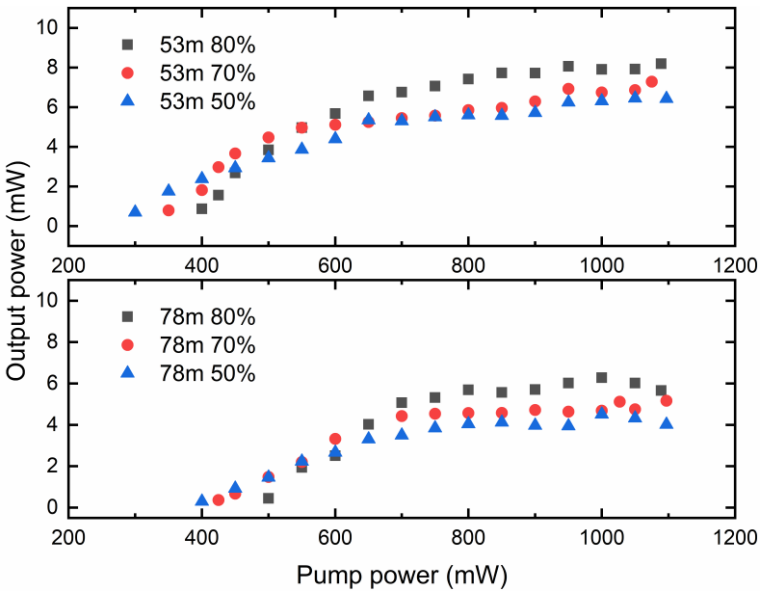

Figure 8.3 Laser output power versus pump power with different output ratios and BASF lengths

The optical spectrum was measured with an OSA resolution bandwidth of 1 nm. In order to make a meaningful comparison, the pump power was kept constant across different cases. Figure 8.4 displays an example of the measured spectrum with a fixed output coupling ratio of 50% and two different fibre lengths. The unabsorbed pump power was identified by peaks at 1047 nm. When the BASF with a longer length of 78 m was connected to the cavity, less unabsorbed pump power was observed through the output, and the ASE peak shifted towards longer wavelengths from 1160 nm to 1165 nm. Despite the ASE peak being closer to the lasing wavelength and the pump being more absorbed, the peak at 1178 nm showed a decrease with an increase in the fibre length. The optical signal-to-noise ratio (OSNR) remained greater than 40 dB. The inset of Figure 8.4 is a magnified view of the peak at the signal wavelength of 1178 nm. The flat top of the peak in the figure was because the 1 nm resolution bandwidth of the OSA was broader than the linewidth of the laser signal.

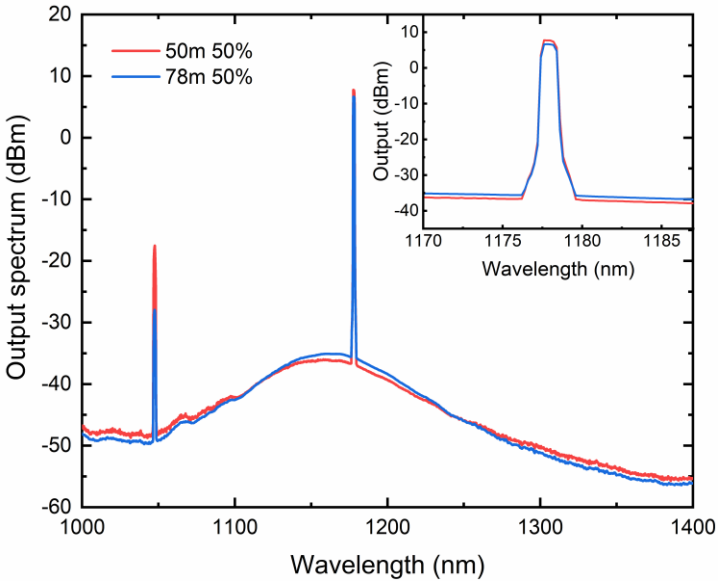

Figure 8.4 Spectrum of the BASF laser with the output coupling ratio of 50% and different fibre length, measured with an OSA resolution bandwidth of 1 nm; inset: a magnified view of the peak at 1178 nm.

In all the aforementioned scenarios, both bi-directional pumps were launched simultaneously and with equal power into the fibre. To further investigate the effect of pump direction, an additional experiment was conducted. The experimental setup was kept the same, but the pumps were activated sequentially, with their power gradually increased until the maximum value was reached. The experiment was performed under three situations, in particular, a fibre length/output coupling ratio of 53 m/70%, 53 m/80% and 78 m/80%. The output power and pump power were measured and are presented in Figure 8.5.

The figure provides clear evidence that the laser output at maximum pump power was unaffected by the sequential launch of the two pumps and remained equivalent to the output obtained with the equal and simultaneous bi-directional pump configuration. However, in the linear region of the output power before the fibre was fully saturated, significant variations in the threshold and slope efficiency were observed between the three configurations. These variations can be attributed to the impact of the pump direction on the distribution of excited ions along the length of the fibre.

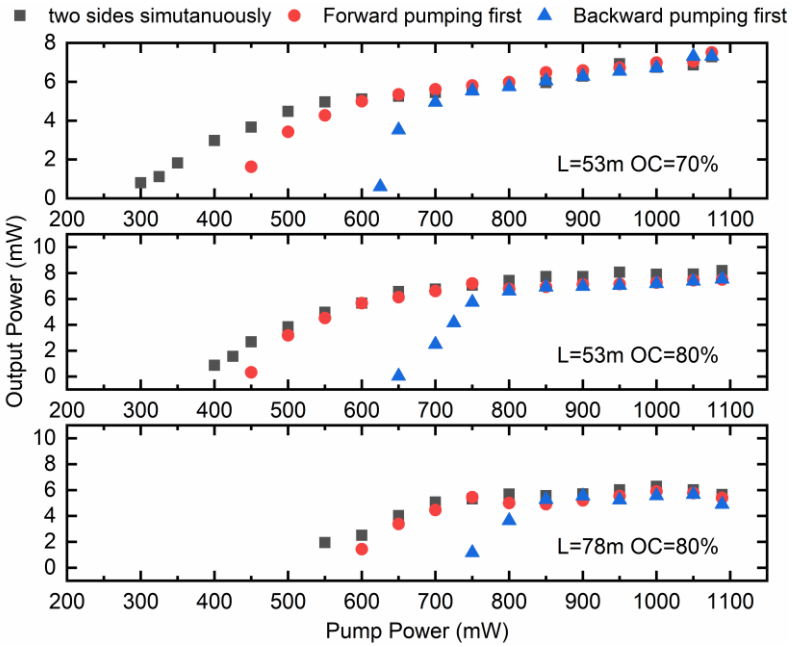

Figure 8.5 Laser output power versus pump power at 1047 nm, under three different pump orders: two sides equally and simultaneously (black) or one after the other (red and blue)

Overall, the current laser at 1178 nm suffers from large impact of the high UL (60% at the pump wavelength of 1047 nm. A saturation state was observed when the pump power exceeds the range of 700-800 mW. Increasing the concentration of Bi dopants may increase the number of ions involved in the lasing process, but it would also lead to a corresponding increase in the UL [2]. Therefore, a delicate balance must be achieved between absorption and UL. Alternatively, selecting pump wavelengths that provide lower UL may increase the laser performance. An experiment exploring this possibility will be discussed in the next section.

8.3 Dual pumping Bi-doped aluminosilicate fibre laser

8.3.1 Experiment setup

In order to reduce the impact of high UL in BASF, a dual-wavelength pumping configuration was utilised in which a pumping wavelength of 1120 nm was applied alongside the prior 1047 nm wavelength. This approach has the advantage of decreasing the intracavity UL to an effective value that lies between the individual UL at the two pump wavelengths. Although using 1120 nm as the sole pump wavelength would further decrease the UL, the absorption at this wavelength is approximately half of that at 1047 nm, resulting in a

significant increase of lasing threshold and required fibre length. Another advantage of using a longer pump wavelength is that the ASE peak of the BASF will shift towards the longer wavelength side, which can be beneficial if the signal wavelength (determined by the FBG) coincides with the peak gain position.

The experimental setup for the BASF laser pumped at 1047 nm and 1120 nm is indicated in Figure 8.6. The forward pumping was achieved through a Nd:YLF laser at 1047 nm with 600 mW power, followed by an isolator (ISO). Two additional laser diodes at 1120 nm were spliced to a polarisation beam combiner (PBC) to provide a total 500 mW of backwards pump power. The output port of the PBC was connected to another ISO. Both the forward and backward pumps were increased simultaneously and launched to the BASF with equal value power.

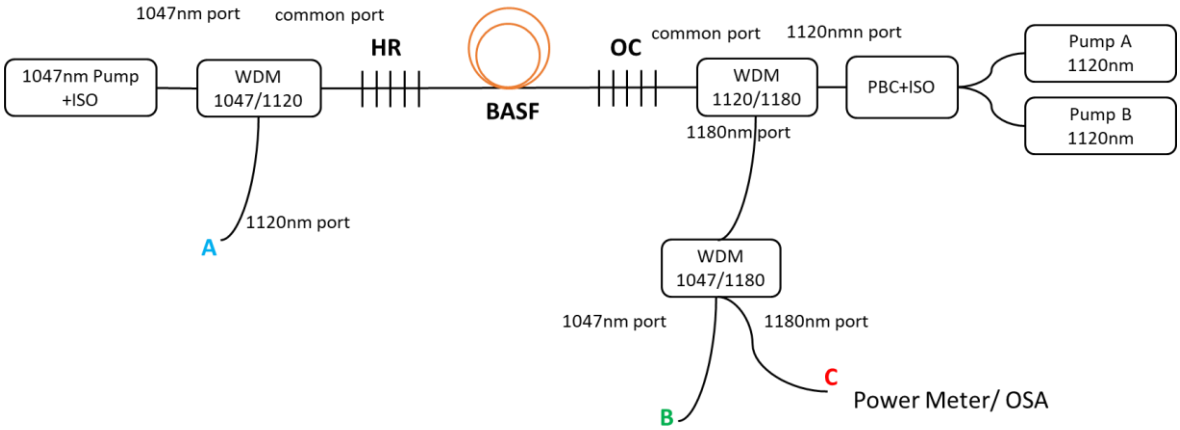

Figure 8.6 Schematic of the setup for the dual-wavelength-pumped BASF laser. Two FBGs were used as HR and OC. The output was measured from port C by both the OSA and the power meter. PBC: polarisation beam combiner; ISO: isolator.

The laser cavity was constructed with two FBGs acting as the HR and OC, respectively, with the reflectivity of 99% and 50% and the operating wavelength of 1178 nm. This configuration was similar to the setup described in Section 8.2.1. The selection of a 50% coupling ratio as a starting point was based on the convenience for further adjustment, given that a middle level coupling ratio was desired. The OC grating was connected to the common port of an 1120/1180 nm WDM, while the 1120 nm port was connected to the pump. The 1180 nm port was followed by a 1047/1180 nm WDM to filter out any unabsorbed pump at 1047 nm (port B). Port C served as the laser output and was monitored by a power meter and an OSA for power and spectrum measurements. Another 1047/1120

nm WDM was placed between the forward isolator and the HR grating to monitor the unabsorbed 1120 nm pump power (port A) and avoid excessive power propagating to the isolator and causing heat build-up in the component.

8.3.2 Results and discussion

Three BASFs were tested in the setup of varying fibre lengths, selected based on their respective absorption values. The results in terms of output power and slope efficiency are summarised in Table 8.2, along with the absorption and UL values at the respective pump wavelengths for each fibre as references.

Table 8.2 Summary of laser output under 1047/1120 nm dual wavelength pumping

Fibre No.	Absorption(dB/m)		UL(%)		Length(m)	P_{out}(mW)	Slope efficiency
	1047nm	1120nm	1047nm	1120nm			
L10730-A1680	0.66	0.33	61	43	53	17	2.3%
					78	11	2.1%
L10723-A1676-1	1.2	0.64	68	55	25/50/75	No lasing	
L10734-A1692	0.18	0.11	47	40	200	No lasing	

Among the three fibres tested, the BASF L10723-A1676-1 exhibited higher UL values of 68% and 55% at 1047 nm and 1120 nm, respectively, preventing lasing in the cavity even when the tested length varied from 25 m to 75 m. Despite the lower UL values of L10734-A1692, the low absorption of 0.18 dB/m resulted in a required fibre length of 200 m. However, the increased fibre length still could not overcome the fibre loss, ultimately resulting in no lasing. This observation highlighted the critical role of the absorption in the lasing process. Specifically, the fibre L10730-A1680 exhibited absorption within the range of the other two fibres and was capable of generating lasing in the tested cavity.

Figure 8.7 presents the relationship between the laser output power and the pump power. The pump power was increased by every 50 mW, consisting of 25 mW at 1047 nm and 25 mW at 1120 nm. Once the 1120 nm pump reached its maximum level, the 1047 nm pump was further increased to its full capacity. The laser cavity exhibited a lower threshold at a fibre length of 53 m, approximately 450 mW, and a higher threshold at a fibre length of 78 m, approximately 550 mW. At a maximum pump power of 1.2 W, the laser demonstrated an output power of 17 mW and 11 mW for the two cases, with similar slope efficiencies of 2.3% and 2.1%.

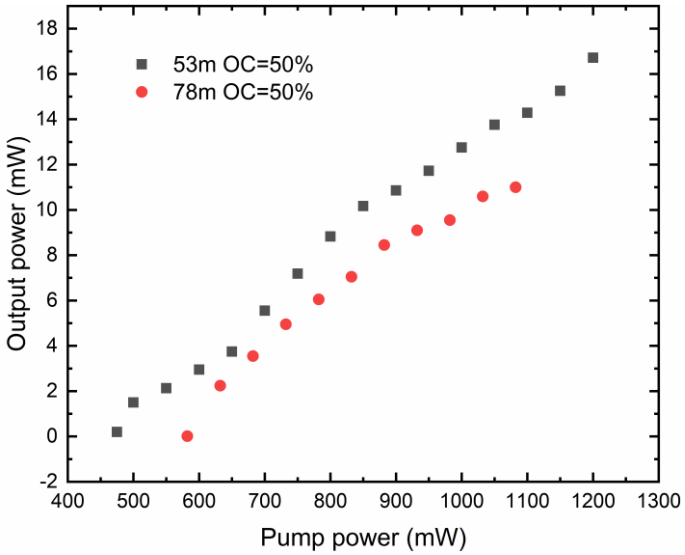

Figure 8.7 Output power variation with increased pump power of L10730-A1680 pumped at 1047 and 1120nm.

The output spectrum of the two cases were measured under a pump power of 1 W with an OSA resolution bandwidth of 1 nm, as illustrated in Figure 8.8. Lasing was observed at the wavelength of 1178 nm, as defined by the central wavelength of the FBGs. The peaks at 1047 nm and 1120 nm correspond to the unabsorbed pump power. A longer cavity length resulted in more absorption of the pump power, leading to lower peaks at the two wavelengths (blue solid line) in the spectrum, while a shorter cavity length resulted in higher peaks (red dotted line).

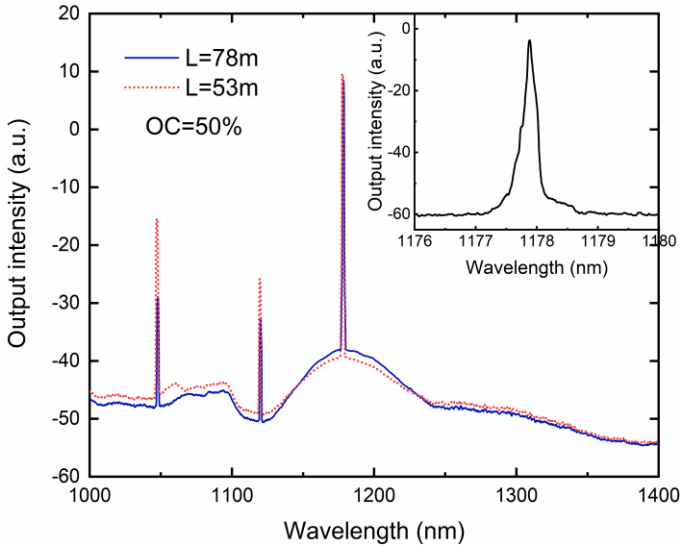

Figure 8.8 Laser output spectrum measured with a 1nm OSA resolution bandwidth. Inset: 4nm span of the signal peak at 1178nm, measured with a 0.02nm resolution bandwidth.

Comparing to the laser pumped only at 1047 nm (Section 8.2.2), employing the dual-wavelength pumping configuration shifted the ASE peak from 1160 nm to 1180 nm. The inset of Figure 8.8 shows the spectrum of the lasing signal measured with an OSA bandwidth of 0.02 nm. The peak shape was resolved with a linewidth of ~0.05nm (FWHM).

Figure 8.9 compares the change of laser output power with the pump power under the single-wavelength pumping and the dual-wavelength pumping configurations. The results indicate that at a specific length of fibre (left: 50 m; right: 78 m), the threshold of dual-wavelength pumping was higher than that of the single-wavelength pumping, primarily due to the lower absorption at the second pump wavelength of 1120 nm. Interestingly, a saturated output power was reached in the case of single-wavelength pumping, whereas it was not observed in the dual-pumping cavity. This can be explained by the lower effective UL in the cavity, which allowed a larger proportion of Bi active ions to be involved in the lasing process and fewer ions to contribute to undesired processes in the fibre, such as upconversion. Consequently, a higher number of ions were excited to the laser's upper energy level, resulting in an output power increase from 6 to 17 mW (left) and from 4 to 11 mW (right) while maintaining the same fibre length and output coupling ratio. This improvement confirms the significant impact of UL in the fibre on the laser performance and emphasises the need to develop BASFs with low UL values.

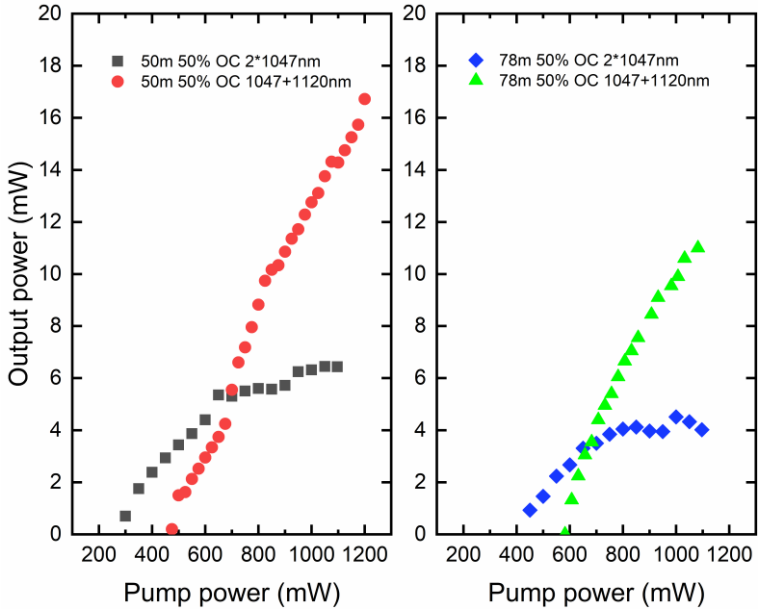

Figure 8.9 Comparison of the laser output under two configurations (black/blue: single-wavelength pumping at 1047 nm; red/green: dual-wavelength pumping at 1047 and 1120 nm)

Moreover, the high UL caused another effect in the cavity, where the BASF behaved as a saturable absorber. The behaviour of the fibre is similar to the mechanism of typical saturable absorbers where the transmission loss for signal reduces at high intensities. Based on this phenomenon in BPSFs, our group has previously demonstrated a self-mode locked pulsed laser using a 100 m fibre with a UL of ~17% [3]. In the case of the BASF with a UL of 60%, pulsing was also observed with fibre lengths of 53 m and 78 m. Without any polarisation controller (PC) inside the cavity, each pulse appeared randomly, propagating at its own speed and intensity. Figure 8.10 presents the laser output monitored by an oscilloscope (Tektronix DPO 7254) with a 2.5 GHz bandwidth. The top three waveforms were individually captured within a 10 ns time scale, while the bottom waveform was recorded within a 100 ns period. Duration of each pulse was measured to be in the range of 0.5~0.6 ns.

The self-generation of random pulses in the BASF may lead to laser instability and reduced the laser efficiency. It was hypothesised that a further reduction of the fibre length could potentially exacerbate the situation. Nevertheless, it is important to note that the self-pulsing behaviour of the BASF remains an area of interest for future research. This will be discussed in the future scope section (Section 9.2).

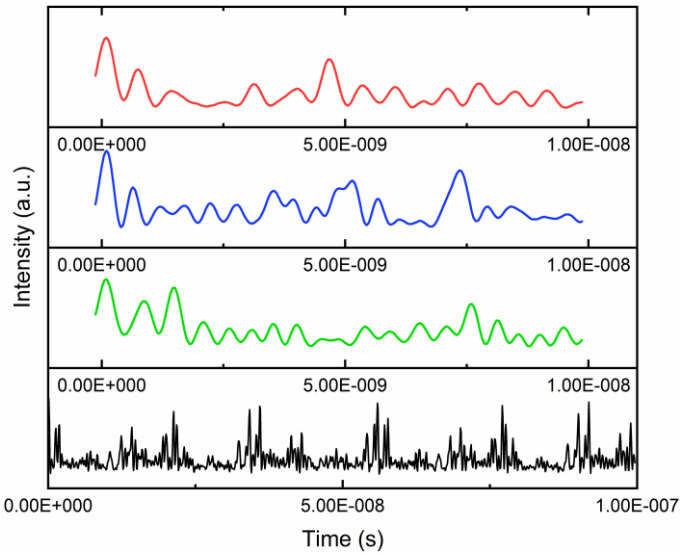

Figure 8.10 Random pulsing in the laser cavity, measured by an oscilloscope with a bandwidth of 2.5 GHz.

8.4 Conclusion and future work

This chapter presents a preliminary investigation of the performance of BASF lasers, operating in a linear cavity configuration. Two pumps with the same wavelength of 1047 nm were initially employed in a bi-directional manner, and the fibre length was reduced to 50 m. However, the laser exhibited poor performance, with a maximum power of 8 mW and a slope efficiency of 2.3% at 1180 nm. Additionally, the saturation was observed with an increase in the pump power, which can be attributed to the high UL at the pump wavelength in the BASF, resulting a significant impact on the laser performance.

Subsequently, a dual-wavelength pumping configuration was studied to reduce the effective UL in the cavity, with a second pump operating at 1120nm. This configuration successfully mitigated the laser's tendency to reach a saturation state with the available pump power, confirming that the previous saturation was indeed due to the significant proportion of UL and related detrimental processes such as upconversion. Consequently, the output power was increased to 17 mW. However, the UL remained relatively high of 60% and 40% at 1047 and 1120nm respectively, causing the self-generation of random pulses in the cavity.

It is essential to note that, while various pump configurations can mitigate the UL's impact, the fundamental solution to enhance the laser performance is through BASF fabrication. To develop efficient BASFs capable of delivering high power in lasers and substantial gain in amplifiers at 1.1 μm, there exists a significant demand for advancing BASF fabrication techniques. Efficient BPSF has been successfully delivered in our study and it is anticipated that BASFs could facilitate applications in a diverse wavelength band, thereby promoting the utilisation of related devices.

8.5 Reference

[1] S. Wang, Y. Wang, N. K. Thipparapu, M. Ibsen, D. J. Richardson, and J. K. Sahu, “Tunable CW Bi-doped fiber laser system from 1320 to 1370 nm using a fiber Bragg grating,” *IEEE Photonics Technology Letters*, 32(22), 1443-1446 (2020).

[2] M. P. Kalita, S. Yoo, and J. K. Sahu, “Bismuth doped fiber laser and study of unsaturable loss and pump induced absorption in laser performance,” Optics Express 16, 21032-21038 (2008)

[3] N. K. Thipparapu, C. Guo, A. A. Umnikov, P. Barua, A. Taranta, and J. K. Sahu, "Bismuth-doped all-fiber mode-locked laser operating at 1340 nm," Opt. Lett. 42, 5102-5105 (2017)

Chapter 9 Conclusion

9.1 Contributions to knowledge

This chapter provides a concise summary of the key findings presented in this thesis, which focuses on the development of Bi-doped fibres in phosphosilicate and aluminosilicate hosts (BPSF and BASF, respectively). The primary objectives of this work were to enhance the performance of the fibres from a material standpoint, to examine their spectroscopic characteristics, and to demonstrate and optimise related optical fibre devices. This thesis reports the development of lasers based on BPSF and BASF fibres operating at ~1.3 μm and ~1.1 μm, respectively. It is noteworthy that the fabrication of the BPSFs and BASFs presented in this thesis was performed by the author. The characterisation of the BPSFs was conducted in parallel by the author and Dr Yu Wang, while work related to BPSF lasers, and the entire study of BASF was carried out solely by the author.

In the case of BPSF, the author established a reproducible fabrication process using the MCVD-solution doping technique. Subsequently, a series of characterisations of the resulting fibres were performed, including glass composition analysis using SIM and EPMA techniques, and absorption and unsaturable loss measurements (Chapter 4). Afterward, a laser in a ring cavity configuration was established to further assess the performance of BPSFs. The performance of the laser was optimised by carefully selecting the fibre length and the cavity output coupling ratio (Chapter 5). A CW Bi-doped fibre laser (BDFL) at 1340 nm was demonstrated with a maximum power over 170 mW with about 700 mW of pump power at 1270 nm. The laser also had a slope efficiency of 38%, which, to the best of our knowledge, was the highest reported value of BDFLs at 1.3μm under a low pump power. At a subsequent time, two tuning elements, an optical filter and a mechanical-tuned FBG, were separately used to investigate the tuning capability of the BPSF. With the help of the optical filter, the laser was continuously tuned from 1305 nm to 1375 nm, achieving a 150 mW maximum power at the central wavelength of 1340 nm and a 60 nm tuning bandwidth with a 3 dB drop according to the maximum power. On the other hand, a home-made tunable FBG based on mechanical compression resulted in a similar performance of the tunable laser, with a maximum power 165 mW and maintained over 100 mW in the range of 1320-1370 nm.

Similarly, the author investigated BASFs through the fabrication for a collection of fibres (Chapter 6) and the study of the laser performance (Chapter 8). A detailed spectroscopic study was conducted, including the measurements of fluorescence spectrum and lifetime, calculation of absorption and emission cross-sections, and analysis of a unique visible anti-stoke emission in the fibre (Chapter 7). Fibre fabrication conditions were found to have a significant impact on BASFs. It was observed that the Bi concentration in the final resulting BASFs increases when helium gas (He) was utilised with a higher ratio compared to oxygen (O_2) during the collapsing stages of the preform. Additionally, an increased fibre drawing speed led to a reduction of the fibres' absorption and the UL in the near-infrared (NIR) spectra region. However, the outcomes were not consistently uniform across all cases. The spectroscopic parameters of the BASFs are reported, which are believed to be useful for understanding and modelling the laser and amplifier performance. The main challenge faced by the author is the high UL in the fibres, which resulted in a poor laser efficiency at the current stage. The preliminary study of the laser indicated the importance of further improvement of the fabrication process.

9.2 Future work

9.2.1 Development of the fabrication of BASFs

In this thesis, the development of the fabrication of BASFs has been discussed, but there is still significant room for improvement. Firstly, more samples need to be fabricated to optimise the fibre drawing conditions, and to draw a more convincing conclusion regarding its impact on the fibre characteristics. Previous reports have shown that for Bi-doped germanosilicate fibres and BPSFs, the unsaturable loss decreases as the fibre drawing speed increase [1,2]. However, our BASF did not consistently demonstrate a decreasing trend across all the examined cases; in contrast, a reverse trend was observed in our BPSFs [3], indicating an urgent need for a deeper understanding of the mechanism behind it. Secondly, the fabrication needs to be further optimised to decrease the UL in the fibre, by balancing the solution concentration, the gas atmosphere, and the temperature in the MCVD process. The effect of aluminium concentration has not been studied yet and requires further investigation.

9.2.2 Detailed spectroscopic study of BASFs including upconversion process

In addition to the aforementioned improvements to the fibre fabrication process, it is also important to conduct further spectroscopic analysis to understand the energy levels and energy transfer processes that exist within the BASFs. For instance, a possible immediate study is to measure the anti-stoke luminescence in BDFs with different concentrations of Bi and Al, or BASFs with different UL values, using pumps operating at different wavelengths such as 980, 1047 and 1120 nm. By comparing the performance of different fibres, the results of this study can provide valuable feedback for the improvement of fibre fabrication.

Furthermore, according to [4], the upconversion emission and the strength of this process exhibit pump power dependence when it sits at low or high levels. Therefore, a more detailed investigation can be conducted by monitoring this process under low (<0 dBm) and high (>20 dBm) pump powers. Additionally, the temperature dependence of the upconversion process has not been revealed in our study. Although this investigation is limited by time and equipment, such research in the future would benefit not only the fibre manufacturing process and device experiments but also to help understanding the spectral characteristics of Bi ions and different BACs in silica optical fibres.

9.2.3 Development of lasers and amplifiers at 1.1μm based on BASFs

- **Development of the Bi-doped fibre amplifiers at 1.1 μm**

Bi-doped fibre amplifiers (BDFA) have been demonstrated with great success at various wavelengths, providing a wide bandwidth and gain exceeding 20 dB [5-7]. This technology holds tremendous potential for expanding the telecom bandwidth and increasing the capacity of signal transmission. In a preliminary study conducted in the past, we demonstrated signal amplification at 1180 nm, achieving a gain of 11.5 dB for an input signal power of -4 dBm, using a BASF with a length of 140 m [8]. This outcome confirms the viability of developing a BDFA at 1.1 μm and underscores the need to investigate the gain at other bandwidths as well. A tunable laser source operating in the range of 1.1-1.2 μm is required for such studies.

- **Study the Bi-doped pulse lasers based on BASFs**

As presented in Chapter 8 of this thesis, a significant challenge associated with the use of BASFs in laser cavities is the occurrence of random pulsing due to the high UL of the fibre. This issue leads to instability of the cavity and a reduction in laser efficiency. However, the pulsing behaviour deserves further investigation, with the aim of either preventing its generation or leveraging it to our advantage. It is noteworthy that previous studies have demonstrated self-pulsing at 1340 nm using BPSFs as a saturable absorber [9], but there is currently no report of such pulsed behaviour in BDFL utilising BASFs itself at 1180 nm, without help of any other saturable absorbers.

- **Study the cladding pumping of BDFs for power scaling**

Power scaling through cladding pumping has been a well-established technique in fibres doped with REs, such as ytterbium (Yb) and thulium (Tm). Recently, a similar configuration has been demonstrated preliminary in BDFLs, with an output power of 300 mW and 150 mW at 1360 nm and 1460 nm, respectively [10]. This highlights the feasibility of employing cladding pumping in BDFs and emphasises the need to develop such fibre with a double-cladding design. Considering the core and cladding ratio and the corresponding absorption ratio, a pump wavelength with higher absorption is preferred to increase the laser efficiency, particularly, within the 700-800 nm range. The characterisation at such wavelengths of interest, including the absorption and UL, is also crucial to be studied.

9.2.4 Extending the gain bandwidth by using Bi fibre doped with multi-dopants

This thesis presents the development of BDFs with co-dopants of P and Al, separately, which exhibit luminescence at the wavelengths around 1.3 μm and 1.1 μm, respectively. As the performance of BDFs is known to be highly influenced by the surrounding environment of Bi ions, it is imperative to investigate the potential benefits of incorporating both co-dopants simultaneously into BDFs. Such an approach may yield superior performance compared to the individual co-dopants and provide valuable insights into the fundamental mechanisms governing the luminescence properties of BDFs.

9.3 Reference

[1] A. Khegai, F. Afanasiev, Y. Ososkov, K. Riumkin, V. Khopin, A. Lobanov, M. Yashkov, E. Firstova, A. Abramov, M. Melkumov, and A. Guryanov. “The influence of the MCVD process

parameters on the optical properties of bismuth-doped phosphosilicate fibers". *Journal of Lightwave Technology*, **38**(21), 6114-6120 (2020)

[1] S. Firstov, A. Levchenko, A. Kharakhordin, A. Khegai, S. Alyshev, M. Melkumov, V. Khopin, A. Lobanov, and A. Guryanov, "Effect of Drawing Conditions on Optical Properties of Bismuth-Doped High-GeO_2–SiO_2 Fibers." *IEEE Photonics Technology Letters*, **32**(15), 913-916 (2020).

[3] Y. Wang, "The study of bismuth doped fibres and the development of broadband bismuth doped fibre amplifiers", PhD thesis, 2023, University of Southampton, UK

[4] S.V. Firstov, K.E.E. Riumkin, V.F. Khopin, S.V. Alyshev, E.G. Firstova, M.A. Mel'kumov, A.N. Gur'yanov, and E.M. Dianov, "Anti-Stokes luminescence in bismuth-doped alumino- and phosphosilicate fibres under two-step IR excitation". *Quantum Electronics*, **46**(7), 612 (2016).

[5] N. K. Thipparapu, Y. Wang, A. A. Umnikov, P. Barua, D. J. Richardson, and J. K. Sahu, "40 dB gain all fiber bismuth-doped amplifier operating in the Oband," *Optics Letters*, **44**(9), 2248-2251 (2019).

[6] Y. Ososkov, A. Khegai, S. Firstov, K. Riumkin, S. Alyshev, A. Kharakhordin, A. Lobanov, A. Guryanov, and M. Melkumov, "Pump-efficient flattop O+E-bands bismuth-doped fiber amplifier with 116 nm 3 dB gain bandwidth," *Optics Express*, **29**(26), 44138-44145, 2021.

[7] A. Donodin, V. Dvoyrin, E. Manuylovich, L. Krzczanowicz, W. Forysiak, M. Melkumov, V. Mashinsky, and S. Turitsyn, "Bismuth doped fibre amplifier operating in E- and S-optical bands," *Optical Materials Express*, **11**(1), 127-135 (2021).

[8] N. K. Thipparapu, S. Jain, A. A. Umnikov, P. Barua, and J. K. Sahu, "1120 nm diode-pumped Bi-doped fiber amplifier," *Optics Letters*, **40**, 2441-2444 (2015)

[9] N. K. Thipparapu, C. Guo, A. Umnikov, P. Barua, A. Taranta, and J. Sahu, "Bismuth-doped all-fiber mode-locked laser operating at 1340 nm," *Optics Letters*, **42**(24), 5102-5105, (2017).

[10] A. Vakhrushev, Y. Ososkov, S. Alyshev, A. Khegai, A. Umnikov, F. Afanasiev, K. Riumkin, E. Firstova, A. Guryanov, M. Melkumov, and S. Firstov, "Output power saturation effect in

cladding-pumped bismuth-doped fiber lasers". *Journal of Lightwave Technology*, **41**(2), 709-715 (2022).

Appendix A List of publications

[1] S. Wang, Y. Wang, N. K. Thipparapu, M. Ibsen, D. J. Richardson and J. K. Sahu, "Tunable CW Bi-Doped Fiber Laser System from 1320 to 1370 nm Using a Fiber Bragg Grating," *IEEE Photonics Technology Letters*, **32**(22), 1443-1446(2020)

[2] S. Wang, N. K. Thipparapu, Y. Wang, M. Ibsen, D.J. Richardson, and J. K. Sahu, "Widely-tunable Bismuth-doped fiber laser for the 1305-1375nm wavelength range," *OSA Advanced Photonic Congress, Specialty Optical Fibers*, 2020, paper SoM4H.6.

[3] S. Wang, Y. Wang, N. K. Thipparapu, M. Ibsen, D.J. Richardson, and J. K. Sahu, "All-fiber wavelength-tunable Bi-doped laser employing a fiber Bragg grating operating in the 1300nm band," *Conference on Lasers and Electro-Optics Europe (CLEO), OSA Technical Digest (Optical Society of America, 2020)*, paper STh1P.7.

[4] Y. Wang, S. Wang, A. Halder, and J. Sahu, "Bi-doped optical fibers and fiber amplifiers". *Optical Materials: X*, **17**, 100219 (2023).

[5] N. K. Thipparapu, S. Wang, A. A. Umnikov, P. Barua, and J. K. Sahu, "All-fiber Bi-doped laser continuously tunable from 1317-1375nm." in *2019 CLEO/Europe-EQEC, paper cj_12_6.*

[6] N. K. Thipparapu, Y. Wang, S. Wang, A. A. Umnikov, P. Barua, and J. K. Sahu, "Bi-doped fiber amplifiers and lasers [Invited]." *Optical Materials Express*, **9**, 2446-2465, (2019).

[7] Y. Wang, N. K. Thipparapu, S. Wang, P. Barua, D. J. Richardson, and J. K. Sahu. "O-band bismuth-doped fiber amplifier and its temperature dependent performance." *In Sixth International Workshop on Specialty Optical Fibers and Their Applications (WSOF 2019)*, vol. 11206, paper 112061X-1.

[8] Y. Wang, N. K. Thipparapu, S. Wang, P. Barua, D. J. Richardson, and J. K. Sahu. "Study on the temperature dependent characteristics of O-band bismuth-doped fiber amplifier." *Optics letters* **44**, no. 23, 5650-5653, (2019).

[9] N. K. Thipparapu, Y. Wang, S. Wang, P. Barua, and J. K. Sahu, "Bi-doped silica-based fiber amplifier for O-band transmission," in *Asia Communications and Photonics Conference (ACPC) 2019, OSA Technical Digest (Optical Society of America, 2019)*, paper S3G.6.

[10] H. Ahmad, M. Z. Samion, A. A. Kamely, S. Wang, Y. Wang, and J. K. Sahu, "Multiwavelength Brillouin Generation in Bismuth-doped Fiber Laser with Single- and Double-Frequency Spacing", *Journal of Lightwave Technology*, **38**(24), 6886-6896 (2020).

[11] H. Ahmad, S.N. Aidit, M.Z. Samion, S. Wang, Y. Wang, and J.K. Sahu, "Tunable Dual-Wavelength Bismuth Fiber Laser With 37.8-GHz Frequency Spacing". *Journal of Lightwave Technology*, **39**(20), 6617-6623 (2021)

[12] H. Ahmad, N.H.A. Kahar, N. Yusoff, M.Z. Samion, S.A. Reduan, M.F. Ismail, L. Bayang, Y. Wang, S. Wang, and J.K. Sahu, "Passively Q-switched 1.3 μm bismuth doped-fiber laser based on transition metal dichalcogenides saturable absorbers", *Optical Fiber Technology*, **69**, 102851 (2022).

[13] K. Ji, D. Lin, I. A. Davidson, S. Wang, J. Carpenter, Y. Amma, Y. Jung, and D. J. Richardson. "Generation of High-power Picosecond Optical Vortex beams from a Yb-doped Multicore Fiber Amplifier." In *CLEO: Applications and Technology*, pp. ATh2C-1. Optica Publishing Group, 2022.

[14] K. Ji, D. Lin, I. Davidson, S. Wang, J. Carpenter, Y. Amma, Y. Jung, M. Guasoni, and D. J. Richardson, "Controlled generation of picosecond-pulsed higher-order Poincaré sphere beams from an ytterbium-doped multicore fiber amplifier" *Photonics Research*, **11**(2), 181-188